Department of Precision and Microsystems Engineering

Concatenation of a Frequency Doubling Mechanism to Achieve Higher Frequency Multiplication

Jos Tromp

Report no : 2023.099
Coach : Dr. ir. D. (Davood) Farhadi
Professor : Dr. ir. D. (Davood) Farhadi
Specialisation : Mechatronic System Design (MSD)
Type of report : Thesis report
Date : 30-11-2023

Preface

This project began with a literature review focused on portable energy sources for small-scale devices, with a particular emphasis on applications in microrobotics. The primary conclusion drawn from this review was the increasing relevance of elastic strain energy at smaller scales. This thesis is fundamentally built upon this insight, primarily addressing one of the core drawbacks of elastic strain energy – its limited range of motion.

Professor Davood Farhadi, the project supervisor, initially addressed this range of motion problem with the development of a compliant frequency doubling device. It takes a single-directional input motion and provides an output motion that moves back and forth. Luuk Samuels further developed this for his thesis by conducting a parametric study on this mechanism, providing valuable insights into the properties of the mechanism and setting the foundation for this work. This thesis addresses the concatenation of this mechanism to obtain higher number frequencies.

The structure of this thesis follows that of a scientific article, including sections for the abstract, introduction, method, results, and discussion. Detailed aspects of the methodology, supplementary results, and supplementary information are provided in the supplementary materials section to keep the main body of the report concise.

The literature review is provided at the end of this document in supplementary material S.9. Most of the files used for the project, including all codes related to the analysis (ANSYS; Matlab; etc.), MATLAB .fig files and vector files of all figures are provided on onedrive: https://1drv.ms/f/s!AuFKEiGsd8cUhWpIP4fVCiUKUj9B?e=1Po5dk.

Concatenation of a Frequency Doubling Mechanism to Achieve Higher Frequency Multiplication

Jos Tromp

5393078

A thesis to obtain the degree of Master of Science
To be defended publicly on November 30, 2023 at 15:00

Precision and Microsystems Engineering
Delft University of Technology

Abstract

The range of motion of elastic energy sources is limited by the size of its transmission system. To enhance this range of motion without compromising the size, previous research introduced a frequency doubling mechanism with the intention to concatenate these mechanisms. This study serves to achieve higher numbers of frequency multiplication by concatenating up to three frequency doubling mechanisms. A crucial challenge is to reduce the input force required to operate the compliant design, even in the absence of output load, to ensure the output moves twice the distance of the input. The optimization process involved simulations to achieve a near-perfect Geometrical Advantage (G.A.) of 2 while ensuring the highest possible load capacity to minimize force-induced geometrical variations. The optimized mechanism was then statically balanced with buckled beams to minimize the input force of each frequency doubling mechanism. The buckled beams introduced negative stiffness, adding potential energy to counteract forces, and ultimately reducing the input force to approximately 5.3% of the initial force. Three frequency doubling mechanisms were concatenated and experimentally validated, achieving a frequency multiplication of 8. The real prototype demonstrated successful results, although the input force was not entirely eliminated, the desired frequency multiplication was achieved. These results form the basis for a compliant frequency multiplication mechanism, enhancing the range of motion of elastic strain energy sources through the implementation of a compact transmission system.

1 Introduction

Small scale devices are increasingly being explored for various applications, such as microrobotics [1–3]. For powering devices at these reduced scales, the significance of elastic strain energy becomes more pronounced due to their high energy density and power density [4]. However, these applications face a significant challenge due to the limited range of motion resulting from limited material strain. Traditionally, transmission mechanisms such as gears have been used to enhance range of motion but they introduce friction, energy loss, wear, and maintenance issues [5]. Compliant mechanisms present an attractive alternative to increase the range of motion without the drawbacks associated with conventional transmission systems. Most known compliant amplification systems are some form of leverage systems [6], however these introduce large design spaces of at least the size of the range of motion itself. A different approach is to implement frequency multiplication to amplify range of motion. This enables back-and-forth motion of the output and therefore enables the range of motion to surpass the design space of the mechanism[1].

In the state of the art a compliant mechanism has been proposed that enables frequency multiplication of an input motion by utilization of a singularity point [7]. This mechanism was further developed by optimizing its dimensions and providing a deeper understanding of the mechanism [8]. These works combined resulted in a frequency multiplier optimized for a linear input motion of 2 mm and outputting a back-and-forth linear motion of 2 mm. A schematic of the mechanism is provided in Figure 1 where it can be seen that the input both moves to the left and right, whereas the output only moves up in both cases. This results in a sort of V-shape input-output profile providing a Geometrical Advantage (G.A.) of 2, since the output stage travels a total of 4 mm and the input stage a total of 2 mm. A G.A. of 2 in itself is not the main goal, the intention is to feed this output again into the input of another mechanism to double the frequency and the range of motion once again. This is called concatenation of the mechanism and it can provide any integer frequency multiplication up to 2^n concatenations.

However, due to the compliant nature of the frequency doubling mechanism an input force is required to elastically deform the flexural members and initiate motion (see Figure 1.D.). This is actually a limiting factor for concatenation because these forces accumulate with each successive concatenation, quickly surpassing the load-carrying capacity of the mechanism or altering the G.A. to the extent that frequency doubling does not occur. Recent developments in the field of compliant mechanisms have proposed to cancel the elastic deformation forces by introducing an extra source of potential energy into the system [9, 10], making it statically balanced.

It is the objective of this project to statically balance the frequency doubling mechanism to achieve a near-zero input force and successfully concatenate it. This will lay the groundwork for a compliant transmission system that extends the range of motion of elastic strain energy sources beyond the limitations of their design space. In the subsequent sections of this thesis, we will delve into the methodology, simulations, and results that have led us to our proposed solution.

2 Method

The methodology consists of three main parts, first we have optimized the dimensions of the frequency doubling mechanism for successful concatenation. Second, we have statically balanced this mechanism to relieve the input forces. The last phase involves actual concatenation of multiple mechanisms through simulations and a physical prototype.

2.1 Dimensional optimization

Figure 2 illustrates the mechanism, showcasing the relevant dimensions that define the kinematics of the mechanism. Tuning these parameters influence the kinematics and mechanics of the mechanism, such as the input-output profile and G.A., as well as strength, stiffness and other properties [8].

The design parameters are normalized based on the input displacement u_{in} which is consistently set to 1 mm throughout this project (1):

[1] The range of motion throughout this thesis is defined as the total amount of traveled distance (back and forth).

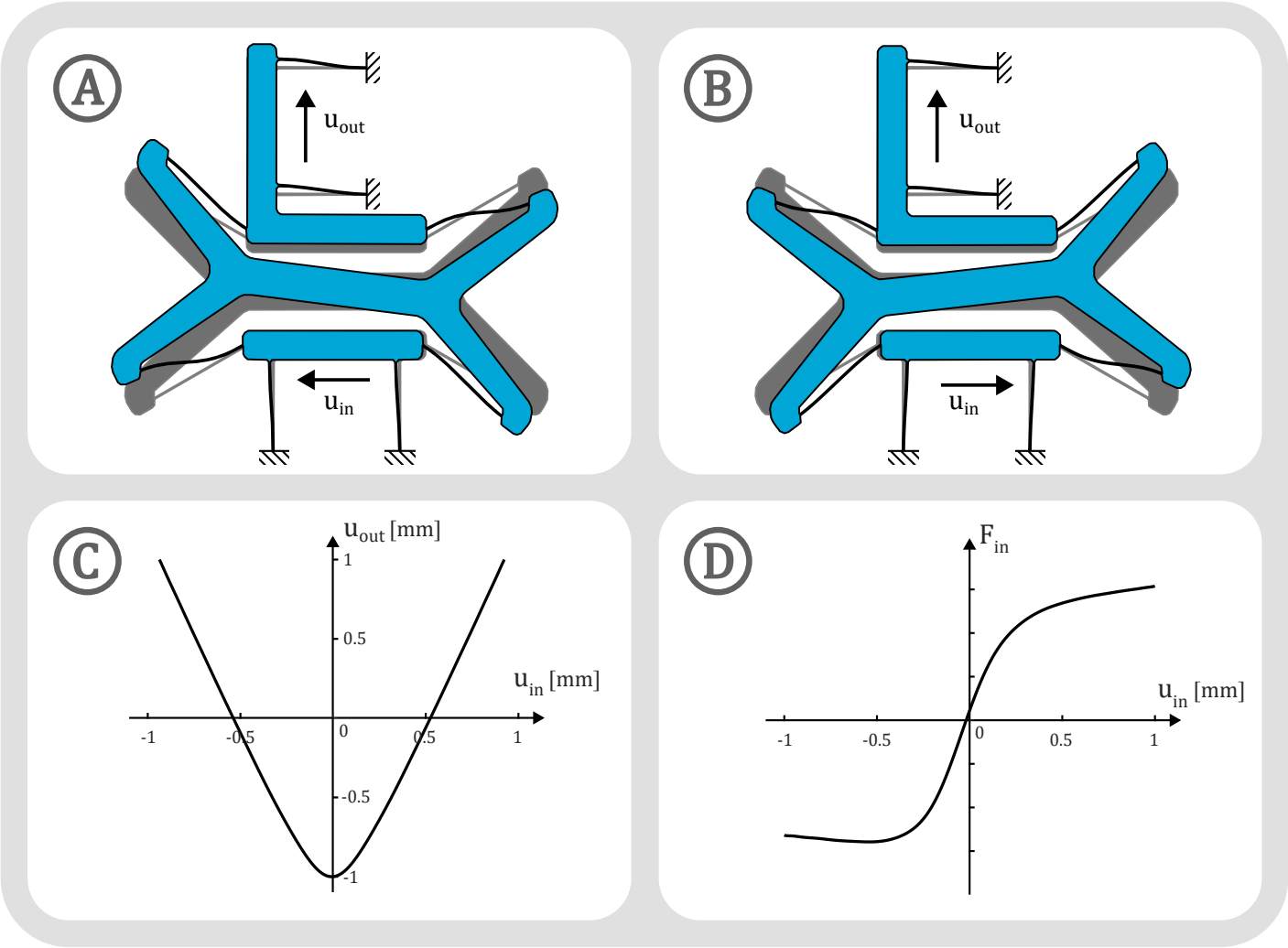

Figure 1: Working Principle of the Frequency Doubling Mechanism. Deformation of the mechanism with **(A)** negative input displacement and **(B)** positive input displacement. The black lines represent flexural beam elements. **(C)** A typical input-output displacement profile of the frequency doubling mechanism and **(D)** a typical input force for moving the mechanism with zero load at the output.

$$l = L/u_{in} \qquad l_1 = L_1/u_{in} \qquad l_2 = L_2/u_{in} \tag{1}$$

Criteria for effective concatenation

For successful concatenation, we identified a single main criterion: maintaining a G.A. of 2 in every case. Figure 12 from supplementary material S.1 clearly shows that a different G.A. than 2 will jeopardize the frequency doubling behavior when concatenating only a few mechanisms.

The G.A. is not only influenced by the design parameters, forces acting on the output of a mechanism also change the input-output profile and therefore the G.A. Since the we want to concatenate the frequency doubling mechanisms, the input force of each mechanism will act on the output of the mechanism before it and by doing so create an accumulation of force in the system. While attempts will be made to reduce the forces required to actuate the mechanism, we do not expect to bring the input force to exactly zero due to nonlinearities, simulation errors, fabrication errors, and more uncertainties. Also, we have explored the accumulation of (input) forces in concatenated systems and found that forces multiply by a factor of 2 to 4 per concatenation. This is due to the duplication of the range of motion and the nonlinearity of the input-output profile (refer to Figure 13 in supplementary material S.1). The maximum number of concatenations will thus depend on how well the G.A. will be held constant from any remaining forces. Thus, besides a correct parameter combination to create a G.A. of 2, a load capacity is defined to be an indicator for the amount of deflection from a force acting on the output of the mechanism. And it is normalized by the stiffness of the linear stages. The detailed equations are provided in supplementary material S.2.

The final criterion to be considered is the total size of the mechanism, which is also a function of the parameters. The load capacity is however more important, only if the size can be decreased without significant loss of the load capacity, a smaller design will be chosen. Other properties, such as the shape of the input-output profile, do not limit the number of frequency multiplication and are therefore not considered as criteria in this study. They are only checked to stay within reasonable boundaries, which was true for all examined designs.

Material

A flexure material has to be chosen early in the project, since the design selection will also depend on it. Two main flexure materials with their fabrication methods were

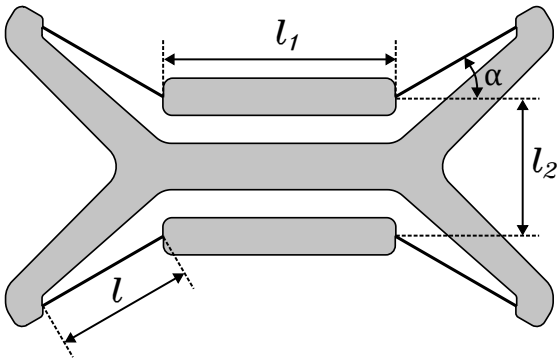

Figure 2: Relevant Parameters of the Mechanism. The design is point symmetric.

identified: flexures from 3D-printed PLA or other filament material, integrated with the entire design, or flexures cut from a type of spring steel and glued into a 3D-printed design. Both have their advantages and disadvantages, but the most important criterion here has to do with the prospect of statically balancing the mechanism in the second phase. To successfully statically balance a mechanism, the losses in the system need to be minimized as much as possible. Plastic is a viscoelastic material that dissipates energy upon deflection, limiting the amount of energy equalization for the statically balanced mechanism. Steel, however, displays a low mechanical loss upon deflection which is why we have selected steel with its corresponding fabrication method. Specifically, fully hardened AISI301 was chosen, a stainless spring steel with a high yield strength of 965 Mpa and Young's modulus of 190 Gpa. The stress for our design is limited to 500 MPa to achieve a safety factor of approximately 2. This leaves some room for uncertainties and the yet unknown forces from concatenation.

Simulations
Optimization of the dimensions is carried out through simulations to enhance the performance of the frequency doubling mechanism. The design space is defined as a three-dimensional space with predetermined boundaries, encompassing three of the four relevant parameters. Within the simulations, a significant aspect involves optimization of the G.A. of the mechanism. Initially, the mechanism comprises four parameters. However, one of these parameters is optimized to achieve a G.A. of 2, thereby reducing the design space to three parameters. This optimization of the G.A. is done in four steps:

- **Step 1:** An initial estimation for the optimized parameter is derived based on calculations and design considerations.
- **Step 2:** The simulation is performed using the estimated value of the optimized parameter, along with the other fixed parameters.
- **Step 3:** The simulation results are carefully analyzed, and a new, refined value for the parameter is selected, considering the desired G.A..
- **Step 4:** Steps 2 and 3 are repeated iteratively until the G.A. is within the specified range of 2±0.01.

This iterative approach allows for fine-tuning of the fourth parameter, ensuring that the desired G.A. is achieved. This approach effectively narrows down the design space to three parameters, streamlining the evaluation of parameter combinations for the optimal design.

The simulations for each design within the reduced three-dimensional parameter space provide valuable properties that aid in evaluating the mechanism's performance. More simulations were done to find these properties, primarily the input-output relation and the load capacity. The detailed simulation procedure is explained in supplementary material S.4.

Design selection
After evaluation of the results, a design was selected based on the design criteria provided above.

2.2 Static balancing

The input-output relationship of the frequency doubling mechanism is affected by the forces from strain energy in the compliant segments. As already indicated, this is unwanted since the forces change the G.A. of the mechanism. Any alteration from a G.A. of 2, as well as any input force will be magnified by every extra concatenation. Considering that the forces required to elastically deform the compliant beams are mostly conservative, in theory, they can be canceled out if an appropriate mechanism is found. The criteria for a statically balanced mechanism is that it has constant potential energy over its range of motion, creating a mechanism that is neutrally stable and in continuous equilibrium [9, 10].

Force profile
Achieving constant potential energy over the range of motion can be done in two main ways: lowering the peaks of the potential energy, filling up the valleys, or some combination of the two. Since lowering the potential energy curve requires design modifications, it is opted to first investigate the possibility of adding potential energy to the system and thereby statically balancing it. This practically means that the input force of the mechanism must be cancelled out by some other source of energy acting on any part of the mechanism. The placement of this energy source on the mechanism will determine how its force profile should look like to cancel out the input force. We can obtain the force profiles on multiple locations of the mechanism by actuating the mechanism from that location and observing the force required to do that. This was done at the input and output stage of the selected design, and it turns out that the input force is nonlinear of shape, with high stiffness and a softening effect towards the end of its motion, the output force however is highly linear of shape, it starts off with a constant force and continues then with low stiffness. This result was taken as a starting point for investigating a static balancing method.

Besides actuation at the input and output stages, the mechanism could, in theory, be actuated from various positions and under different angles. These have eventually not been explored since a feasible and practical solution was found.

Static balancing methods
Two primary methods from existing literature were ex-

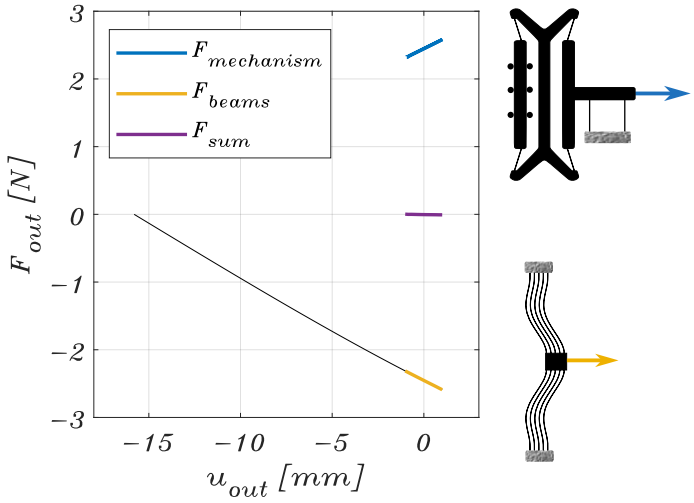

Figure 3: Static balancing method. $F_{mechanism}$ is the force to actuate the mechanism at the output stage, starting at $u_{out} = -1$ from the undeformed configuration. F_{beams} is the force from the buckled beams. F_{sum} represents the output force when combining the butterfly mechanism with the buckled beams.

plored: Opposing constant force cancellation, which requires 'constant force mechanisms', and the more common method with opposing force profiles, often requiring negative stiffness devices [11]. Given our mechanism's positive stiffness behavior, we opted for the application of negative stiffness. (The constant force method could have been chosen due to the near-constant force profile at the output stage. However, this requires an extra frequency doubling mechanism to be connected to the output stage of the main one that cannot be used as functional mechanism resulting in a more complex solution. Additionally, a significant force would remain due to the remaining stiffness.)

A few negative stiffness solutions were found in literature, including preloaded coil spring, (preloaded) buckled beams and repelling magnets [12, 13]. Buckled beams would be far superior in this case due to their compatibility with existing beam elements in the mechanism and their scalability. Standard straight buckled beams offer a linear negative stiffness. When we assess these options in conjunction with the recognized force profiles for input and output, the preferred choice is the use of buckled beams acting on the mechanism's output stage.

Figure 3 illustrates the method of force cancellation utilizing buckled beams. The buckled beams will be attached to the output side of the mechanism since that is where the force profile can be approximated by the buckled beams. The flexural beams will be pre-compressed to initiate the buckling behavior and create negative stiffness. Additionally, a horizontal displacement (in the direction of u_{out}) will be imposed on the beams to provide for the constant force component in the mechanism. This will result in a sum of forces equal to a fraction of the original force, depending on the type and amount of nonlinearity apparent in $F_{mechanism}$ and F_{beams}.

Buckled beam(s) calculations

From the parametric optimization phase a design has been selected, which provides the starting point for the dimensioning of the negative stiffness device. The frequency doubling mechanism comes with a known actuating force on the output stage that needs to be opposed by the buckled beams. The force required to move the mechanism at the output is approximated by the linear function:

$$F_{output} = kx + F_0 \tag{2}$$

with:

$$\begin{aligned} k &= 133.97 \text{ N/m} \\ F_0 &= 2.314 \text{ N} \end{aligned} \tag{3}$$

The buckled beams need to provide exactly the opposite force to equation (2). Dimensioning of the beams start with the selection of a certain length and thickness as a function of the required pre-displacement and maximum allowable stress. The required pre-displacement is equal to:

$$x_0 = \frac{F_0}{-k} = -17.27 \text{ mm} \tag{4}$$

A certain length is required to keep the stress low, and a certain compression (d_0) is required to buckle the beams but not less important to enable the required range of motion, defined by x_{tot}. To calculate the required compression for the required range of motion, equation (5) was used from literature [14].

$$d_0 = \frac{3}{L}\left(\frac{x_{tot}}{2\gamma}\right)^2 \tag{5}$$

With γ as a factor that goes from 0 to 1 indicating the amount of range there is left in the negative stiffness. At $\gamma = 1$, the endpoint of the negative stiffness is reached, which means that further movement will give positive stiffness. A lower value of γ is preferable because the behavior is more linear at zero displacement.

By using equation (5) an iterative process was done by selecting a set of values for L and d_0 and simulating the stress and force-displacement curve in ANSYS. With a stress limitation of 500 Mpa and a visually linear behaviour of the force-deflection curve, the following set of dimensions were obtained:

$$\begin{aligned} L &= 70 \text{ mm} \\ d_0 &= 6.2 \text{ mm} \\ \gamma &= 0.80 \end{aligned} \tag{6}$$

This gives a stress of 498 Mpa with a near-linear force-deflection and a stiffness of -13.9 N/m per beam. Thus, for a total stiffness of -134 N/m the number of required beams is 9.6 which rounds up to 10. This makes the stiffness too low (too negative), to reduce the stiffness the length of the beams was increased. Which releases a little bit of stress too, so the amount of compression (d_0) was also increased to get a more linear force-deflection. However, since the force-deflection is not perfectly linear, the constant force was not satisfied. This required an iterative process by changing the pre-displacement x_0, the beam length L, and the pre-compression d_0 for a solution where the stiffness was close to -134 N/m (within 1%), the force F_0 was within 1% of 2.314 N and the stress was close to the maximum for the most

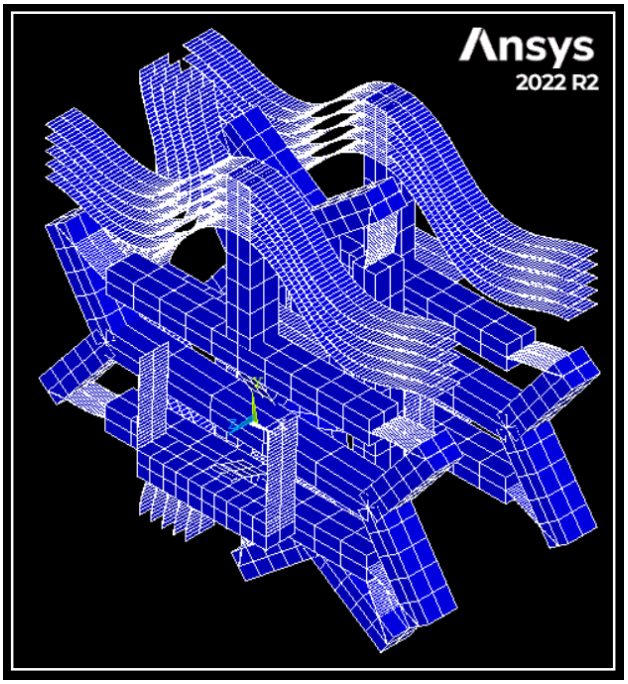

Figure 4: 3D-Screenshot of ANSYS simulation. This is the simulation of 3 concatenated statically balanced mechanisms. The leftmost linear stage is the input, the output stage is on the backside hidden by the mechanism.

amount of linearity, leading to the dimensions and properties provided in equation (7):

$$\begin{aligned} L &= 75 \text{ mm} \\ d_0 &= 7.585 \text{ mm} \\ x_0 &= 14.8 \text{ mm} \\ n &= 10 \\ k_{beams} &= -137 \text{ N/m} \\ F_{0,beams} &= 2.316 \text{ N} \\ \sigma_{beam} &= 499 \text{ Mpa} \\ \gamma &= 0.70 \end{aligned} \tag{7}$$

This results in a negative stiffness device with 10 beams and properties within 1% of the required force profile.

2.3 Final design and concatenation

The last phase involves concatenation, where we link multiple frequency doubling mechanisms to enhance their combined effect. Achieving this required us to displace each successive mechanism's input by 1 mm ($= u_{in}$), ensuring that they align with their singular positions. The output of each mechanism functions as the input of the next mechanism, except for the first mechanism where an extra input stage is added to function as its linear guide. This implies that, for a perfectly statically balanced mechanism, the stiffness of the first linear stage would still be visible. In theory, this could be canceled out with a different set of buckled beams attached to the input stage. For this project the input stage forces have been neglected since the objective is to concatenate as many devices as possible, which is not effected by the actuating force of the first input stage.

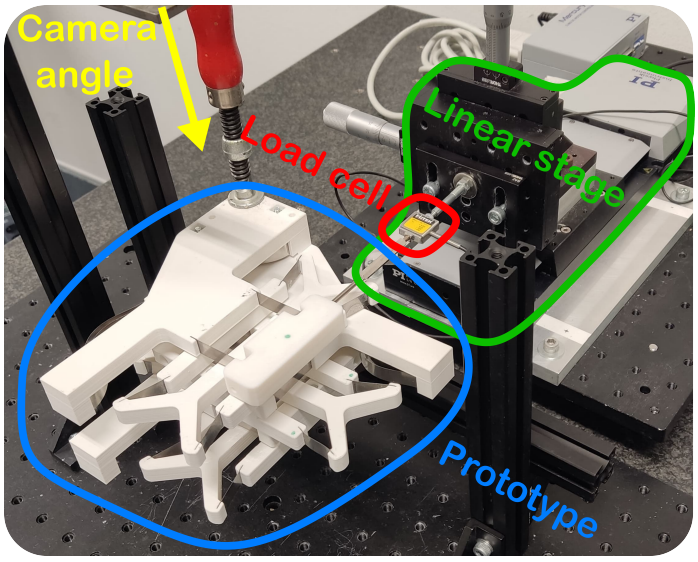

Figure 5: Experimental setup. For force measuring and video tracking of the prototype.

The simulations of the final mechanism and the concatenated model are again performed in ANSYS APDL. The simulation method with keypoints and code are provided in the supplementary materials S.5. Furthermore, Figure 4 presents a screenshot of the simulation of 3 concatenated mechanisms. Animations of the 1, 2 and 3 concatenated mechanism simulations are added in videos A5, A6 and A7 respectively in supplementary material S.6.

Prototype

A physical prototype was developed as a crucial step in validating the results of the simulations. The prototype was designed in SolidWorks, and it was designed such that every butterfly mechanism is the same no matter the concatenation step. Two separate linear stages were designed, which would alternate. Every butterfly mechanism would rotate 90 degrees for every concatenation. An important feature designed into the prototype is the ability to tune parts of the mechanism, namely the amount of predisplacement of each stage, the amount of precompression of the buckled beams and their lengths. This way any fabrication errors or failures can maybe be tuned out. Even though this makes the comparison between simulation- and experimental results harder, it is considered that a functioning device is superior to a correct comparison as a demonstration of the concept.

Due to the finite compliance of the 'rigid' beams in the prototype, the simulations would, by definition, yield different results. The simulations were, therefore, performed with flexible beam elements to more closely approximate the prototype. Rigid beams were used too, giving similar results but for comparison purposes the flexible simulations are presented later in this report.

The rigid parts of the prototype were 3D-printed from PLA material and the flexures are cut from a strip of ordered spring steel (AISI301). Slots were printed in the printed parts to create a bonding surface for gluing in the flexures with superglue. A more detailed explanation of the prototype fabrication is added to the supplementary material S.7 together with the resulting pictures of the assembled mechanism.

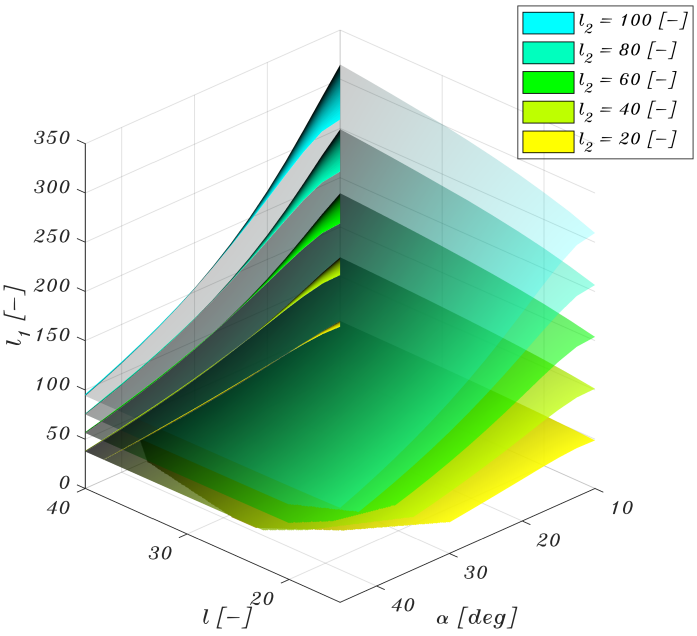

Figure 6: Parameter combinations for a G.A. of 2. These are the results from simulation #1, the data points are meshed on surfaces with constant length l_2. Results for $l_2 = 30, 50, 70$ and 90 are hidden for visibility. The darker the color, the larger the length of the flexure (l).

The experimental data was gathered by a combination of video tracking and force measurements performed on the prototype. A picture of the experimental setup is provided in Figure 5. It uses a linear stage from Physik Instrumente (M-505 translation stage), with a force sensor from FUTEK (type LSB200 FSH03875) capable of measuring up to 45 N with ±0.25% accuracy. The video was taken on a phone camera recording in 4K at a rate of 30 FPS, green dots on the prototype were later tracked with tracking code in Matlab.

3 Results

This section presents the results of dimensional optimization, the statically balanced mechanism, and the concatenated design as outlined in the methods section. For all results an input of $u_{in} = 1$ mm is used.

3.1 Dimensional optimization

The parametric study yielded two main results, (1) the parameter combination for a G.A. of 2 and (2) the load capacity as a function of the parameters. The results from the first part (simulation 1) are provided in Figure 6, with the fourth parameter l_1 as a function of the other three parameters l, l_2 and α. Surfaces are meshed to connect the data points and provide this visual representation of the data. Only half of the results are shown here for visibility, the additional results are provided in supplementary material S.6, Figure 21 and 22.

The results for the load capacity are presented in Figure 7. The highest scoring designs from the three-dimensional data are mapped on the two planes (l, α) and (l_2, α) allowing us to observe the optima for the individual parameters. It is observed from the l-α-plane that a lower flexure length l results in a higher load capacity and for α the optimum lies in the range of 17.5°. From the l_2-α-plane it is observed that higher load capacity designs are more concentrated towards higher values of l_2, but the dependence is less pronounced and from $l_2 > 60$ the load capacity remains relatively constant.

An extra illustration (Figure 25) in supplementary material S.6 provides the input-output profiles and the force profiles. It can be seen that the diversity of input-output profiles is not that much, thus it will not be taken into consideration during the design selection. It also shows that the output forces for all results have the same linear type of behavior meaning that all designs can be statically balanced with the same method.

Design selection

The highest load capacity solutions are concentrated in the region around $l = 20$ and $\alpha = 17.5°$, with a slight dependency on l_2. The highest load capacity solutions occur at high values for l_2, but the size can significantly be reduced with less than 10% of a reduction of the maximum load capacity. The chosen solution was therefore based on a reduced size with still a high load capacity resulting in the final parameters (8):

$$\begin{aligned} l &= 20 \\ l_1 &= 91.8 \\ l_2 &= 40 \\ \alpha &= 17.5\,\text{deg} \end{aligned} \tag{8}$$

The load capacity of this design is equal to 660, about 7.5% lower than the highest scoring design with a load capacity of 714. Moreover, the simulation results reveal a maximum stress of 490 MPa and a G.A. of 2.0023.

3.2 Static balancing

With the buckled beams the input force of the statically balanced device has been simulated and analyzed, presented in Figure 8. These are the results for the simulations with rigid body parts and a perfectly linear input stage since these were used to statically balance the mechanism. The highest input force for the statically balanced mechanism is 2.03 mN, which is a reduction of over 99% of the non-statically balanced mechanism.

3.3 Final design and concatenation

The results for the final design were acquired by both simulations and a physical prototype. Results for 2-fold, 4-fold, and 8-fold frequency multiplication were obtained by concatenating three mechanisms in total, covering all other integer frequency multiplications in between, by selecting a different starting or end point. Figure 9 shows the embodiment of the design with three concatenated mechanisms. The separate stages correspond to the displacements u_0, u_1, u_2 and u_3, from front to back.

Final results (simulation and prototype)

The final results of the concatenated mechanism includes the input-output relationships and the input forces obtained from both simulations and experiments. These results are provided in Figure 10. The left column shows the data from

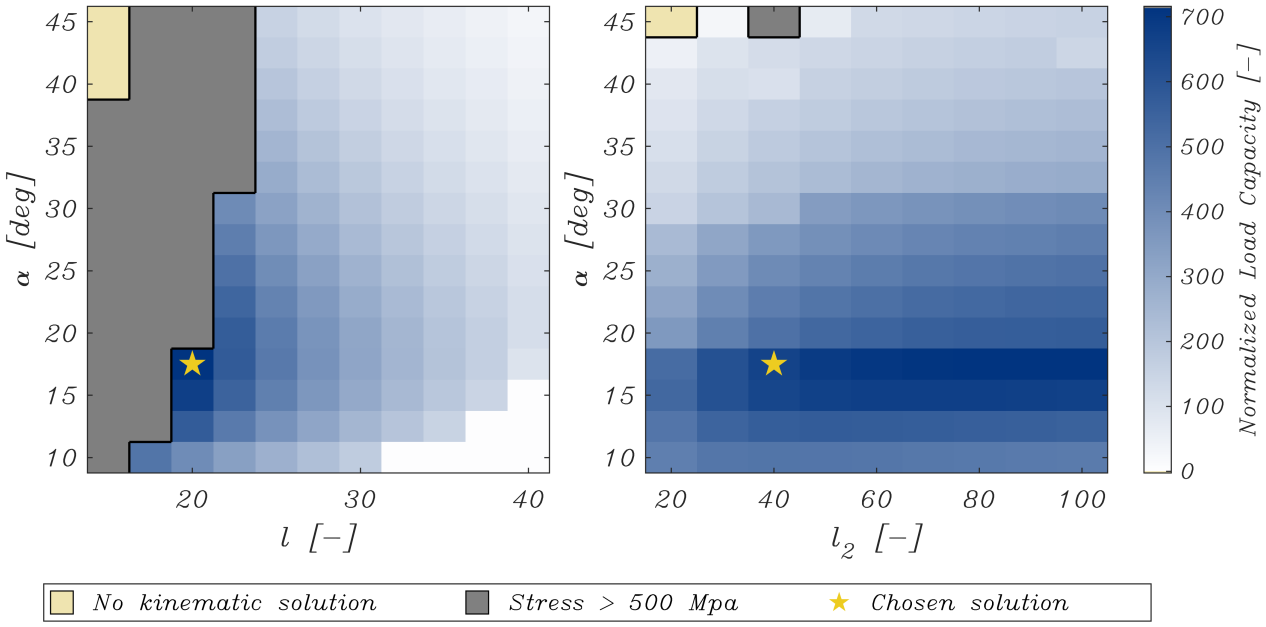

Figure 7: Normalized Load Capacity. Maximum normalized load capacity for all simulations projected on the l-α-plane and the l_2-α-plane. The areas with no kinematic solution correspond to parameter combinations where no G.A. of 2 was found.

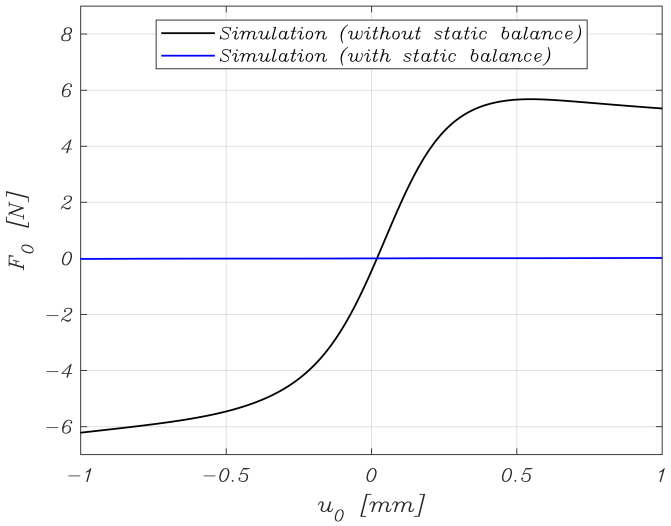

Figure 8: Input force before and after static balancing. This data represents the simulation results for a single mechanism with perfectly linear input stage.

the three concatenated mechanisms, the middle column from two and the right column from a single mechanism. The simulation results of the single and two concatenated mechanism(s) were performed with dimensions measured from the prototype for comparison purposes. The videos used for the experimental results are added to the supplementary materials S.6 numbered as video A1, A2 and A3. Video A4 provides a more detailed view of the three concatenated mechanisms. The vertical offset of the data is chosen such that it aligns with the concatenations. It is observed that the prototype does achieve the targeted 8-fold frequency multiplication, albeit with a reduced motion increase due to the output spanning ±0.5 mm instead of ±1 mm as in the simulations. The measured input forces for all three configurations seem to not align with their relative simulations, even though the profiles show somewhat the same number of peaks and valleys. For the single and double mechanism, a shift of the force is observed to the negative side, meaning the mechanism has a preference to move to one side than to the other. This is not observed in the simulations, which shows a more symmetric force profile. The maximum absolute force of the single mechanism is 0.33 N, for the double mechanism 0.86 N and for the triple 2.11 N. For the single mechanism this is a reduction of 94.7% (from 6.21 N). Regarding the force data, the efficiency has been calculated based on the total amount of work done and the work lost by hysteresis (area between the forward and backward cycle), see equation (9). The total work was calculated as the average of the forward and backward cycle with n as the number of steps of the simulation.

$$\begin{aligned} \eta &= \frac{W_{\text{tot}} - W_{\text{loss}}}{W_{\text{tot}}} \\ W_{\text{tot}} &= \frac{\text{2e-3}}{2n} \sum_{i=1}^{n} \left(F_{0,\text{forw}}(n) + F_{0,\text{rev}}(n)\right) \\ W_{\text{loss}} &= \frac{\text{2e-3}}{n} \sum_{i=1}^{n} \left(F_{0,\text{forw}}(n) - F_{0,\text{rev}}(n)\right) \end{aligned} \tag{9}$$

This results in an efficiency of 60% for the three concatenated mechanisms, 87% for two and 75% for the single mechanism. Obviously, none of the input forces are transferred to actual work so the real efficiency would be 0%, but it gives an impression of the losses in the system.

4 Discussion & Conclusion

4.1 Interpretation of results

Analyzing the parameter combination leading to a G.A. of 2, we observe that the flexure length l does not have a lot of impact on the G.A. which is probably caused by the virtual

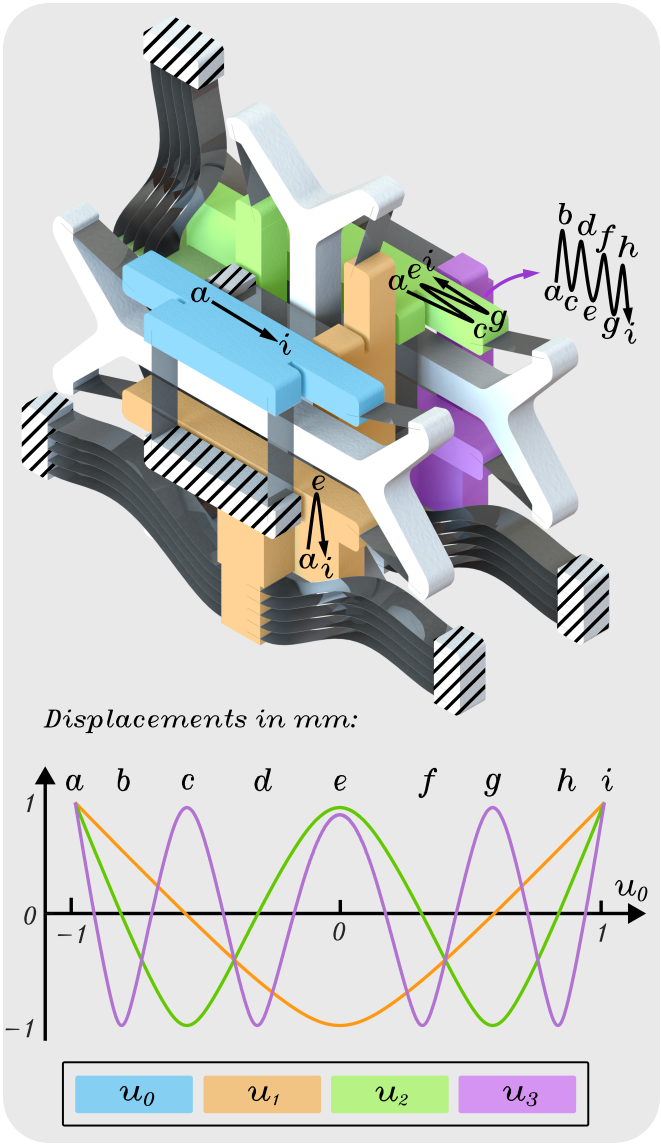

Figure 9: Design embodiment frequency multiplier. The 3D view is simplified for visibility with the fixed world shown as diagonal lines. In the prototype all ground objects are connected by a frame. The blue color represents the input linear stage with its corresponding displacement u_0. The displacement u_0 goes from -1 to +1 with its neutral position at $u_0 = 0$. Displacement u_1 corresponds to the orange color, u_2 to green, and u_3 to purple. The displacements are graphed at the bottom of the figure. Letters a till i are included as a guide to showcase every part of the movement. The graph illustrates the concatenated behavior of the single frequency doubler neglecting that the forces will change the shape of the input-output displacement.

rotation points that do not depend on the flexure length. The flexure length l only has some influence when α is low ($<20°$), which can be assigned to larger rotations of the butterfly when α is low leading to axial retraction. Besides this point, we observe that l_1 increases linearly with l_2 for a given α, l_1 is higher than l_2 up to $\alpha = 45°$. When α is 45° the key condition for a G.A. of 2 is the that the length l_1 is about equal to l_2 and for all other values of α there is a certain ratio l_1/l_2. Only for low flexure lengths l this ratio changes, which is probably caused by the axial contraction of the flexure when rotation by larger amounts.

The lengths of the mechanism become bigger when α is lower. The higher α, the smaller l_1. Designs with high values for α are not always found, especially not when l_2 is small. We recommend using this data not as precise answers, only an indication of what design parameters are possible and what the impact of one on the other is. For slight changes in the design (flexure thickness, flexure width, linear stage dimensions, etc.) the exact parameter values will change a bit. One parameter should be optimized for an exact G.A. of 2 for each new design with minor changes.

Load capacity results reveal a design preference for high output stiffness at low flexure lengths l (as long as the stress is below maximum) and a flexure angle α of 17.5°. The load capacity increases for shorter flexure lengths, which can be assigned to the increased stiffness in all of its directions. The optimum α value is not immediately apparent. Lower angles than 17.5° are less optimal due to reduced force alignment with the flexure, causing buckling under load. Higher α values result in larger butterfly rotations, increasing deformation of the flexures and reducing axial stiffness, particularly near the end of the range of motion. It is expected that this is the reason for the lower load capacity for higher values of α.

Upon analyzing the final simulation and experimental results of the mechanism, several unexpected occurrences became apparent. One notable discrepancy was a reduction in the input force of the single mechanism, which was not reflected in the simulations. Upon close inspection of the prototype with and without buckled beams, it appeared that the input linear stage was offset by about a millimeter. This is due to fabrication and assembly errors, and it is the main reason for this discrepancy of the data. In addition, different dimensions have been measured compared to the 3D-model (up to 2%) and the predisplacements of each mechanism have been tuned by hand. Even though this is thought to be the main source of error, other sources of error include:

- **Modeling errors (<10% error):** This includes simplifications of the simulated model (Especially the frame which is only modelled as beams without the many details.) and mathematical approximations of the simulation.
- **Material properties (<5% error):** The material properties may alter from the simulation, in particular the 3D-printed parts, which are modelled as isotropic materials which is a major simplification of the anisotropic structure of the printed material.
- **Testing inaccuracies (<2% error):** Testing setups and equipment have inevitably introduced non-ideal conditions that are not represented in the simulations. For example, the rigidity of the frame to which the prototype was clamped, the clamping force impacting the mechanism, etc. Even though all experimental conditions have been setup with utmost care, the experiments can never be perfect and could explain a minor part of the errors between the experimental and simulation results.

The primary goal is not perfection in simulation or prototype, but rather to maximize concatenation. However, since the simulations present results of much higher quality (primarily due to a consistent G.A.), the source of error needs

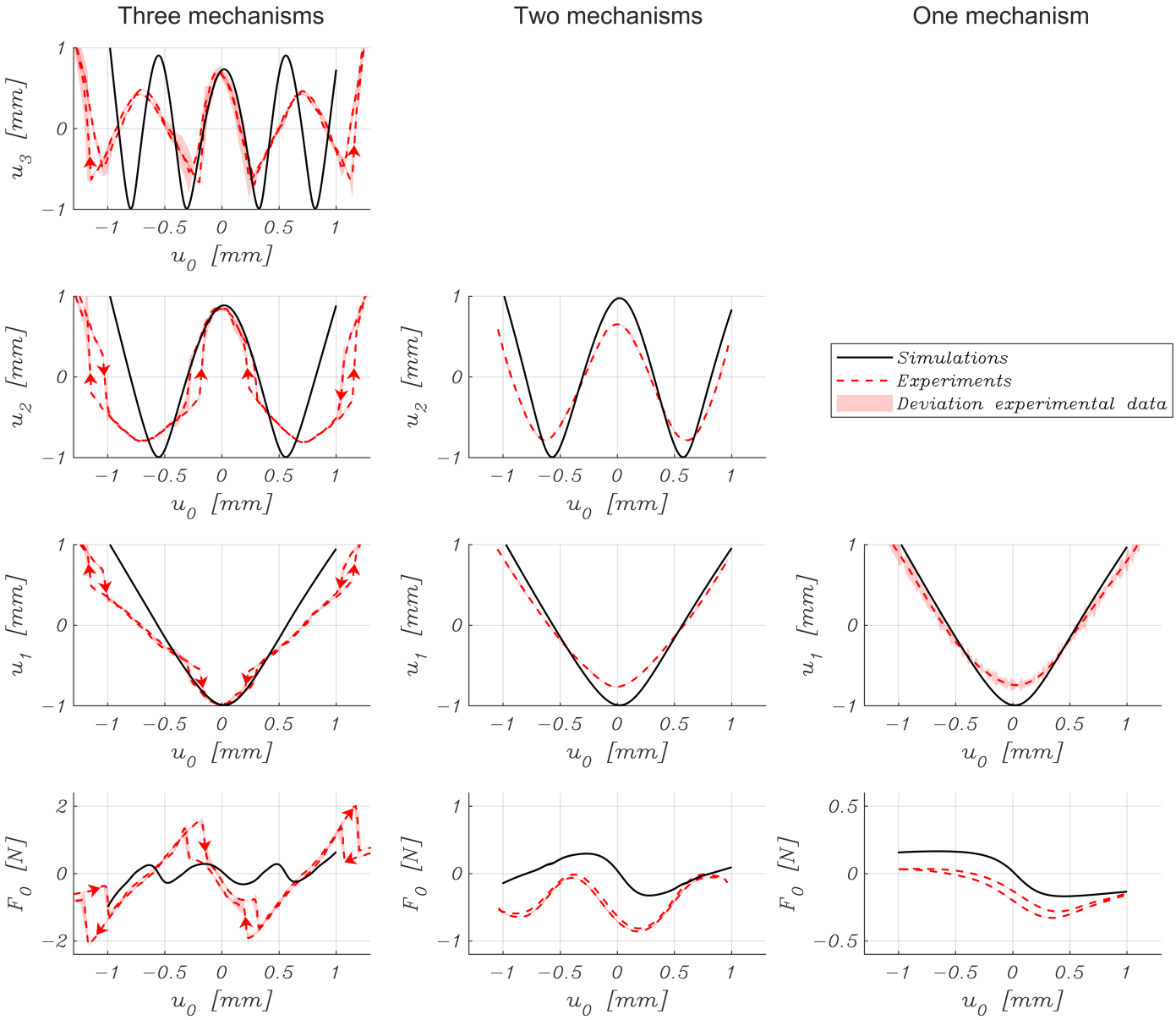

Figure 10: Mechanism behavior for 1, 2 and 3 concatenated mechanisms. Showing results from simulations and prototype. Prototype data was achieved with video tracking and with force sensor. Left column showing the results for 3 concatenated mechanisms, middle column for 2 concatenated mechanism and the right column showing the single mechanism.

to be identified in order to improve the real product for future applications. Reducing the sources of error in the real product will enable higher number of concatenations to really harvest the motion doubling property of the mechanism and achieve a high range of motion.

One notable observation is the improved efficiency observed when concatenating two mechanisms as opposed to a single one. The concatenated mechanism shows higher efficiency than the single one, even though the amount of flexing material is doubled. It is observed that the lost energy is increased for the two mechanisms (100 mJ compared to 71 mJ for the single mechanism), however not at the same rate as the total input energy, meaning the total efficiency has gone up.

4.2 Limitations

Throughout the project, certain limitations have unavoidably emerged, primarily stemming from constraints such as limited time, knowledge, and available equipment. They have been listed below to enable efficient future research and to assess the degree to which the obtained results may be optimizable:

- **Fixed dimensions**
  The thickness and width of the flexures were not optimized but instead based on existing results from the literature, despite their potentially significant impact on the outcomes. Especially the thickness of the flexures can be of significant impact because it relates to the stiffness of the flexures by the third power. It is unknown to what extend this thickness t can optimize the mechanism exactly, but from a brief study considering that the load capacity goes up by t^3 and stress

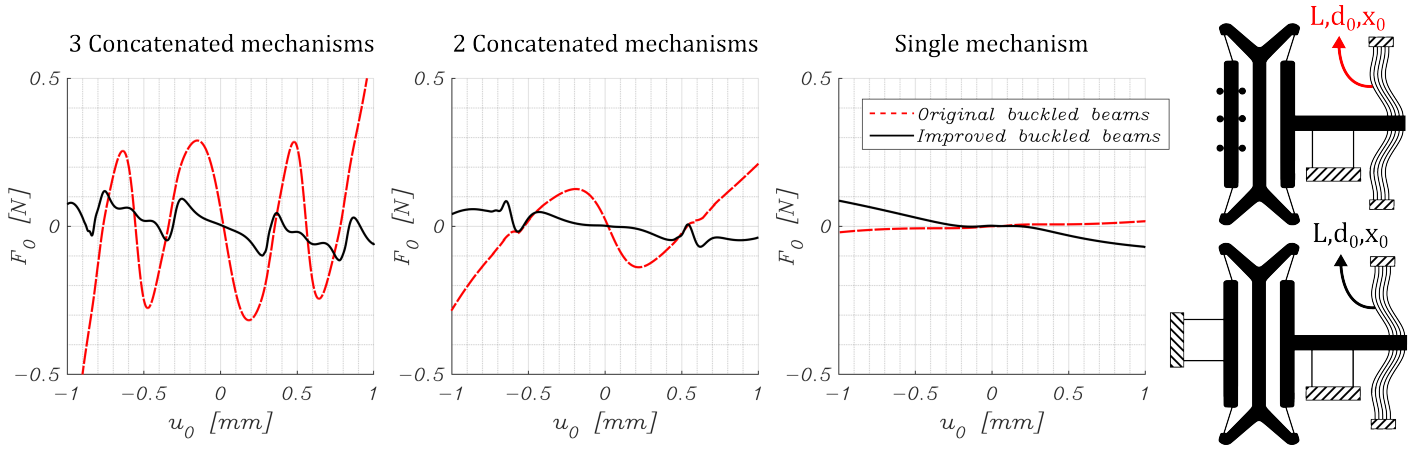

Figure 11: Input force with optimized buckled beams for three concatenated mechanisms. The dimensions of the buckled beams are: $L = 74$ mm, $d_0 = 10$ mm and $x_0 = 13.2$ mm, resulting in a maximum input force of 0.12 N for 3 concatenated mechanisms compared to 0.99 N from original beam dimensions. The new input-output profiles are not shown here because the changes are insignificant ($\leq$2.5%).

by t^2, a thickness of 0.125 mm would increase the load capacity by 13%. This makes use of the fact that the flexure length must increase to reduce the flexure stress, influencing the load capacity which also changes by $(t_{\text{new}} - t_{\text{old}})^3$, refer to supplementary material S.8. For future studies, it is recommended to conduct a more comprehensive examination of these dimensions to precisely identify the best design parameters for the entire mechanism. It's important to note that the thickness and width of the flexures may be constrained by their availability and/or manufacturability.

- **Correlation between remaining forces and design parameters**
  There could be a correlation between remaining forces after static balancing and the design parameters. This possible correlation has been neglected for this project since the remaining forces after static balancing can be a function of a lot of other factors, for example the rigidity of the "rigid" members, the linearity of the output force, the number of flexing beams (due to material damping), the prototype inaccuracies, other assumptions in the design, etc. If we would assume a certain fraction of the input force would be cancelled after static balancing, say 90%, it would make sense to divide the load capacity results by the input force before selecting a design. However, the remaining input force after static balancing depends on so many factors that it is not possible to know to what extend the input force before static balancing correlates to the remaining input force after static balancing.

- **Symmetry assumption of the single mechanism**
  During the parametric optimization phase a symmetric design was assumed to speed up the simulation time and in turn allow for higher grid density design search. This assumption allowed for two times more data since the only half of the range was being simulated instead of the full range. However, later results have indicated that the G.A. is different (±2.5%) on the other side of the mechanism due to the linear stages that are not perfectly linear. This effect is visible in Figure 10 where the G.A. is slightly lower at $u_0 = 1$ mm than at $u_0 = -1$ mm. The amount of variation is believed to be limited but this is a valid limitation to the process chosen in this project in an attempt to reduce the simulation time.

- **Linearity assumption of the input stage**
  This item is similar to the previous one about symmetry assumption, namely the assumption that the input stage acts as a linear stage. The input stage is not perfectly linear which attributes to non-symmetric behavior of the mechanism making the (design selection) simulations an approximation of the real mechanism. This assumption was required to relieve the mechanism from the forces involved to move the input linear stage. In future works, this can be solved by statically balancing the input stage to obtain the motion of the input stage without the forces that influence the kinematics of the mechanism.

- **Force optimization**
  As shown in the method section the buckled beams were optimized to cancel the forces of the simulation with a "perfect" linear input stage. The resulting force (Figure 8) was almost completely zero, whereas the input force in the final mechanism still displays a peak of 0.17 N. This is due to the simulation difference with the linear input stage. This was originally done because optimization of the buckled beams should not remove the forces from the linear input stage, since these forces would be cancelled by the buckled beams of the mechanism in front of it sharing the same linear stage. An improved version of the mechanism is shown in Figure 11 where the dimensions of the buckled beams were optimized for the three concatenated mechanisms (The optimization was conducted primarily on the two concatenated mechanisms and then fine-tuned for the three concatenated mechanisms). This results in a maximum input force of 0.12 N compared to the force of 0.99 N from Figure 10.

- **Prototype inaccuracies**
  Inaccuracies in the fabrication of the prototype have influenced the results and is one of the reasons the prototype does not show the same behavior as the simulations (besides the nonrigid "rigid" elements). An example is

the slots that the buckled beams slide into are a little wider than required which allows the beams to slide in, however it also allows for a slight angular offset which increases the force applied to the mechanisms output stage. This and other fabrication issues contribute to dissimilarities in the results.

4.3 Conclusion

In this research, we focused on the design and concatenation of a compliant frequency doubler to enhance the range of motion of strain energy devices. Our objective was to achieve higher frequency multiplication through the concatenation of frequency doubling mechanisms, enabling a significant increase in motion capability while maintaining a compact size without the drawbacks of conventional transmission systems.

Through systematic simulations and optimization, we successfully designed a compliant frequency doubling mechanism that achieved a near-perfect G.A. of 2, ensuring that the output moved twice the distance of the input. Moreover, the integration of buckled beams into the system allowed for static balancing, effectively reducing the input force to 5.3% of the initial force. The concatenation of three frequency doubling mechanisms was the culmination of our efforts, resulting in a frequency multiplication of 8 with a demonstration prototype to back up the results. Though challenges remain, notably in achieving complete elimination of the input force, our experimental validation showcased the feasibility of the concept.

Future work may focus on a more effective and complete elimination of the input force, allowing a higher number of concatenations. This would really challenge the more straightforward range of motion amplifiers, e.g., common lever mechanisms due to the frequency doubling behavior.

This research lays a foundation for future advancements in compliant mechanisms and frequency multiplication, offering a pathway to enhance the range of motion of elastic energy sources.

References

[1] Robert Bogue. Miniature and microrobots: a review of recent developments. *Industrial Robot: An International Journal*, 42:98–102, 1 2015.

[2] Ben Wang, Yabin Zhang, and Li Zhang. Recent progress on micro- and nano-robots: towards in vivo tracking and localization. *Quant Imaging Med Surg*, 8:461–479, 6 2018.

[3] Jinhua Li and Martin Pumera. 3d printing of functional microrobots. *Chem. Soc. Rev.*, 50:2794–2838, 2021.

[4] J Tromp. Energy storage for microrobotics: A review of energy and power density in relation to size, 2023.

[5] Larry L Howell. Compliant mechanisms. pages 189–216. Springer London, 2013.

[6] Jaroslav Hricko and Štefan Havlík. Compliant mechanisms for motion/force amplifiers for robotics, 1 2020.

[7] Davood Farhadi Machekposhti. Compliant transmission mechanisms, 11 2018.

[8] Luuk Samuels. Parametric study of an elastic singularity-based frequency doubler for concatenation, 3 2023.

[9] Juan Gallego Sanchez and Just Herder. Criteria for the static balancing of compliant mechanisms. volume 2, 10 2010.

[10] Just Herder. Energy-free systems; theory, conception and design of statically balanced spring mechanisms, 11 2001.

[11] P R Kuppens, M A Bessa, J L Herder, and J B Hopkins. Compliant mechanisms that use static balancing to achieve dramatically different states of stiffness. *Journal of Mechanisms and Robotics*, 13, 1 2021.

[12] Mohan Zhao. Is the negative equivalent stiffness of a system possible? *Physics Education*, 51:13002, 12 2015.

[13] Erik Van De Wetering. Stiffness compensation for piezoelectric energy harvesting improving the efficiency at low-frequency vibrations, 1 2022.

[14] Haitong Liang, Guangbo Hao, Oskar Z Olszewski, and Vikram Pakrashi. Ultra-low wide bandwidth vibrational energy harvesting using a statically balanced compliant mechanism. *International Journal of Mechanical Sciences*, 219, 2 2022.

[15] M Rismalia, S C Hidajat, I G R Permana, B Hadisujoto, M Muslimin, and F Triawan. Infill pattern and density effects on the tensile properties of 3d printed pla material. *Journal of Physics: Conference Series*, 1402:044041, 2019.

SUPPLEMENTARY MATERIAL

S.1 Additional information for design criteria

Figure 12 illustrates the effect of concatenating a mechanism with sub-optimal G.A. characteristics. This indicates that the frequency doubling mechanism needs to be designed carefully with a G.A. close to 2 (This is only true in case with concatenation of identical mechanisms). Figure 13 presents how the input force changes when concatenating up to three mechanisms.

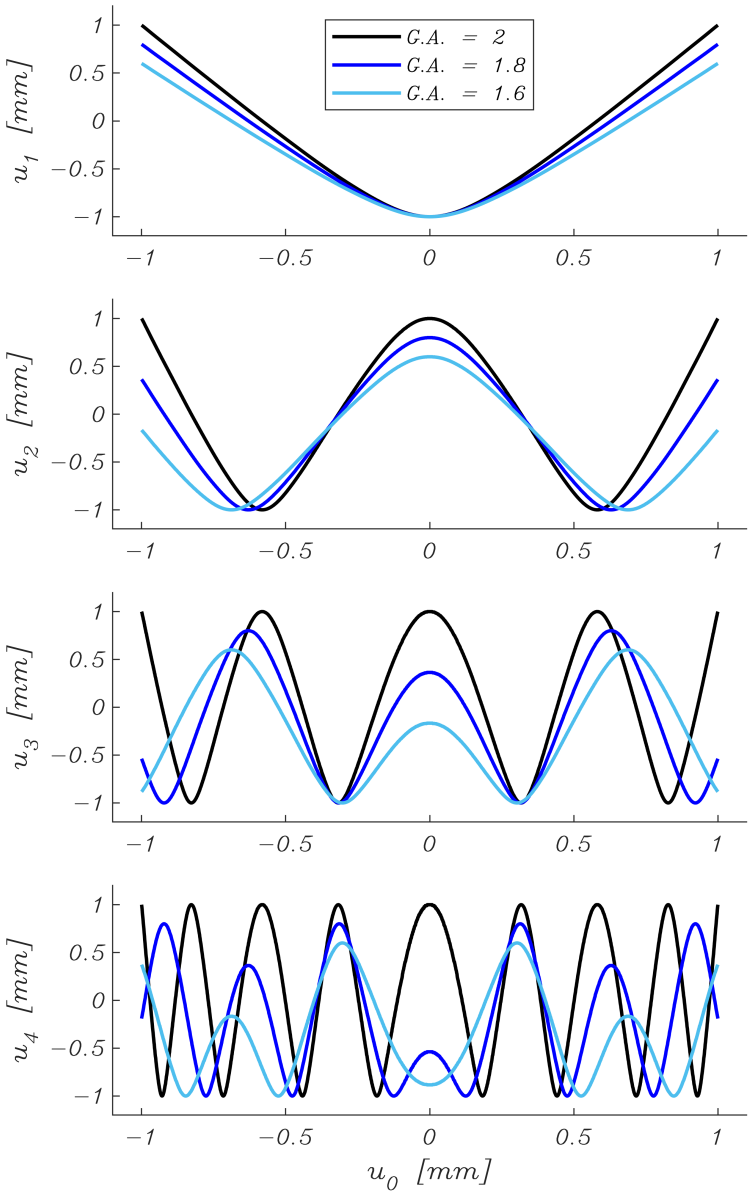

Figure 12: Effect of the G.A. when concatenating up to four frequency doubling mechanisms. With 90% of the perfect G.A. the concatenated system already misses a few frequencies at four concatenations. At 80% of the G.A. of 2 even the third concatenation does no longer show 8-fold frequency multiplication but only 6-fold.

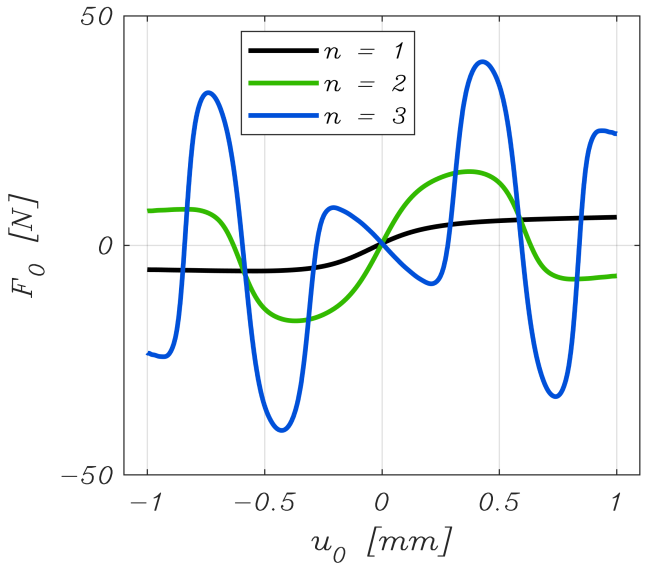

Figure 13: Indicative graph how forces accumulate and multiply when concatenating. A typical input force and input-output profile is used. Input force is max. 6N for a single mechanism, max. 16 N for two mechanisms and peaks at 40N for 3 concatenated mechanisms. This data is made with simulated results from a single mechanism, and then concatenated by a function. For real concatenation the presented forces would alter the input-output relation and therefore change the way forces would be multiplied.

S.2 Calculation of the load capacity

The load capacity is roughly defined as the inverse of the average error from a force on the mechanism. Since the error will be in meters, the unit of the load capacity is N/m, which means it represents the stiffness of the output. Let u_{out} be a vector with length n and a function of F_{out} :

$$u_{\text{out}}\ (F_{\text{out}}\ )$$
$$F_{\text{out}}\ = 1\ \text{N}$$

$$SE = \frac{1}{\text{n}} \sum_{i=1}^{n} \left(u_{\text{out},i}\left(F_{\text{out}}\ = 1\right) - u_{\text{out},i}\left(F_{\text{out}} = -1\right)\right)$$

The error is divided by n to normalize the function for different vector lengths. The total average error is the results of a force of 1 N upwards and 1 N downwards, yielding in a total average output stiffness:

$$k_{out} = \frac{1-(-1)}{SE}$$

Finally, the output stiffness will be normalized by the input stiffness of the linear stage. This ensure that resizing the mechanism will yield similar results. This results in the final formulation of the load capacity:

$$LC = \frac{k_{\text{out}}}{k_{\text{linear stage}}}$$

With:

$$k_{\text{linear stage}}\ = 2 \cdot \frac{12EI}{L_s^3} = 2 \cdot \frac{12 \cdot 190\text{e}9 \cdot 0.01 \cdot 0.0001^3}{12 \cdot 0.032^3} = 115.97\ \text{N/m}$$

During the simulation, the option AUTOTS was set off in ANSYS so that every substep of u_{out} is the same size. This way the error will not depend on the convergence, but it also means that the stepsize needs to be really small for the simulation to not result in an error.

S.3 G.A. initial guess

S.3.1 Introduction

The kinematic properties of the frequency doubling mechanism are defined by the four parameters α, l, l_1 and l_2. One of these is the G.A. which should have a value of two for concatenation. This hard requirement is used to take one parameter from the design space and optimize this parameter such that every design has a G.A. of 2. This greatly reduces the number of simulations because every design will have a G.A. of 2 instead of simulating hundredths of random designs where only a few have the correct G.A.

The optimization cycle will be stopped at a G.A. of 2±0.01 to limit the simulation time. The accuracy of 0.01 is estimated to be orders of magnitude more accurate than the change in G.A. due to undesired but present forces in the mechanism, and also due to errors in the simulation and manufacturing.

In order to start the optimization cycle, an initial guess of the fourth parameter is required. This guess will be based on rigid body calculations with the flexures assumed as rigid with rotational points at the ends, as illustrated by Figure 14.

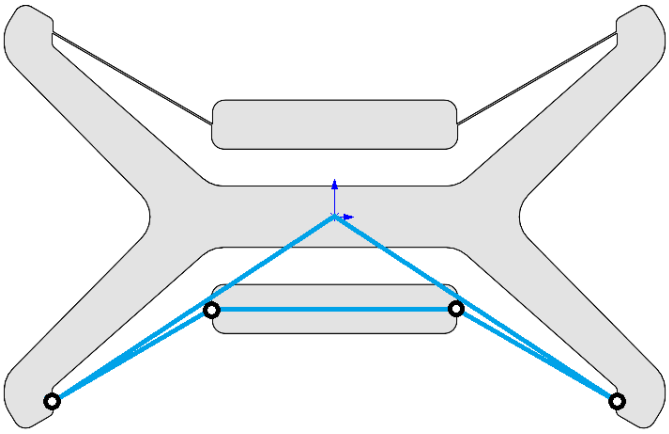

Figure 14: Rigid body simplification. The rigid bodies are illustrated as blue thick lines with rotational joints as circles. The upper two lines are connected and functioning as one rigid body, replacing the middle part of the butterfly mechanism.

S.3.2 Calculation

The rigid body was sketched in SolidWorks where it was proven that the center of the butterfly mechanism exactly moves half the input and output displacements, as illustrated in Figure 15. This allows for great simplifications of the calculations since now only half the mechanism needs to be considered.

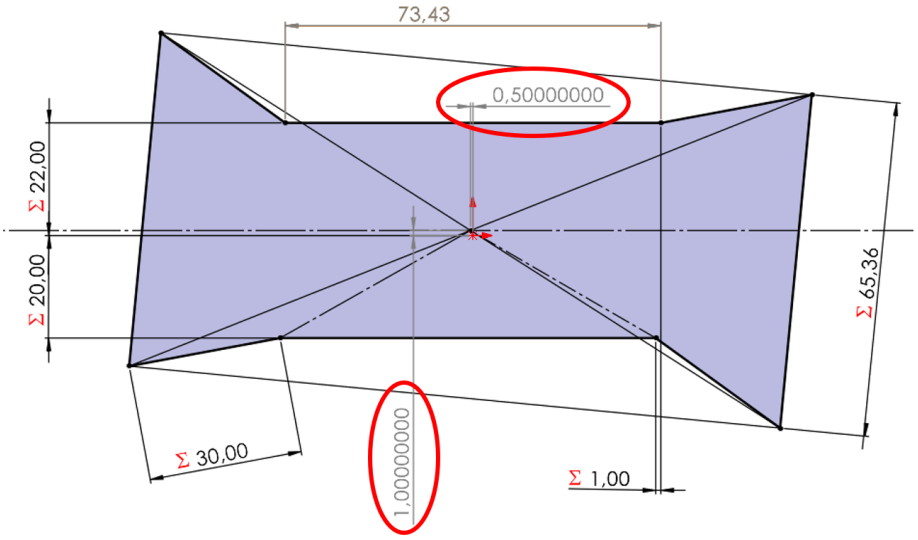

Figure 15: SolidWorks sketch for calculation. The red encircled dimensions are the output displacements as a function of the input dimensions in the sketch. An input of 1mm is given (bottom right) and an output of 2mm (22.00mm - 20.00mm). For all combinations of α, l, l_1 and l_2 it gives the same displacements at the output. Only three parameters were given as an input; l_1 was calculated by the program itself, to not make it over defined.

With this information it was possible to create a set of equations that were solved with MATLAB. The equations are a function of the variables illustrated in Figure 16.

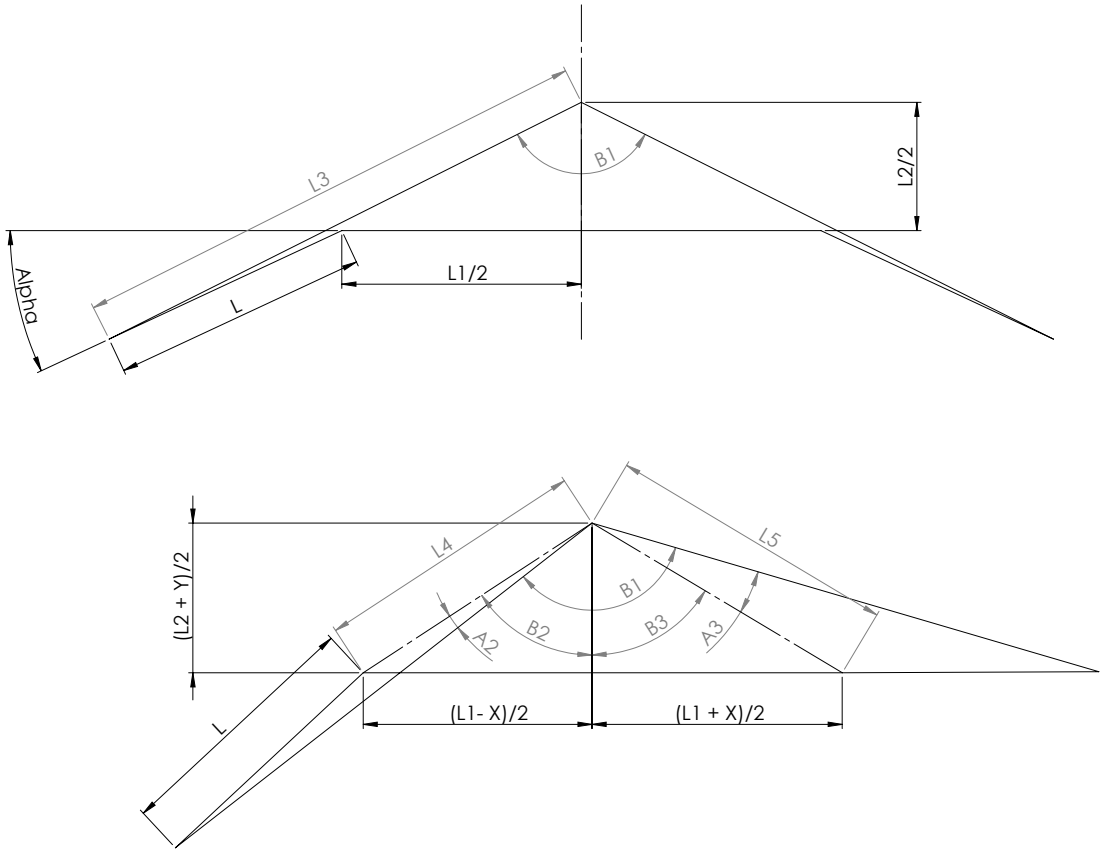

Figure 16: Variables for G.A. initial guess calculation. Top half of the figure shows the "undeformed" state, bottom half illustrates the "deformed" state.

The input and output displacement are defined by x and y respectively (10):

$$\begin{aligned} x &= 1 \text{ mm} \\ y &= 2 \text{ mm} \end{aligned} \tag{10}$$

From the undeformed state we get:

$$\beta_1 = 2\tan^{-1}\left(\frac{l\cos(\alpha) + \frac{l_1}{2}}{l\sin(\alpha) + \frac{l_2}{2}}\right) \tag{11}$$

$$l_3 = \sqrt{\left(l\cos(\alpha) + \frac{l_1}{2}\right)^2 + \left(l\sin(\alpha) + \frac{l_2}{2}\right)^2} \tag{12}$$

From the deformed state we get:

$$\begin{aligned} l_4 &= \frac{1}{2}\sqrt{(l_2+y)^2 + (l_1-x)^2} \\ l_5 &= \frac{1}{2}\sqrt{(l_2+y)^2 + (l_1+x)^2} \\ \alpha_2 &= \cos^{-1}\left(\frac{l_3^2 + l_4^2 - l^2}{2l_3l_4}\right) \\ \alpha_3 &= \cos^{-1}\left(\frac{l_3^2 + l_5^2 - l^2}{2l_3l_5}\right) \\ \beta_2 &= \tan^{-1}\left(\frac{l_1 - x}{l_2 + y}\right) \\ \beta_3 &= \tan^{-1}\left(\frac{l_1 + x}{l_2 + y}\right) \end{aligned} \tag{13}$$

For the displaced case, we can calculate β_1 as the sum of the other angles, which gives:

$$\beta_1 = \alpha_3 + \beta_3 + \beta_2 - \alpha_2 \tag{14}$$

β_1 must be equal in both initial and displaced position since it defines the angle in a rigid body. Combining equation (11) and (14) yields:

$$2\tan^{-1}\left(\frac{l\cos(\alpha) + \frac{l_1}{2}}{l\sin(\alpha) + \frac{l_2}{2}}\right) = \alpha_3 + \beta_3 + \beta_2 - \alpha_2 \tag{15}$$

S.3.3 Parameter elimination

With equation (15) one of the four parameters can be calculated based on the other three. Any parameter can be eliminated, but we prefer to have the ranges of l and α in hand and not based on calculations. The choice for elimination of parameter l_1 or l_2 is arbitrary, we have chosen to eliminate l_1.

Neither the symbolic nor the numerical solution was found with Matlab. This is probably due to α_2 showing discontinuity, sometimes close to the solution. However, it was possible to plot both sides of the equal sign as a function of l_1 and literally see the point of intersection. Therefore, a short script was written to find this intersection numerically, providing the solution for l_1.

S.3.4 Further optimization

One parameter has now been eliminated from the whole design space and every presented solution should have a G.A. of 2. However, the calculation is not perfect, it only provides an initial guess which would give results close to a G.A. of 2. If the solution does not have a G.A. of 2±0.01, another iteration was conducted with compensation for the error in G.A. To do that the remaining error in G.A. was taken to calculate l_1 again, but now with a new y value (from Eq.(10)) defined as:

$$y_{sim2} = y_{sim1} \cdot \frac{2}{G.A._{sim1}} \tag{16}$$

This provides another guess as a function of the G.A. from the first simulation. If the G.A. is within the requirements the optimization cycle will end here. If not, this new guess will define a gradient of the G.A. with respect to the parameter l_1, enabling us to guess a third value for l_1 as shown in Figure 17.

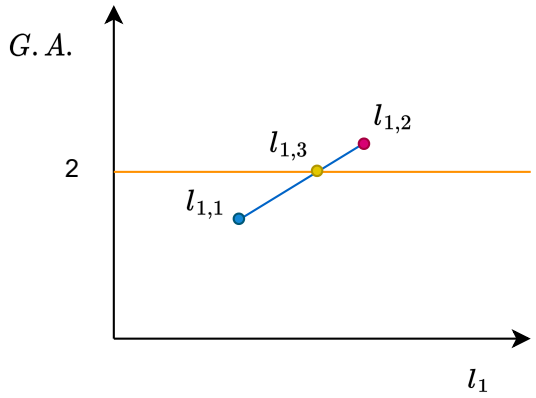

Figure 17: Linear interpolation of parameter l_1. The y-axis shows the G.A., which should converge to 2. The third guess of l_1 is a linear interpolation between $l_{1,1}$ and $l_{1,2}$.

This process is repeated until the G.A. converged to a G.A. of 2±0.01. Every new simulation adds an order to the interpolating function. All solutions converged before or at the fifth cycle.

S.4 Design selection simulations

S.4.1 Simulation procedure

For all data points in the range, three types of simulations are done and explained in this section. A flow chart is provided on the next page with the whole process explained visually, refer to Figure 18.

Simulation #1

- **Description**
  Find l_1 for G.A. = 2

  Since the G.A. of 2 is such a hard requirement, each mechanism is optimized for a G.A. of 2. This simulation uses a different code than simulations 2 and 3 to get a shorter simulation time.
- **Input**
  α l l_2
- **Output**
  l_1
- **Method**
  The mechanism is first displaced with a small u_{in} to get through the singularity and then a displacement u_{out} is applied of 4 mm. Theoretically u_{out} only has to be 2 mm, but this causes problems when the initial guess of parameter l_1 leads to a G.A. higher than 2. An output displacement of 4 mm was determined to be adequate in guaranteeing that u_{in} achieved a minimum of 1 mm in all simulations.

  The first simulation is run with $l_{1,1}$ which is calculated with y_{sim1}=1.6 mm. Theoretically this should be 2 mm, but 1.6 mm turned out to provide better initial guesses. After the first simulation, we get the corresponding geometrical advantage; $G.A._1$. For the second simulation we need a second guess for l_1. Any guess will be valuable to get the slope l_1/G.A. but we calculate $l_{1,2}$ by using equation (16).

Simulation #2

- **Description**
  Find Input Output profile
- **Input**
  α l l_1 l_2
- **Output**
  u_{in} u_{out} F_{out} σ_{max}
- **Method**
  For simulation 1 we already simulated the input output displacement, but this was done as fast as possible with big time steps. For simulation 2, we perform a separate simulation for this with smaller time steps for high resolution results. The mechanism is displaced on the output side, and this also provides F_{out} which is the force required to actuate the mechanism on the output side. It should not be confused with a certain output force obtained from a certain input force. A statically balancing device will later deliver this actuating force to statically balance the mechanism.

Simulation #3

- **Description**
  Obtain the load capacity.
- **Input**
  α l l_1 l_2 F_{out}
- **Output**
  $u_{out,F=1}$ $u_{out,F=-1}$ $\longrightarrow$ To calculate the load capacity
- **Method**
  We start by applying a linear approximation of the output force from simulation 2 on the output of the mechanism. This linear output force serves as a replacement of the statically balancing device that will be present in the final design. Then we add a positive force of 1 N on the output and run the simulation. Then we add a negative force of 1 N on the output and run the simulation. The results of the simulation are the (deformed) input output profiles, which are used to calculate the load capacity. The force of 1 N is an estimate of what the magnitude of force would be after 3 statically balanced concatenated mechanisms.

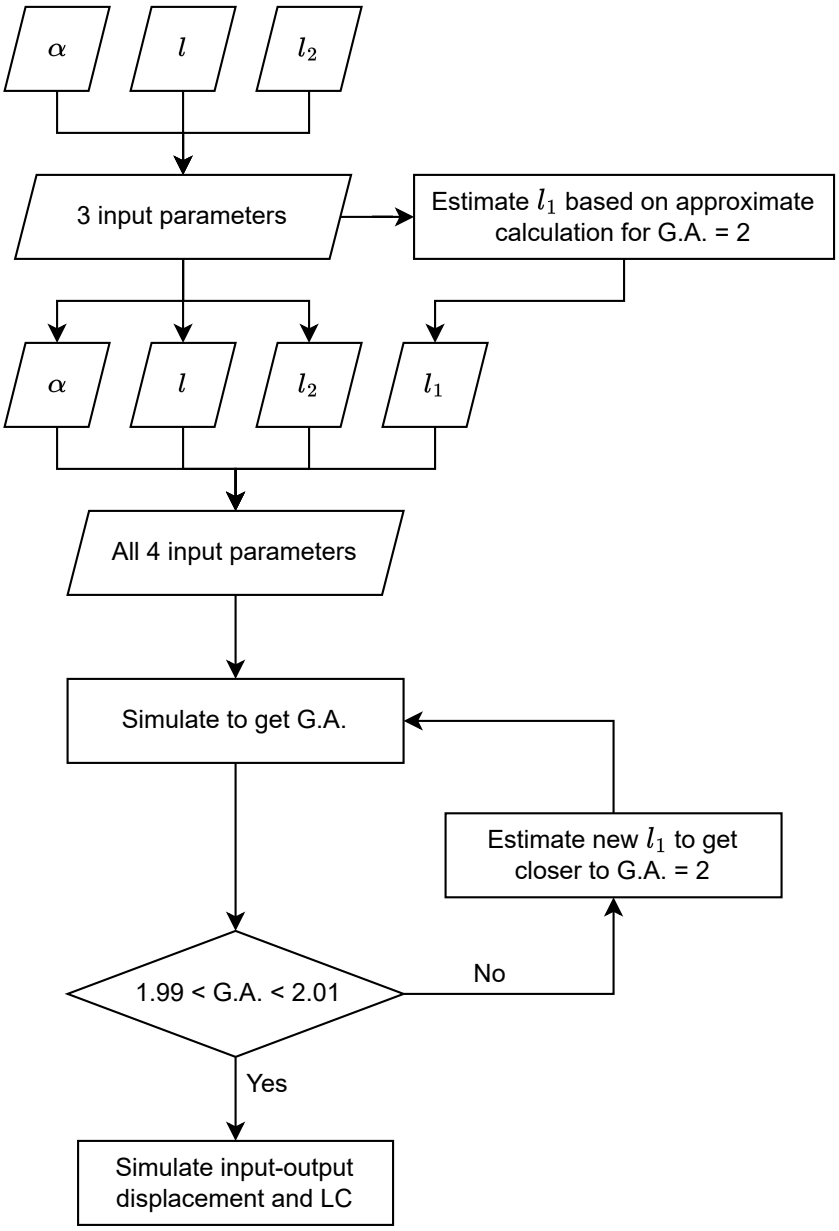

Figure 18: Flow chart of design selection simulation 1. It starts on top, with three parameters. The process continues as illustrated and ends with the simulations #2 and #3 after the G.A. of 2 has been attained.

S.4.2 Simulation dimensions and settings

Table 1 provides the settings used for the simulations during the design selection phase. Figure 19 provides the general placement of the keypoints and beam elements as they were used in the simulation. Point 12 is the input, point 17 the output. The gap between each plane (input stage plane, butterfly plane, output stage plane) is 2 mm.

General inputs/settings	Description	Explanation
Element type	BEAM188 & MPC184	Beam188 is based on Timoshenko beam theory, suitable for simulating slender to moderately thick beams. According to the ANSYS APDL documentation this element is well-suited for linear, large rotation, and/or large strain nonlinear applications. MPC184 is a rigid element, used for the rigid parts of the mechanism.
Elements along length	30	Number of elements along length of the flexures.
Elements in cross-section	2 x 2 = 4	Rectangular elements with 2x2 elements in the cross-section. (Each beam is therefore a beam with 2x2x30 = 120 elements)
Width of flexure (z-direction)	10 mm	This dimension is fixed during the whole project.
Thickness of flexure	0.1 mm	This dimension is fixed during the whole project.
Solver settings		
Number of substeps	50 (Sim 1) 200 (Sim 2) 300 (Sim 3)	For simulation 1, the number of substeps is 50 with AUTOTS on for a short simulation time. Simulation 2 and 3 were simulated with more substeps with AUTOTS off.
AUTOTS	ON (Sim 1) OFF (Sim 2) OFF (Sim 3)	The substeps are kept constant in the second and third simulations, in order to correctly calculate the properties of the curves, especially the for the load capacity.
NLGEOM	ON	Set the nonlinear geometry option to ON to include large deflection effects.
NEQIT	50	Allow more (50) substeps per iteration for non-linear analysis.

Table 1: Settings of the simulations.

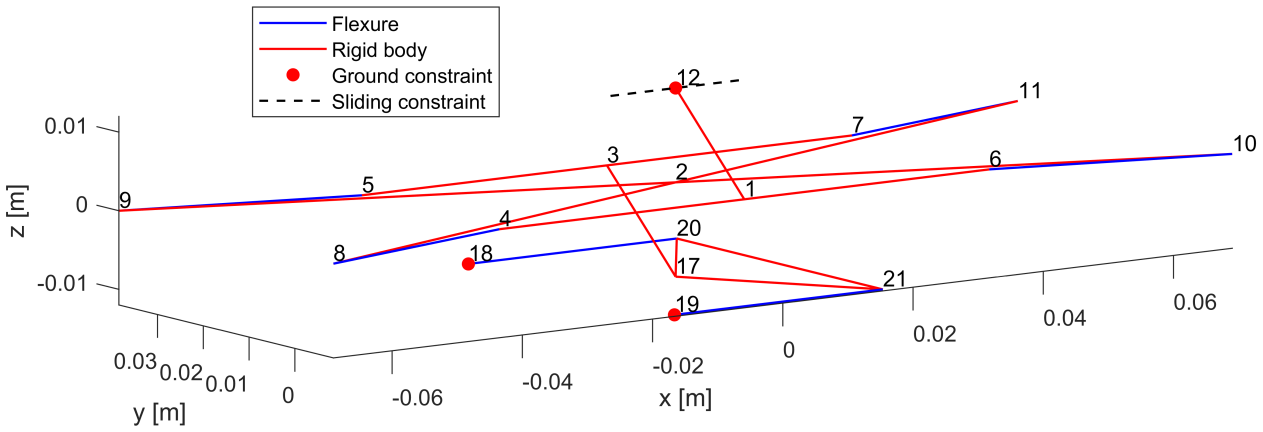

Figure 19: Keypoints and beams of ANSYS simulation. The red lines represent the rigid MPC184 beams, the blue lines the BEAM188 type beams.

S.5 Statically balanced design simulations

This material describes the statically balanced mechanism simulations of the single- and concatenated mechanism(s).

S.5.1 Keypoints and beam elements

Due to the amount of keypoints, a code in Matlab was made to supply the keypoints and lines for ANSYS. The first mechanism was similar to the simulated mechanism during parametric optimization. The second mechanism would turn by 90 degrees and displace in z-direction. The third is in the same orientation of the first, only displaced in z-direction. Figure 20 provides the general placement of the keypoints and beam elements as they were used in the simulation. The keypoints of each successive mechanism are enumerated by adding 100 to the keypoint number of the previous mechanism.

S.5.2 Material properties

PLA printed with 100% infill has a Young's modulus of about 3500 Mpa. However, its Youg's modulus decreases when printing with 30% infill. A research on printed PLA with a testbar of 13 mm, which is in the same range as the dimensions of our prototype, conducted tests on 25%, 50% and 75% grid infill [15]. Their results show a Young's modulus of 2770 Mpa by linear interpolation between 25% and 50% infill.

$$
\begin{aligned}
E_{\text{PLA}} &= 2.77\,(10^9)\ \text{Pa} \\
\nu_{\text{PLA}} &= 0.35 \\
E_{\text{AISI301}} &= 190\,(10^9)\ \text{Pa} \\
\nu_{\text{AISI301}} &= 0.27
\end{aligned}
$$

S.5.3 Simulation settings

Table 2 provides the settings used for the simulations of the statically balanced mechanism.

General inputs/settings	**Description**	**Explanation**
Element type	BEAM188	This beam element is based on Timoshenko beam theory, suitable for simulating slender to moderately thick beams. According to the ANSYS APDL documentation this element is well-suited for linear, large rotation, and/or large strain nonlinear applications.
Elements along length	30	Number of elements along length of the flexures.
Elements in cross-section	2 x 2 = 4	Rectangular elements with 2x2 elements in the cross-section. (Each beam is therefore a beam with 2x2x30 = 120 elements)
Width of flexure (z-direction)	10 mm	This dimension is fixed during the whole project.
Thickness of flexure	0.1 mm	This dimension is fixed during the whole project.
Solver settings		
NSUBST	400 (1 mech) 400 (2 mech) 2000 (3 mech)	For a single and double mechanism, the number of substeps is 400. For three concatenated mechanisms, the number is increased to 2000 in order to get a converging simulation.
AUTOTS	OFF	The substeps are kept constant for convenience of later processing of the data.
NLGEOM	ON	Set the nonlinear geometry option to ON to include large deflection effects.
NEQIT	50	Allow more (50) substeps per iteration for non-linear analysis.

Table 2: Settings of the simulations.

S.5.4 Simulation solve steps

This section provides detailed insight in the solution steps for the simulation of three simulations. The solve steps can be categorized by three separate stages: 1. Constrain and couple nodes. 2. Preload each mechanism by displacing the output and couple corresponding nodes in correct positions. 3. Displace input and get the resulting output displacement and input force.

- **Initialize:** Before any solve steps some nodes will be coupled with other nodes by their displacement and rotations. The x- and z-displacements and all rotations of nodes 17 and 22 are coupled (Coupling is a command in ANSYS that can couple degrees of freedom from multiple nodes so that they function as a set with the same displacements/rotations). This ensures that the output of the first mechanism is linearly guided by the output stage of the first mechanism, while still having the ability to be preloaded which will happen later in the process. Similarly, nodes 117 and 122 are coupled (leaving only the x-direction uncoupled) and nodes 217 with 222 (leaving the y-direction uncoupled).
- **Solve step 1:** Constrain all nodes that are fixed to the ground and pre-compress and pre-displace the buckled beams. Furthermore, move input node 12 by 1mm in x-direction and fix all other linear stages in the direction of motion (nodes 17, 117 and 217).
- **Solve step 2:** Fix y-displacement of node 22 to its current position.
- **Solve step 3:** Delete x-constraint of (input) node 12 and move y-displacement of node 22 to 1 mm.
- **Couple mechanism 1:** The output of the first mechanism can now be coupled to the output stage of the first mechanism (Couple y-displacement of node 17 to 22).
- **Solve step 4:** Delete y-constraint of node 17 and displace node 22 in y-direction by 2 mm. This puts the second mechanism in displaced position.
- **Solve step 5:** Fix x-displacement of node 122 to its current position.
- **Solve step 6:** Delete y-constraint of node 22 and move node 122 to -1 mm in x-direction.
- **Couple mechanism 2:** The output of the second mechanism can now be coupled to the output stage of the second mechanism (Couple x-displacement of node 117 to 122).
- **Solve step 7:** Delete x-constraint of node 117 and displace node 122 in x-direction by -2 mm. This puts the third mechanism in displaced position.
- **Solve step 8:** Fix y-displacement of node 222 to its current position.
- **Solve step 9:** Delete x-constraint of node 122 and move node 222 to 1 mm in y-direction.
- **Couple mechanism 3:** The output of the third mechanism can now be coupled to the output stage of the third mechanism (Couple y-displacement of node 217 to 222).
- **Solve step 10:** Fix x-displacement of input node 12 to its current position.
- **Solve step 11:** Delete y-constraints of nodes 217 and 222.
- **Solve step 12:** Move input node 12 to 1 mm in x-direction.
- **Solve step 13:** Move input node 12 to -1 mm in x-direction.
- **Solve step 14:** Move input node 12 to 1 mm in x-direction.

The input displacement, output displacement and input force from steps 13 and 14 were saved as results from the simulation.

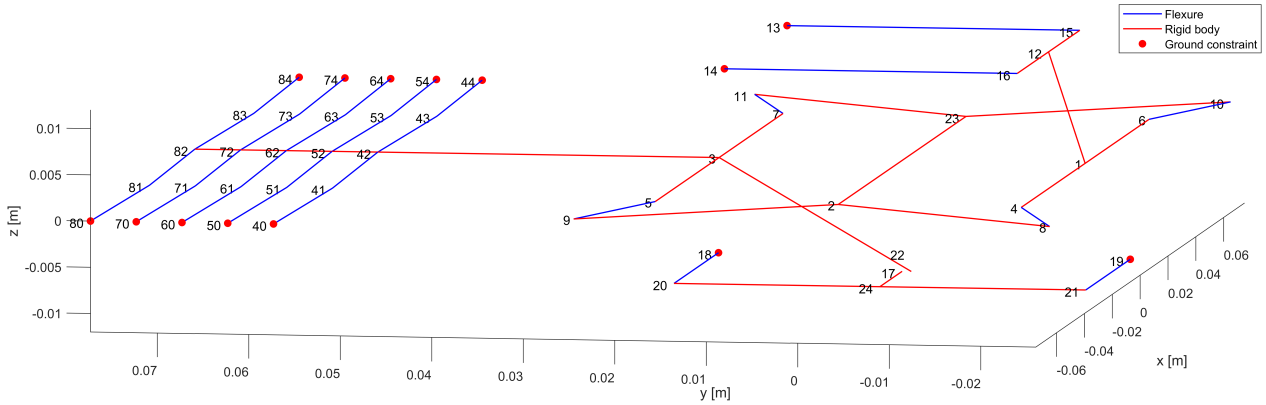

(a) Keypoints and beams one mechanism.

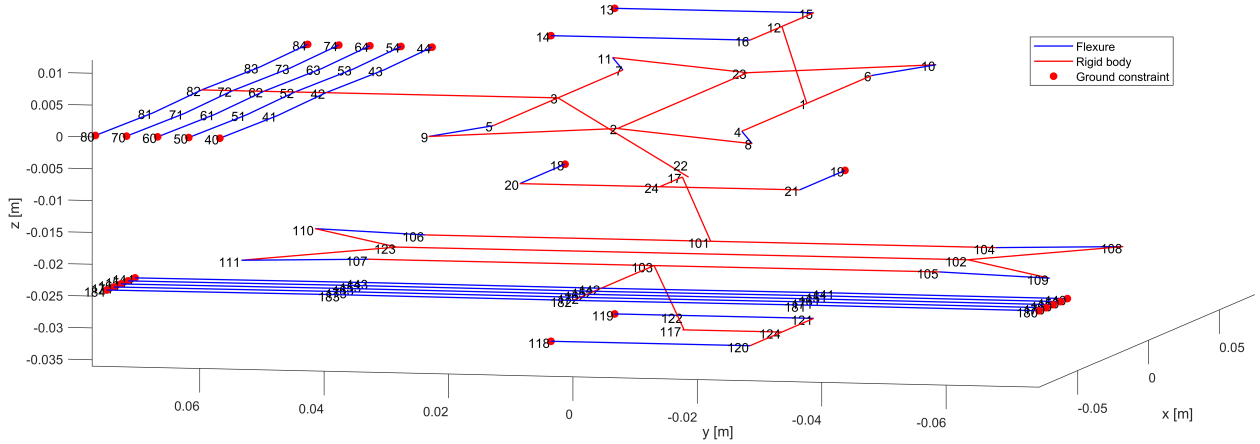

(b) Keypoints and beams two mechanisms.

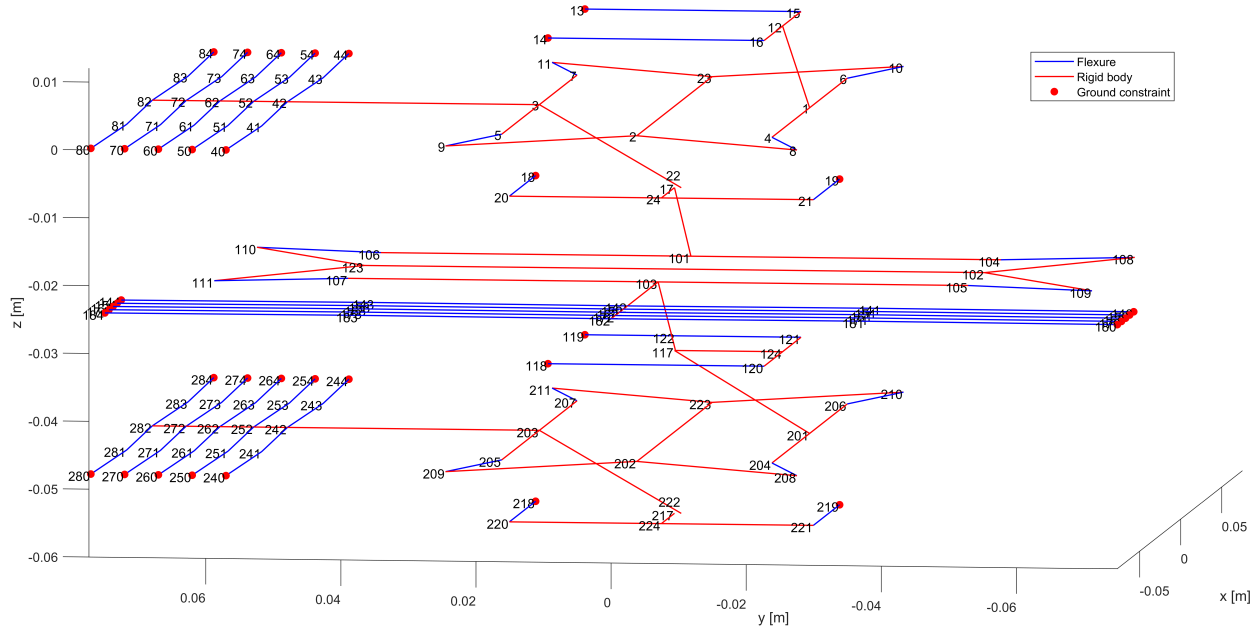

(c) Keypoints and beams three mechanisms.

Figure 20: Keypoints and beams for the statically balanced ANSYS simulations. In red the rigid beams, which resemble the rigid PLA parts of the prototype. The rigid beams are not real rigid beams, but actually high-stiffness beams from PLA. The blue lines represent the flexural members of the mechanism from hardened stainless steel.

S.6 Additional results

Figure 21 shows the parameter combination that result in a G.A. of 2, the color determines the parameter l_1, which was found during the optimization process as a function of the other parameters. Figure 22 is another representation of the same data that identifies other relations between the parameters.

Figure 23 provides the Normalized load capacity for all parameter combinations. l_1 is not found in this tile plot since this is a function of the other three parameters. It is observed that the load capacity increases when the flexure length l decreases. Furthermore, the highest load capacity designs tend towards an α of 15 to 20 degrees.

Figure 24 provides the load capacity results as a function of the horizontal and vertical size of the mechanism, which was primarily used in the selection of the final set of parameters together with Figure 23.

Figure 26 provides the input-output relation for the statically balanced (single) mechanism and non-statically balanced mechanism.

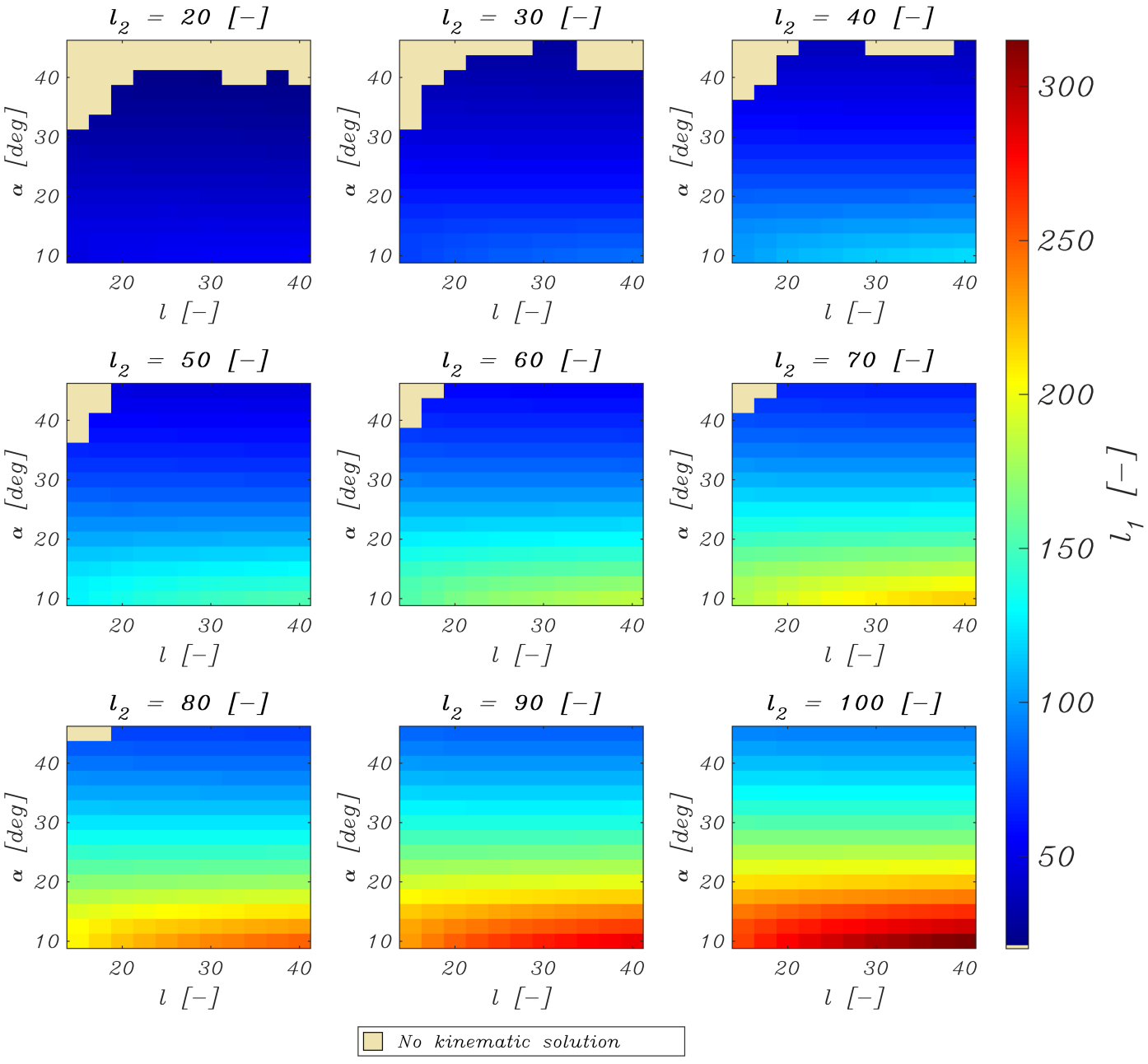

Figure 21: Tile plot of parameter combinations for a G.A. of 2. Areas indicated by "No kinematic solution" illustrate simulations where no length l_1 was found to make the G.A. equal to 2. All other results converged to a G.A. of 2. The stress limitation of $\sigma \geq 500$ Mpa is not considered in making this plot meaning that all results are provided here to clearly indicate the relation between the parameters.

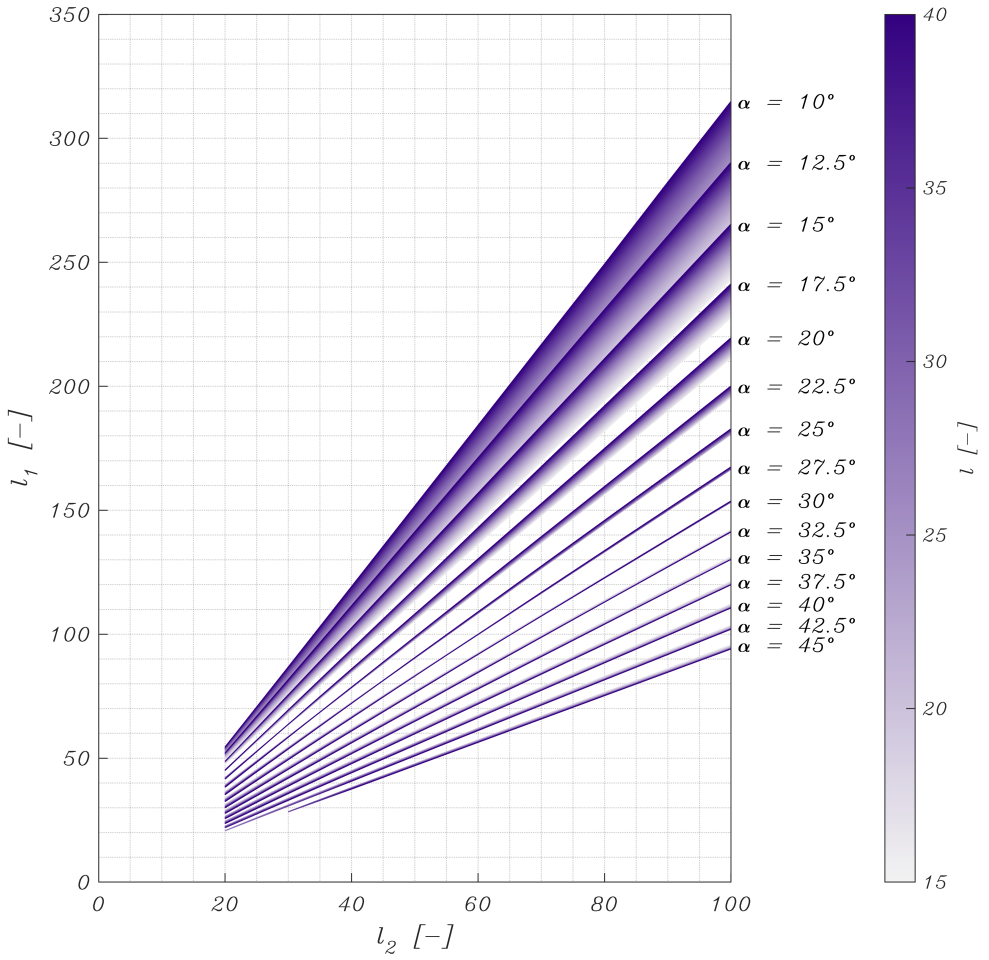

Figure 22: A different representation of the parameter combinations that produce a G.A. of 2. Surfaces of the data points with constant α are meshed as a function of l, l_1 and l_2 and then mapped onto the 2D-plane l_1, l_2. The colorbar indicates different values for flexure length l.

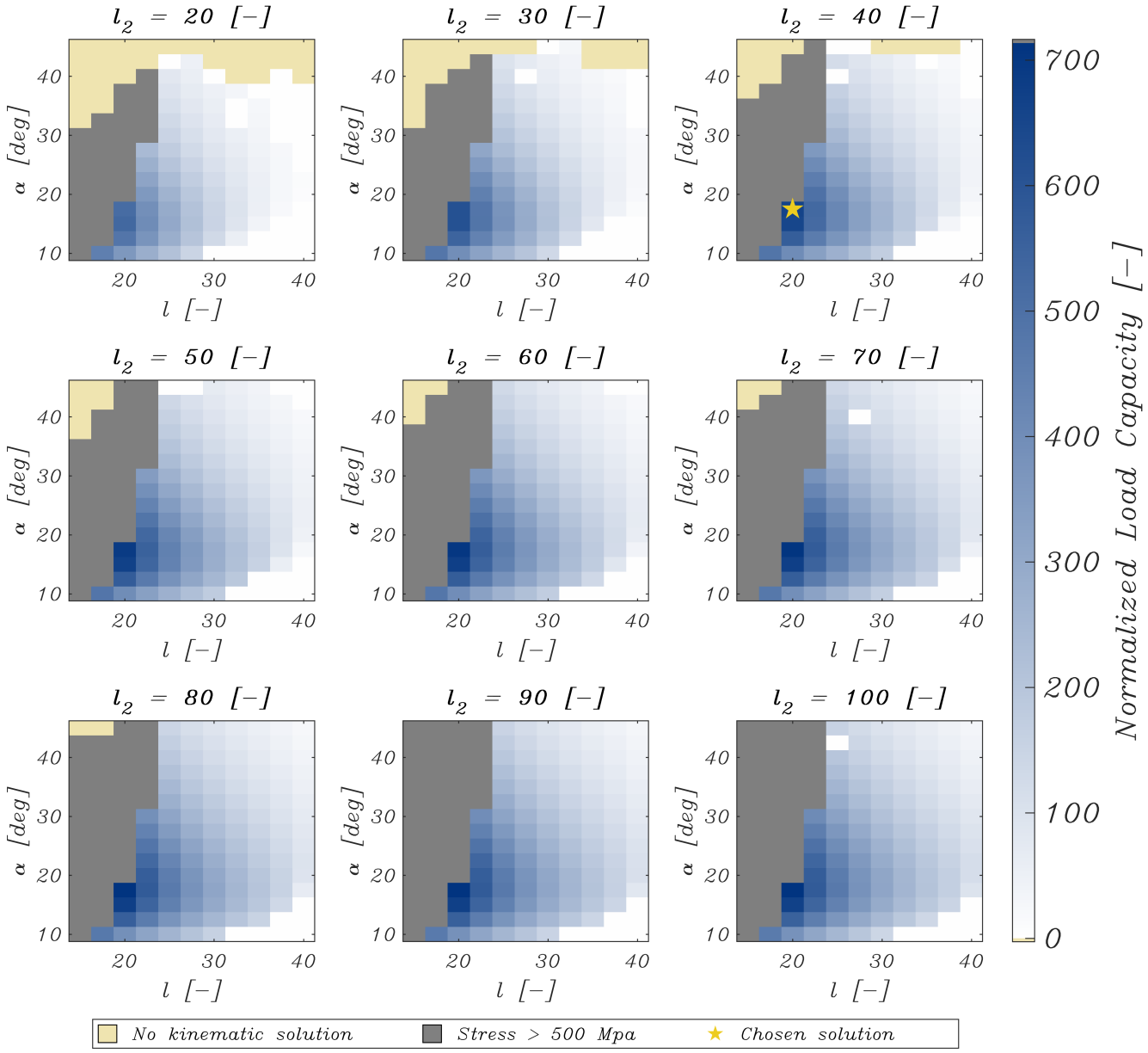

Figure 23: Tile plot of Normalized Load Capacity as a function of the parameters. In grey the results where the stress was too high.

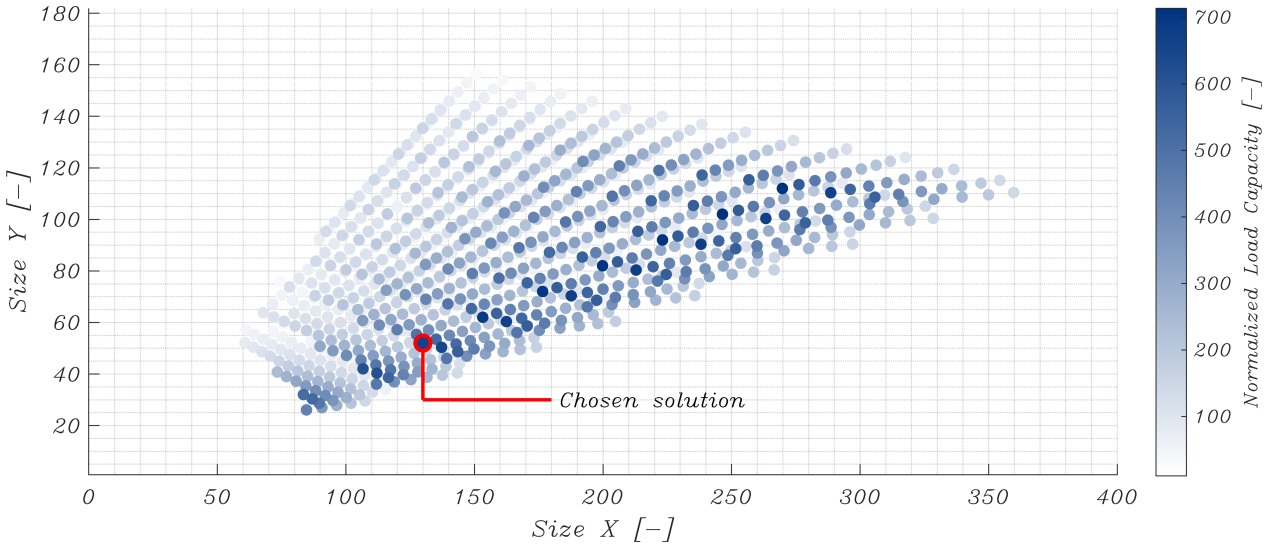

Figure 24: Load Capacity v.s. Size. Size is solely a function of the parameters, neglecting any extra size from the frame to hold the flexures in place. Size X is the length l_1 plus the horizontal component from l ($l\cos\alpha$). Size Y is the length l_2 plus the vertical component from l ($l\sin\alpha$).

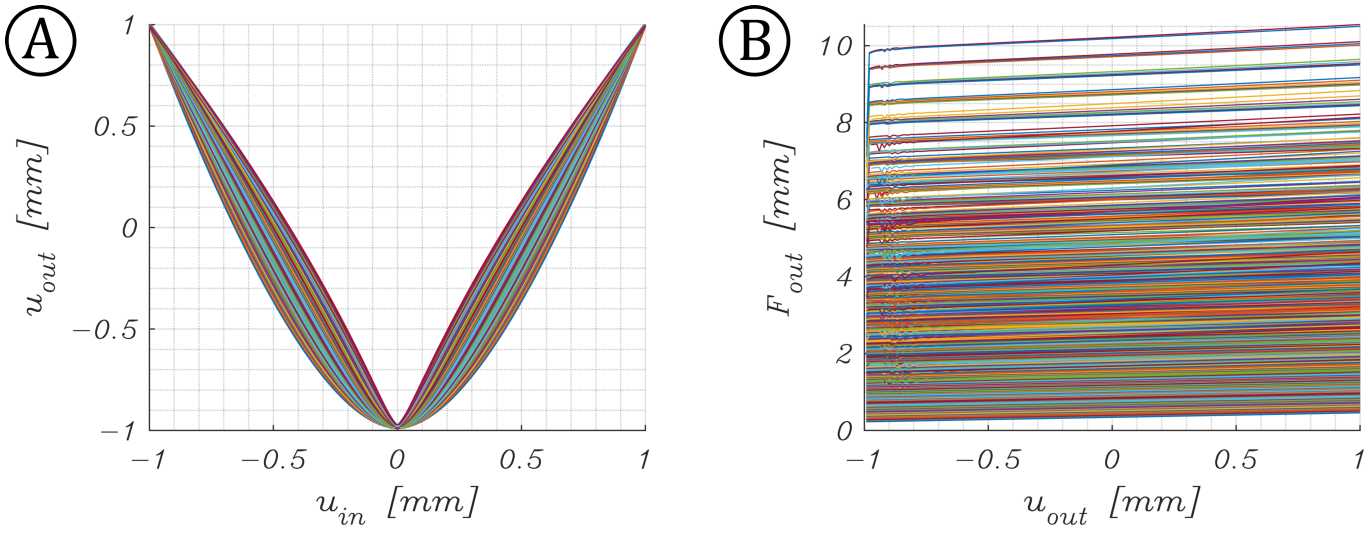

Figure 25: Graph of displacement- and force-profiles for all parameter combination. **(A)** Input-output displacement and **(B)** force at output stage. (Some solutions are overlapped by other solutions)

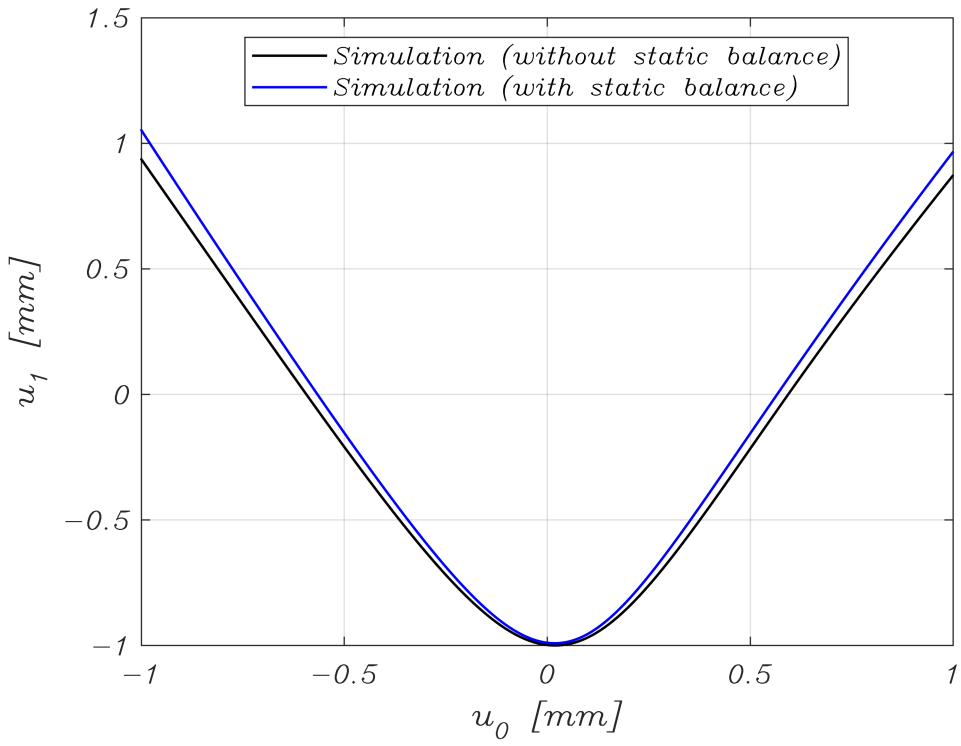

Figure 26: Single mechanism before and after static balancing. Results for a single mechanism from simulations with perfect sliding input stage.

Videos

Link to videos: https://1drv.ms/f/s!AuFKEiGsd8cUhVkDKds8xweHasyb?e=raxQup

A1. Video of 1 mechanism
A2. Video of 2 mechanisms
A3. Video of 3 mechanisms
A4. Video of 3 mechanisms (pretty)
A5. Animation of simulation for 1 mechanism
A6. Animation of simulation for 2 mechanisms
A7. Animation of simulation for 3 mechanisms

S.7 Prototype fabrication and assembly

The rigid parts of the mechanism have been designed in Solidworks and printed with the 3d-printer named PRUSA MINI+ from PLA. The flexible beams were bought from a supplier and were made from AISI301 with full hard treatment, making up for the high tensile stress. Materials and print settings are listed below:

Materials:

- ECOPLA-WHITE (Print temperature: 195-215°C)
- AISI301 Full hard (AMS 5519)

3D Print settings for the PLA (PRUSA MINI+):

- Filament temperature 215°C
- Bed temperature 60°C
- Nozzle diameter 0.4 mm
- Layer height 0.15 mm
- Infill 30% (grid)

Glue:

- Bison super glue

S.7.1 Assembly method

To ensure high precision of the assembly of the steel flexures to the plastic 3D-prints, the plastic parts were printed as one part with thin plastic beams connecting them. The thin beams were later cut away once the flexures were glued in place. Figure 27 illustrates the assembly method of the 3D printed parts. All parts have been fabricated the same way.

Bolts and nuts (M4) were used to connect all the parts together, enabling rapid prototyping by allowing us to change parts during the process of testing. This has also been useful for testing multiple concatenations with the same parts, just by screwing the next mechanism to the previous one.

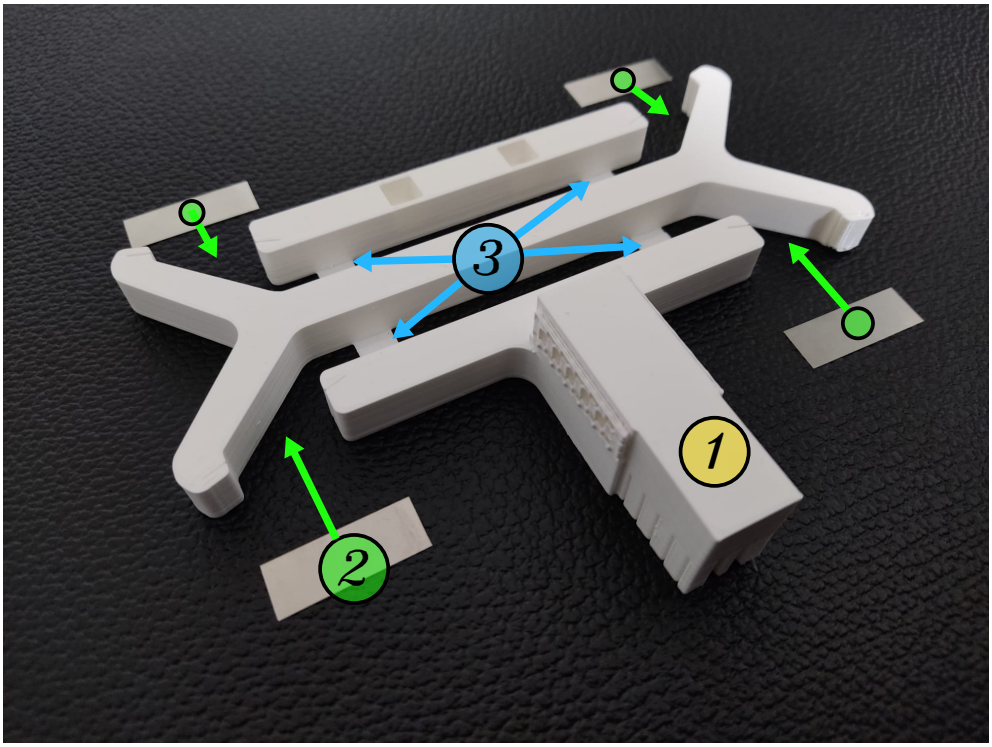

Figure 27: Fabrication butterfly mechanism. (1) The printed part from white PLA. **(2)** The leaf flexures from spring steel that will fit in the slots from part 1. **(3)** Thin members incorporated in the design to keep the PLA part in one piece for correct relative positioning of the PLA parts. These are cut away after the flexures have been glued in place.

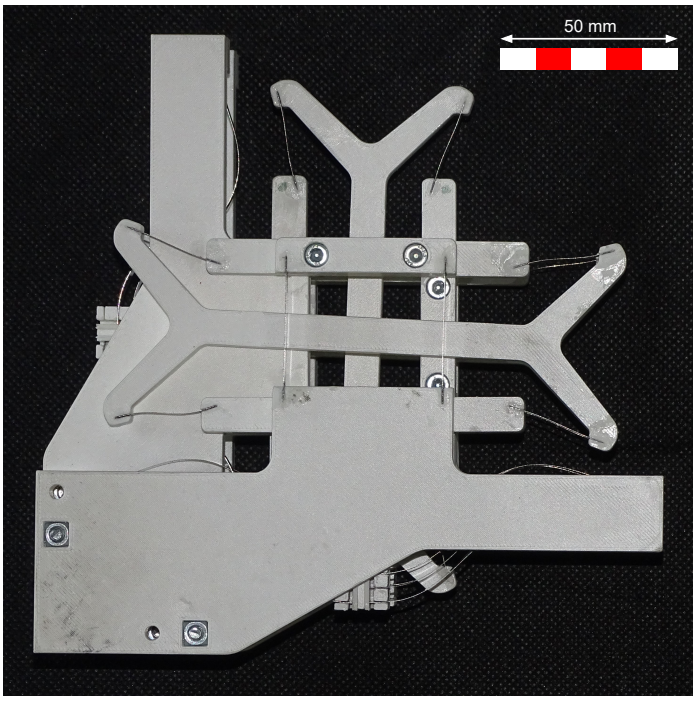

(a) Front view

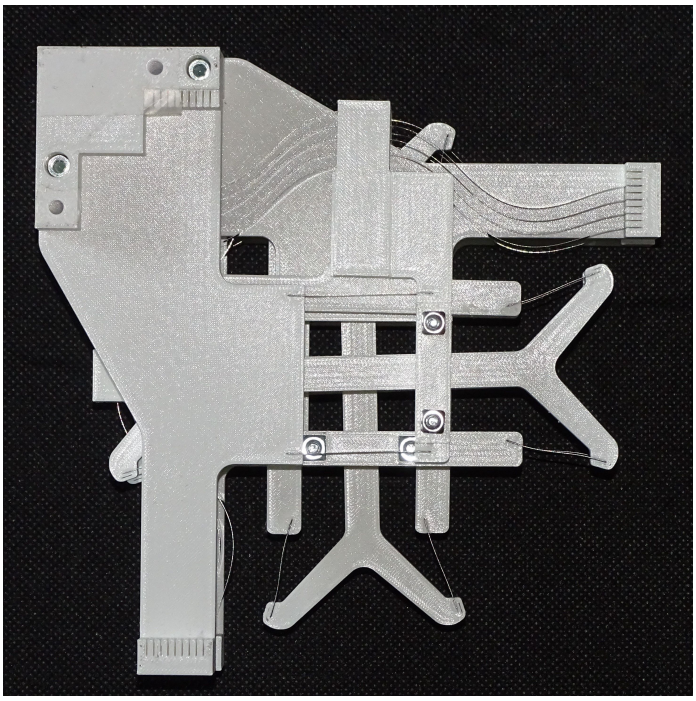

(b) Back view

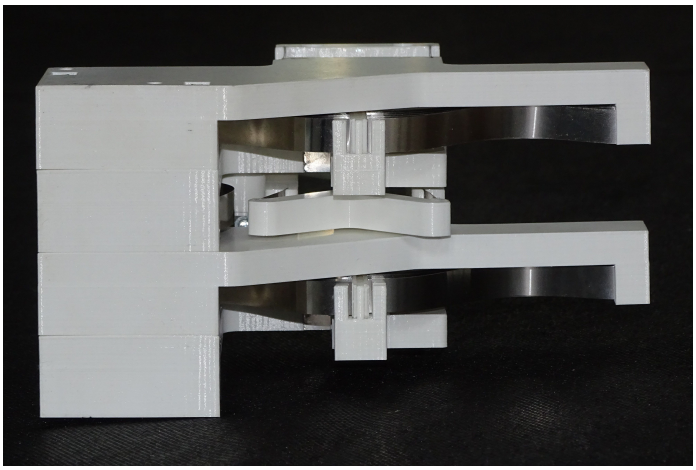

(c) Bottom view

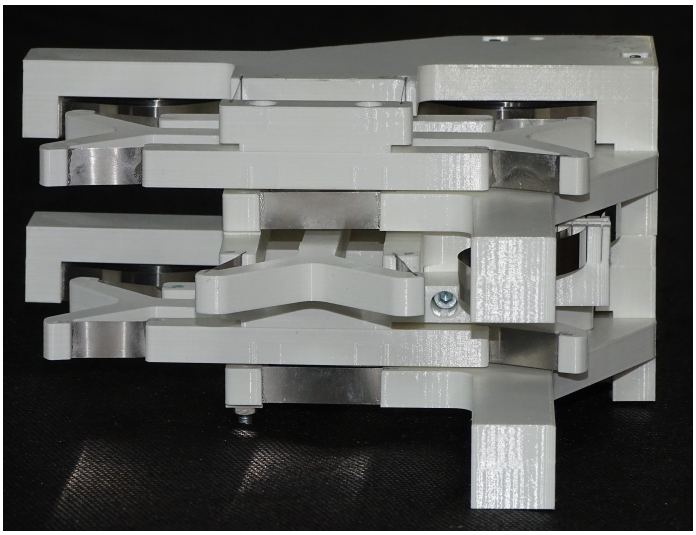

(d) Top view

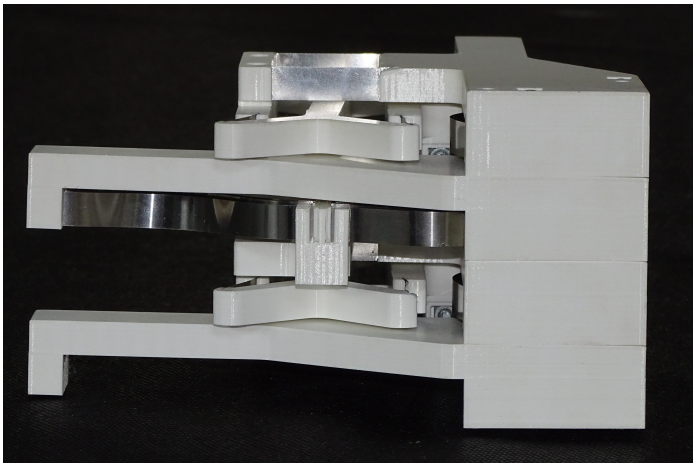

(e) Left view

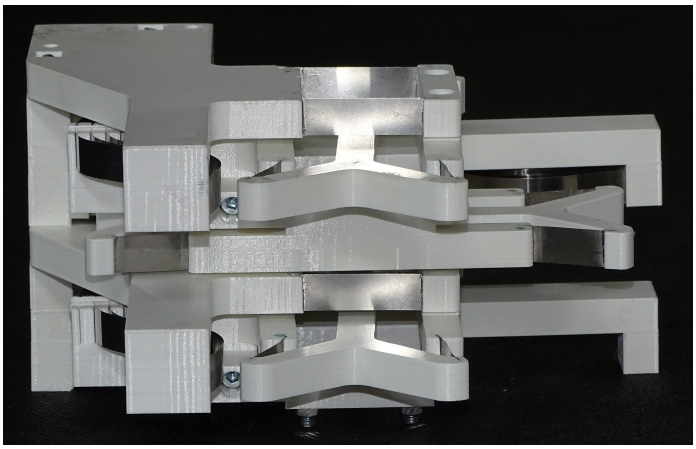

(f) Right view

Figure 28: Pictures of the assembled prototype (2D-views). Total size of prototype is 177x177x96mm.

(a) 3D-view (Front-top-right)

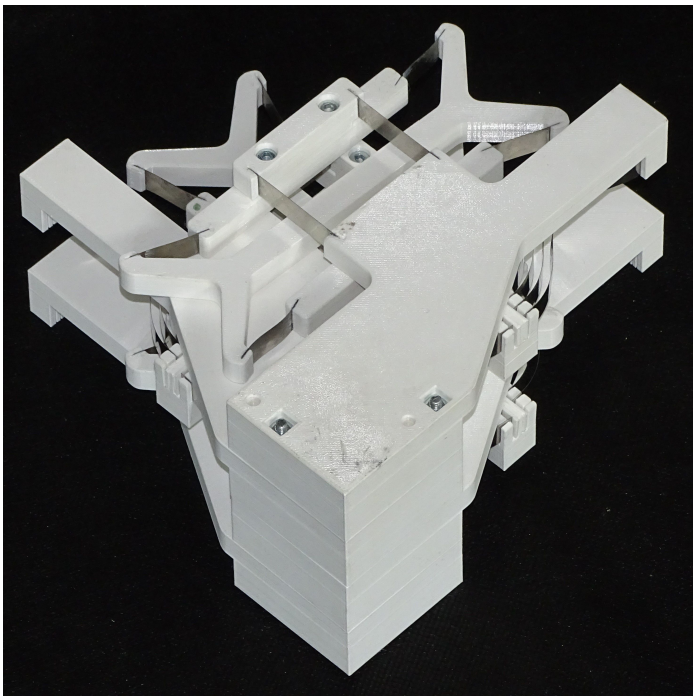

(b) 3D-view (Front-left-bottom)

Figure 29: Pictures of the assembled prototype (3D-views).

S.8 Flexure thickness

A different flexure thickness may change the load capacity (in this case output stiffness) of the designs. Analyzation process: It starts in the right graph at the selected design which is the green point with a stress just below 500 Mpa. Then the critical stress level is changed to account for the different thickness. A new design is selected with a different flexure length L. Then in the left graph a new output stiffness is obtained based on the new flexure length. This gives a rough estimate of how the output stiffness of the mechanisms can change as a function of the flexural thickness.

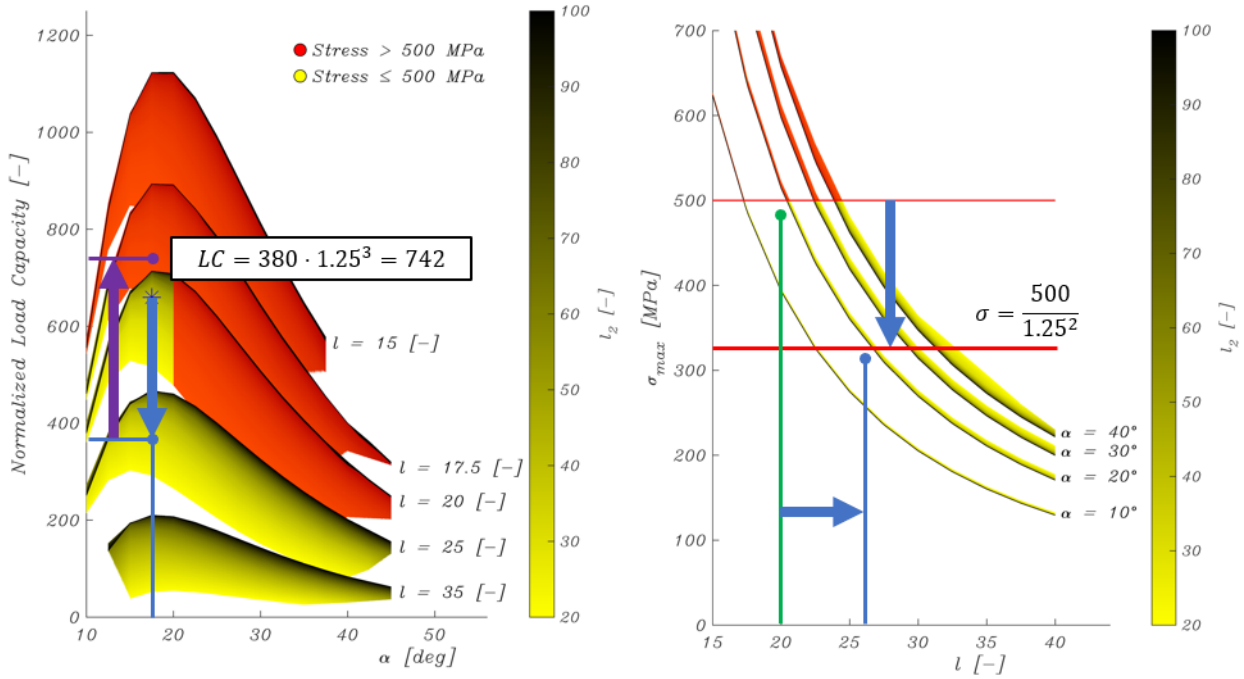

Figure 30: Influence of flexure thickness on the load capacity. Thickness of 1.25 times 0.1 mm.

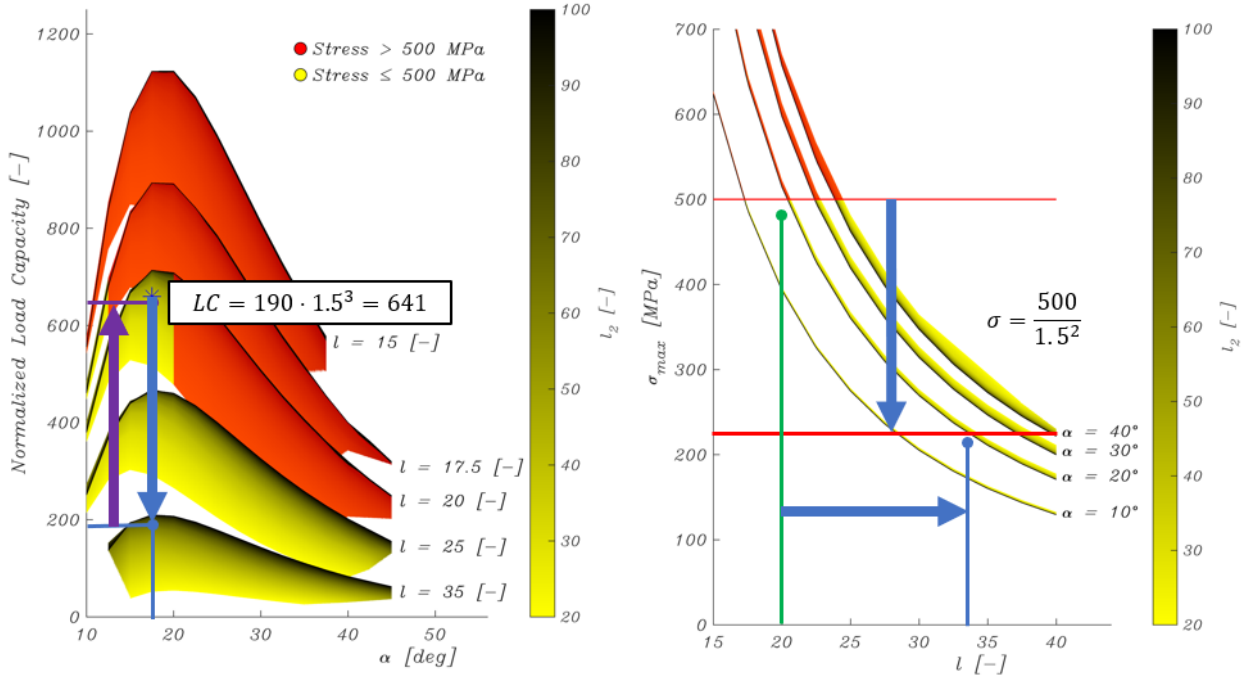

Figure 31: Influence of flexure thickness on the load capacity. Thickness of 1.5 times 0.1 mm.

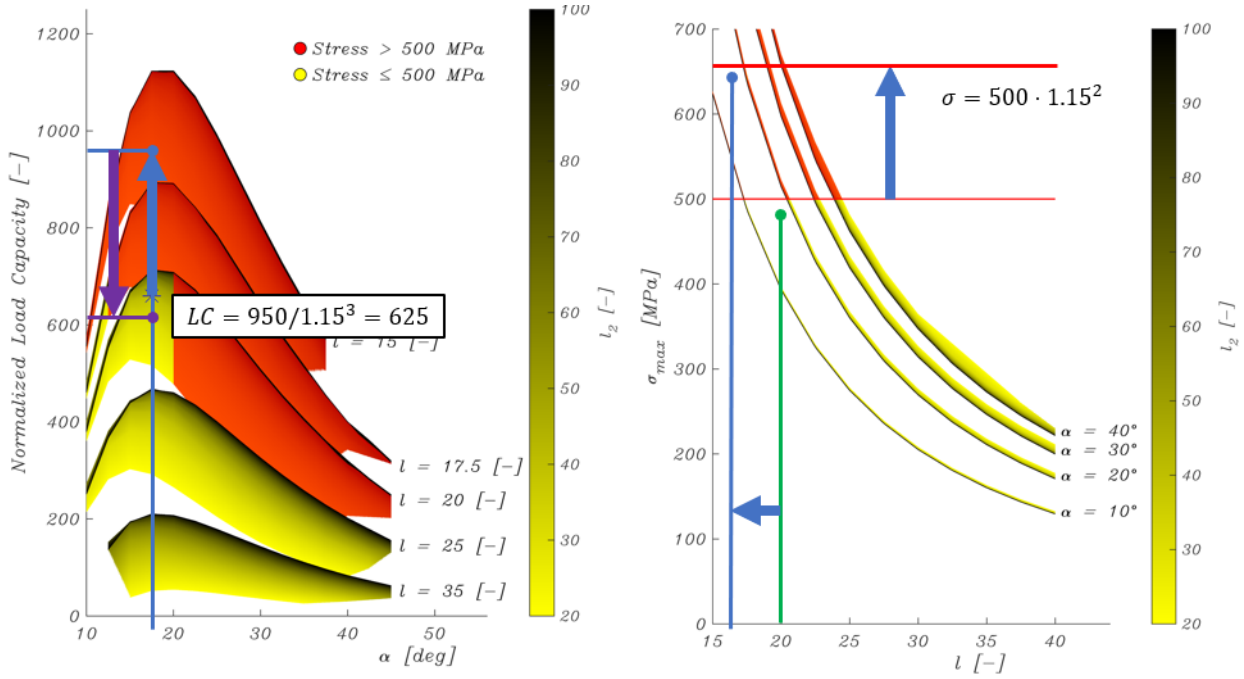

Figure 32: Influence of flexure thickness on the load capacity. Thickness of 0.87 times 0.1 mm.

S.9 Literature review

The literature review starts on the next page.

Delft University of Technology
Department of Precision and Microsystems Engineering

Energy Storage for Microrobotics: A Review of Energy and Power Density in Relation to Size

Author:
J. Tromp

Supervisor:
D. Farhadi Machekposhti

March 2, 2023

Abstract

In this study, a review of energy storage devices for microrobotic applications is presented. The review is based on criteria such as size, energy density, and power density. To provide an overview of state-of-the-art energy storing technologies, two comprehensive graphs have been created that illustrate the relationship between energy- and power density and size, based on literature examples. The most commonly used high energy density sources are covered, including elastic strain, battery, magnet, flywheel, fuel cell, metal-air, supercapacitor, chemical fuel, thermal, and pneumatic energy. Each energy source has its own advantages and disadvantages, making the choice of energy storage application highly dependent on the specific requirements of the application. The results of this study show that for micro- and nano-scale applications, strain energy is often the most suitable energy storage solution due to its ability to generate high energy and power densities. Moreover, strain energy is relatively easy to apply, as it can be directly converted into motion without the need for an actuator.

1 Introduction

Advances in micro- and nanoscale technology have facilitated the design and fabrication of millimeter-scale controllable devices, referred to as microrobots, which have the potential to be used in medical, space, military, and industrial sectors [1–4]. Microrobots are able to access tiny spaces, operate where weight is an issue, and can be used for swarming operations such as search and rescue missions [5, 6]. A significant challenge in the field of microrobotics is the identification and implementation of an appropriate power source that can meet the specific demands of microscale devices and systems. Multiple external ways of applying power and control have been utilized before, such as by external light-, sound-, magnetic, and electric sources [7, 8]. However, this makes the robot dependent on external sources, restricting the range of motion, limiting usage in unknown environments, and adding significant weight to the total system. This leaves the search for autonomous mobile microrobots, with onboard power supply and control.

Energy storage in microrobots can be quite a challenge as conventional battery technology suffers from size limitations at these scales. In nature, insects use a variety of chemicals as their energy carrier [9] and although there have been many attempts to accomplish the same energy source and actuation, it has not been done to utilize them at the same scale or efficiency as seen in the animal kingdom [10–12]. Next to batteries, many other energy storage technologies have been proposed, such as elastic strain, pneumatics, magnetic, fuels, and more. The energy density, power density, and size of individual examples are available but there is no clear overview of state-of-the-art power sources that can be used for autonomous microrobots.

This report is created to provide an overview to the microrobotic research field of the current energy storage technologies in answer of the question: What is the best energy storage for autonomous microrobots on different scales? The most promising mechanical, electrical, and chemical energy storage technologies have been reviewed with focus on their volumetric energy density, volumetric power density, and size.

2 Method

Data for this literature review was collected from various sources including published research papers, technical reports, and conference proceedings. The focus of the data collection was on energy storage technologies and their potential application in microrobotics. Data was collected through a systematic search of Google Scholar and Google, using keywords related to energy storage and microrobotics, see S.1. Additionally, the reference lists of relevant articles were manually searched to identify additional sources.

Three types of data were collected for this literature review: real existing data from literature, derived values based on published formulas and models, and theoretical data points extracted from literature. The primary focus was on real existing data which included experimental results reported in published articles. The derived values were specifically developed for this review based on published formulas and models. The theoretical data points were extracted from theoretical models proposed in literature.

It should be noted that the data collection process may have been subject to certain biases. For example, the search for certain energy storage categories may have been more extensive, potentially leading to better results for those categories. To minimize these biases, efforts were made to distribute search terms and use overviews from other literature to find the same amount of data for every category. Additionally, efforts were made to use the same search terms and protocols across all energy storage categories to ensure consistency in the data collected. Some categories had more available data points than others, and efforts were made to ensure that all categories were represented with sufficient data to draw meaningful conclusions. To ensure that all relevant studies were included, multiple databases were searched, and relevant references were cross-checked. Overall, the data collection process was designed to minimize potential sources of bias and to ensure that the most relevant and reliable data was included in the review.

As part of the evaluation of energy storage solutions for microrobots, the largest dimension of the storage device was used as a metric for physical dimensions. This approach may however not be appropriate for all solutions. For example, in the case of thin film solutions where only one dimension has been minimized. Volume instead of size would have been an option, however, it would neglect the predominant principle of microrobots, which is the restriction of maximum dimensions to allow for passage through narrow spaces. While there may be exceptions to this principle, size measurement allows for the data to be presented in a graphical format that is more easily interpreted by readers.

The scope of this review is limited to dimensions less than one meter in order to align with the scale of micro-

robotics, which are typically defined as robots operating at the millimeter scale or smaller. Additionally, this survey focuses solely on volumetric energy densities and does not take weight or density into account. Therefore, readers seeking information on energy storage solutions for microrobots where weight is a critical consideration are advised to consult other relevant sources.

3 Results

This section provides the examples of energy storage technologies, categorised based on their working principles.

3.1 Elastic Strain Energy Storage

Strain energy on macroscopic levels is common in for example coil springs. Multiple microrobots use the power of elastic strain especially for jumping.

3.1.1 Elastic Strain Energy Density

A materials strain energy is directly related to the modulus of resilience, which is the ability of a material to absorb energy from elastic deformation as energy per unit volume. For materials following Hook's law, this energy can be restored with 100% efficiency. The modulus of resilience is mathematically expressed in equation 1, with σ_y as the yield strength, E the Young's modulus and ε_y the yield strain.

$$ED_{\text{strain}} = \frac{\sigma_y^2}{2E} = \frac{1}{2}\sigma_y\varepsilon_y \tag{1}$$

The equation shows that the energy density is solely a material property and does not depend on the size of the device. However, the following examples will indicate that material properties can change when decreasing the characteristic length of the material.

Strain energy on macroscopic levels is common in for example coil springs. These offers a relatively low energy density of 1.08 kJ/L [13,14]. Multiple studies have reported high resilience in nanotubes and nanopillars. On the nanoscale, strain energy materials are developed with an energy density of 27 kJ/L using hybrid composite nanopillars from aluminum [15]. The nanopillars are 100 nm in diameter and approximately 300 nm long. On the nanoscale, experimental studies have shown that gold nanowires with diameter 40 nm have an average yield strength of 5.6 Gpa and a Young's modulus of 70 Gpa, resulting in a modulus of resilience (energy density) of 224 kJ/L. For the 200 nm wires, the yield strength decreases to 3.5 Gpa, resulting in 87.5 kJ/L [16]. Other studies have shown high energy densities of Carbon Nanotube (CNT) springs going up to a theoretical value of 8.4 MJ/L for tubes with a diameter of 1 nm [13, 17]. The much bigger and tested CNT's with a diameter of 50 µm have an energy density of only 7.723 kJ/L [13, 17].

Scientists have discovered that silicon structures with reduced characteristic lengths in the micro- and nanoscale range exhibit increased flexibility and elasticity compared to their bulk counterparts [18]. The tested silicon structures are nanowires manufactured by a "Vapor–Liquid–Solid" growth method and show a high modulus of resilience of 1.04 MJ/L with a diameter of 100 nm [18]. Other reports have shown fabrication methods of sub 100 nm precision [19] and even 20 nm [20].

Reference [21] states a minimum feature sizes of the newest novel fabrication methods of 1 µm. This will be taken as the approximate minimum size for strain energy for materials such as steel and rubber.

Nature has much to offer in the case of elastic energy as spider viscid silk has a high modulus of resilience's. The strings have a minimum diameter of 1 µm and provide an energy density up to 1.34 MJ/L [22]. This is the highest real example found.

3.1.2 Elastic Strain Power Density

Multiple microrobots use the power of elastic strain especially for jumping. One example from 2008 is a jumping robot using spring steel to jump almost 28 times its height, with a size of about 5 cm [23]. A more recent study from 2020 presents a microrobot capable of jumping 30 meters high which is 100 times its size [24]. Both robots utilize the power from strain and the energy supply from a battery, by winding a spring with an electric motor and then releasing all that energy in one time. The power density of these springs are not provided.

The power density of elastic strain can be calculated. For a beam, the equivalent mass is required, which is the mass times 33/140, approximately one forth [25]. For a tension spring, the equivalent mass is equal to Raleigh's number m/3 for low values of M/m [26, 27] (Displaced Mass / own mass). There is one reported power density of CNT stating 190 kW/L from [13] pg.37. The article does not give details about the displaced mass and does not state if this system is optimised for power density or for other parameters.

Power density calculation

The power density is a function of the speed and force applied by the strain source to a certain mass. The force applied to a mass will start it to move with an acceleration:

$$F(t) = m_{tot}\ddot{x}(t)$$

The force applied by the strain device is a function of its strain and the stiffness:

$$kx(t) = m_{tot}\ddot{x}(t)$$

This is a second order differential equation for which the solution is:

$$x(t) = e^{i\sqrt{\frac{k}{m_{tot}}}t} = C_1\cos\left(\sqrt{\frac{k}{m_{tot}}}t\right) + C_2\sin\left(\sqrt{\frac{k}{m_{tot}}}t\right)$$

With initial conditions:

$$x(0) = x_{\text{start}}$$
$$\dot{x}(0) = 0$$

Solving the system for a wire-like axial spring and calculating the average power over the range of motion yields (refer to S.2.):

$$PD_{\text{strain}} = \frac{2}{\pi}\frac{\sigma_{\text{yield}}^2}{3L}\sqrt{\frac{1}{E\rho}} \tag{2}$$

The formulation holds when using an optimal displaced mass of 2/3 of the spring mass. For other displaced masses, the

power density will be lower. The result shows that the material properties have a high effect on the power density, especially a materials yield strength. The formulation also resembles a correlation with the spring size, with increasing power densities for lower sizes.

3.2 Battery Energy Storage

Conventional batteries are one of the most common energy storage devices and are already often used in small electronic devices. A lot of millimeter-scale microrobotic walkers, rollers, and crawlers use a traditional battery as their energy supply. The output is an electric potential which is used by an actuator of some sort, control is often simple as electric currents can be regulated by regular printed circuit boards.

3.2.1 Battery Energy Density

An autonomous robotic micro-insect from 2019 utilizes a lithium-polymer battery with a size of 20mm and an energy density of 533 kJ/L [28]. This 400 gram battery is commercially available and provides power to the Dielectric Elastomer Actuators (DEA) enabling 14min of continuous operation [28].

Li-ion batteries have an energy density in the range of 1.6 MJ/L to 2.5 MJ/L [13, 14, 29–35].

Reference [34] shows an NCR18650GA lithium-ion battery with an energy density of 2.5 MJ/L and a length of 65 mm. The Sony CR1620, a non-rechargeable smaller battery, has an energy density of 2.24 MJ/L with a maximum dimension of 16 mm [36]. Smaller batteries are also developed like this 3x3x0.7mm battery from 2010 that delivers 1.44 MJ/L of energy at a power of 206 W/L [37]. An even smaller 2.2 mm microbattery has a specific capacity of 540 kJ/L with a power density of 230 W/L [36, 38]. It can also deliver a power output of 74000 W/L, however this reduces the energy density by 96% to merely 21.6 kJ/L. The smallest microbattery found has a dimension of 0.97 mm, its design utilizes 3D-printing for optimal use of the limited space in microbatteries [39]. The achieved areal energy density is 9.7 J/cm^2, which corresponds to 303 kJ/L as the height is 0.32 mm [39].

Besides lithium based batteries there are other types, like NiCd and Lead-acid, with energy densities of 540 kJ/L and 288 KJ/L respectively [40]. These are not included in the graphs, we have only included the highest performing examples.

Although many research is done to increase the energy density of batteries, a large gap remains between the theoretical and practical energy density [41]. Predictions of the maximum energy density have been made in previous articles, resulting in large theoretically reachable energy densities. The highest reachable energy density reported utilizes a CuO-Al chemistry to achieve 10.4 MJ/L [42].

3.2.2 Battery Power Density

The power density of Li-ion batteries is provided in multiple literature reviews and tops out at 10 kW/L [13, 35, 40]. For Nickel-Cadmium and Lead-acid batteries the power density is significantly lower at 700 W/L [40].

The already mentioned A123 battery is reported as a high power density battery of 5800 W/L [36]. The smallest microbattery of 0.97 mm has a power density of 2.7 mW/cm^2, corresponding to 84.4 W/L [39].

The discharge rate of a battery is known as the C-rate, where 1C stands for a discharge in 1 hour, and 2C stands for 1/2 hour, and so on. Higher discharge rates effects the capacity of batteries negatively, limiting the maximum discharge rate [43]. Li-ion batteries are therefore often limited to discharge rates of 1C, but research is still done to improve the rate. Higher discharge rate Li-ion batteries are proposed that will hold 75% of the initial capacity after 500 cycles at 30C, multiple times higher than conventional batteries [44].

3.3 Flywheel Energy Storage

There have been no reported uses of flywheel energy storage in microrobotics using the search methods implemented in this survey. This might be due to the self-discharging behaviour of flywheels. Nonetheless, the energy density of a cylindrical flywheel can be calculated using fundamental physics together with the burst speed limit of cylinders.

Harvesting the energy of a flywheel can be done in different ways. A relatively simple method is to directly connect a driving axle to the flywheel, this is for example seen in toy cars that can be charged by rolling the wheels over a flat surface. Another way is using an electric generator to produce electrical energy to power the microrobot by means of an electric actuator. This may be preferred for increased control and utilization of readily existing electrical circuits. Reference [45] provides experimental results of a mechanical 180mm flywheel and generator able to produce electricity at an efficiency of more than 98%.

A study investigating small scale Flywheel-Energy-Storage provides numerical proof that the half-time period of flywheels has a linear correlation with the scale [46]. This effect limits miniaturization of flywheels as the half-time period should be as high as possible. Applications of flywheels on micro-scale will probably involve high discharge rates and short to no energy storing time, in order to use the full energy potential of flywheels. The same study shows that the half-time period increases linearly with the density of the material [46]. A twice as heavy material has twice the half-time period. Thus, for smaller flywheels it may be beneficial to select a high density material.

3.3.1 Flywheel Energy Density

Supplementary material S.4. provides full calculations of the energy density of flywheels. A cylindrical shape is chosen to simplify the calculation. Reference [46] shows that a cylindrical disk carries about 60% the energy compared to the optimal shape, which is a laval shaped disk (thicker in the middle, thinner towards the outside).

The elastic stress of a solid disc is greatest at the center and given by the equation [47]:

$$\sigma_{\text{yield}} = \frac{3+v}{8}\rho\omega^2 r^2 \tag{3}$$

We use equation 3 to express the speed as a function of the yield strength. Given the energy of a rotating disc, the rotational inertia and the mass (refer to S.4.), the maximum

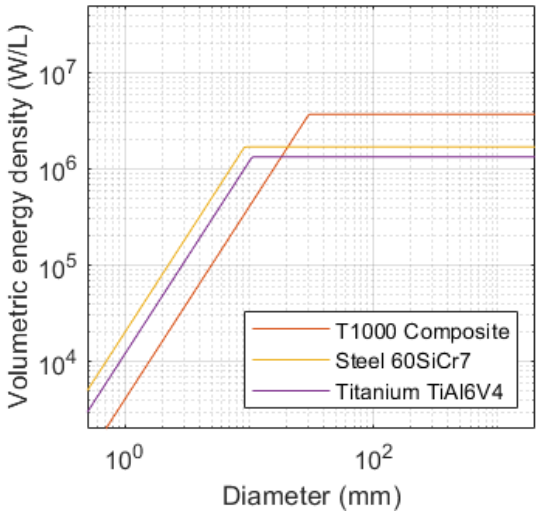

Figure 1: Flywheel Energy Density for different Materials

(kinetic) energy density of a rotating disk is provided in equation 4:

$$ED_{\text{flywheel}} = \frac{4}{3+v}\sigma_{\text{yield}} \tag{4}$$

A remarkable conclusion is that the maximum energy density of a disk is solemnly defined by the material properties. This result could lead to immoderate rotational speeds, which must be investigated due to limitations of the bearing.

As the size of bearings decreases, the maximum allowable speed approaches infinity [48]. This however ignores the practical limitations imposed by the precision of small-scale bearings and other sources of errors in MEMS-bearings. To date, the highest rotational speed achieved in micro designs has been reported as 1.4 million revolutions per minute (rpm) for a disk with a diameter of 4 mm utilizing a gas-lubricated bearing [49]. It is considered that this bearing speed represents the upper limit of achievable rotational speed for small bearings. Further development is required to increase the speed of flywheels at small scale. With the speed limitation and equation 4, the energy densities of multiple materials are illustrated in Figure 1. Material T1000, a high strength carbon fiber composite with yield strength of 3040 MPa [46] provides the highest energy density of 3.68 MJ/L. The specific diameter where the energy density drops is a function of the density of the material. A higher density material is preferable at small scales as the rotational speed limit is reached later (at smaller sizes).

3.3.2 Flywheel Power Density

The gravimetric power density of a flywheel is 12 kW/kg [14]. This would mean that the volumetric power density for a carbon fiber disk would be around 18 kW/L. For steel it would be around 90 kW/L. Another reference from 2011 about electrical energy storage provides a power density of 5 kW/L [50]. Both of these cases assume an electric generator in combination with the flywheel, limiting the power output by the choice of generator. One can imagine that sudden release of energy of a flywheel may result in higher power outputs, for example useful in jumping robots. Examples have not been found in the current existing literature.

3.4 Thermal Energy Storage

Thermal energy can both be stored in the heat capacity of materials (Sensible Heat Storage) and in the heat released from phase changing materials (Latent Heat Storage) [32]. One disadvantage of thermal energy storage is that it releases energy over time through conduction, convection and radiation. Scaling down the dimension of an object by L reduces its thermal mass by L^3, while the heat transfer scales down by L^2, meaning that thermal energy can be transferred more rapidly in smaller devices than in large devices [51]. Still it is possible to design sub-micron-scale devices where heat conduction can be significantly limited [51], indicating potential for microrobotic applications.

3.4.1 Thermal Energy Density

Molten salt is a common energy storage medium that is used as a phase changing (solid - liquid) medium to store energy [32]. Nitrates offer the highest amount of latent heat storage with about 792 kJ/L [52]. Thermochemical energy is another way to store heat that works by a chemical reaction of two substances. An example is the formation of salt $MgSO_4{*}6H_2O$, which provides 2.1 MJ/L of energy [52]. The advantage is that the heat can be generated when required, and not dissipate during long-time storage.

Based on general knowledge about microsystems, it is roughly estimated that a 1 mm scale thermal device can be utilized. Heat based MEMS-actuators such as the chevron type may be used to convert the energy into a force or motion.

3.4.2 Thermal Power Density

The power density of thermal energy depends on the rate of heat transfer from the heat source to the target body. Heat transfer can result from conduction, convection and radiation, making the power density largely dependent on geometrical factors. The power density of the previous examples have not been stated as these were only material properties. The function of heat sinks is to transfer a high amount of power, an example is an optimized heat sink able to transfer heat at a rate of 580 W/L [53]. The maximum dimension of the heat sink is approximately 130 mm.

3.5 Chemical Fuel Energy Storage

The energy from chemical fuels can be harvested via combustion and using the heat to power a type of actuator. Since traditional combustion engines are not easily scalable, other type of actuators have been proposed. Reference [54] accurately describes the use of Shape Memory Alloy (SMA) actuators as a way to utilize chemical fuels such as hydrogen, methane, or butane. An SMA wire is coated with platinum that enables catalytic combustion of the fuel causing it to heat up and contract. It is then cooled down by convection and ready to be heated again. The tested actuator showed only an efficiency of 0.02%, which dramatically decreases the energy density and has to be considered when choosing this type of energy source.

3.5.1 Chemical Fuel Energy Density

Reference [12] reports a gravimetric energy density of the fuel of 20 MJ/kg, with a density of 792 kg/m^3, resulting in a volumetric energy density of 15.8 MJ/L. This is about 10 times higher than the energy density of microbatteries [55].

The microrobot utilizing methanol fuel has a body length of ∼15 mm [12]. This length can theoretically get smaller and it is estimated that the minimum size of system will not get smaller than 1/15.7 of the current length. This is based on a wire diameter reduction stated in the report of 2.6 [12] and a slot hole reduction from 6 to 1, resulting in a total reduction of 15.7. The SMA wire would then be 0.62 mm long with a diameter of 38.1 µm.

3.5.2 Chemical Fuel Power Density

Fuel can be used in many ways and the power density can easily be limited by the type of actuator. For example, the SMA actuator used in the Robeetle microrobot can output a power density of 30 kW/L [12]. However, the power of combustion can be a lot higher if required. Microrobots utilizing combustion could shoot themselves through the air to cover distance, or perform certain tasks that requires explosive power. An article about bullet-barrel interaction provides data of a bullet being shot from a gun. The application may not be microrobotic, but it is a system optimised for power. The 50 gram bullet is accelerated to 800 m/s in 2.1 ms [56], assuming a constant acceleration this gives an average power of 7.6 MW. All the power input comes from the cartridge itself, which fits inside a cylinder with volume 55 mL (Ø21.8x147mm), resulting in a high power density of 139 MW/L. It is not certain to which size this power can be delivered, this results will therefore just be shown as a 147 mm size, neglecting the size of the barrel itself.

3.6 Magnetic Energy Storage

A system of magnets can exert forces on each other and therefore storing magnetic potential energy. Two similar poles will repel each other which could power a microrobotic system. The stored energy density is not very high, however it can be miniaturized to sub-micron level, making it an interesting principle for microrobotics as the size decreases.

3.6.1 Magnets Energy Density

Reference [57] reports a maximum energy density of magnets of 900 J/L by using equation 5 for a neodymium magnet with magnetic flux density (B) of 1.5 T:

$$ED_{magnet} = \frac{B^2}{2\mu_0} \tag{5}$$

Reference [58] provides experiments and equations of forces between cuboid magnets of strength 1.345 T. Integrating the equation of the force over the distance gives us the work done by the magnetic forces, refer to S.3.. From the investigated magnets, the 3x3x3mm cuboids achieved the highest energy density of 153 J/L, which is lower than the energy available in the magnets by equation 5 (720 J/L). This is partly due to the finite volume of magnets causing them to not fully collide with each other. Also the total volume of the system is taken here accounting for the actuating distance, with the volume constraint to the volume of both magnets, the energy density would have been 353 J/L.

Single atom magnets are readily developed showing magnetic field strengths of 6.8 Tesla [59]. The atom used here is Holmium, which has a Van der Waals radius of 233 picometer. The magnetization however does not last long, it has a relaxation time of 1500 seconds at 10 kelvins. Hence, we consider this data only as a theoretical data point. One of the smallest thermally stable magnets are CoFe2C nanoparticles with a size of 5 nm [60]. These magnets are stable up to 790 K and show similar properties to that of rare-earth magnets. Other examples show magnetized particles with median diameters of 5 micrometer [61], the observed magnetization is 355 mT, corresponding to an energy density of 50 J/L (Eq. 5). In addition to these high-tech examples, commercially available neodymium magnets are available down to a size of 1 mm [62].

3.6.2 Magnets Power Density

The power density is a function of the speed and force applied by the magnetic source to a certain mass. The force applied to a mass will start it to move with an acceleration:

$$F(t) = m_{tot}\ddot{x}(t) \tag{6}$$

The attraction forces applied by the magnets can be approximated by equation 7, with x(t) as the distance between the magnets [58]:

$$F(t) = F_0 \frac{d_e^2}{(x(t) + d_e)^2} \tag{7}$$

Where F_0 and d_e are constants. The initial conditions are:

$$\begin{aligned} x(0) &= x_{\text{start}} \\ \dot{x}(0) &= 0 \end{aligned} \tag{8}$$

The symbolic solution to this second-order nonlinear ordinary differential equation was not found with Matlab, however, the solution to this problem is found with Matlab Simulink. The resulting optimal mass to be displaced is 0.36 gram. The mass of the magnetic cuboid is 0.19 gram, thus approximately half. The average power density with this optimal mass is 62.4 kW/L, which is higher than 4 kW that is reported by a review of electrical storage from 2020 [40].

3.7 Fuel Cell Energy Storage

Fuel cell is a relatively new type of energy storage that use the high energy density of fuel, but instead of combustion it is directly converted into electricity. This gives rise to all kinds of applications where electrical energy is required, including microrobots powered by electric actuators.

3.7.1 Fuel Cell Energy Density

Reference [63] from 2008 provides a 3x3x1mm hydrogen fuel cell with tested energy density of 914 kJ/L. The cell could be improved with a different chemistry and higher efficiency to an energy density in the order of 2.52 MJ/L. Larger fuel cells are more common and two examples will be given here. The first is a 400 mm wearable fuel cell for soldiers, utilizing solid oxide to provide 2 MJ/L of energy with a power of 10 W/L [64]. The second example utilizes alane as a carrier

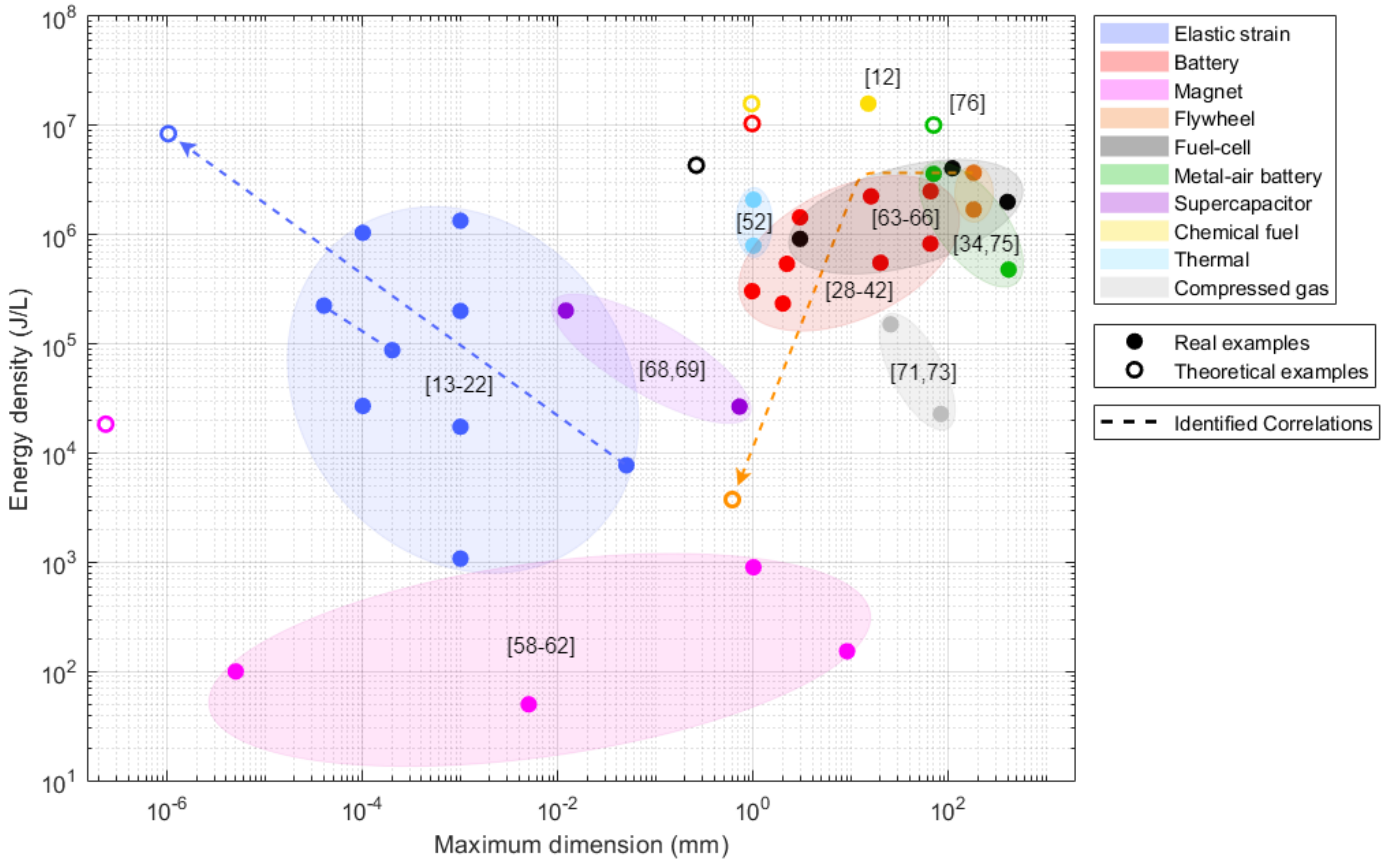

Figure 2: Volumetric energy density of energy storage technologies

of hydrogen, leading to a 109 mm device capable of storing 4.05 MJ/L of energy at a discharge rate of 15.6 W/L [65].

Reference [33] from 2008 provides multiple micro-examples of fuel cells. The smallest reported device fits in a 0.26 mm box using a "direct methanol fuel cell". The energy density of this device is not provided. The theoretical value of fuel cell is that of liquid hydrogen (stored at a temperature of 20 K), which would provide an energy density of 4.32 MJ/L [66].

3.7.2 Fuel Cell Power Density

In addition to the power densities already mentioned, a study from 2008 states that the power density for fuel cells can be more than 500 W/L [30]. This is multiple times higher than 15.6 and 10 W/L mentioned before. An article about car fuel cells from 2006 reports a power density of 450 W/L [66], adding proof to the existence of higher power densities.

3.8 Supercapacitor Energy Storage

Supercapacitors are a subcategory of capacitors that provide a higher energy density at the cost of a lower voltage. Supercapacitors have drawn interest particularly due to their low discharge time compared to batteries, 1-10s compared to 10-60 min for li-ion batteries [67]. The difference in working principle is that electrical energy is stored by static charge rather than by chemical potential in conventional batteries.

3.8.1 Supercapacitor Energy Density

Reference [68] reports recent progress of supercapacitors reporting an energy density of 56 mWh/cm^3 which corresponds to 201.6 kJ/L. This supercapacitor is made from fluorographene nanosheets with lateral sizes of max 12 µm [69].

3.8.2 Supercapacitor Power Density

According to a 2011 review on electrical storage, supercapacitors exhibit a large power density of 120 kW/L [50]. The microsupercapacitor with a size of 12 µm provides a power density of 21 kW/L [69]. Another slightly bigger supercapacitor of 0.72 mm provides a higher power density of 128 kW/L [70]. The higher power may have been at the cost of the energy density which is 26.6 kJ/L [70].

3.9 Compressed Gas Energy Storage

Compressed gas is clean, can be stored for long periods of time and can be electrically controlled by solenoid valves or other mechanical means of control [71]. Compressed gas in microrobotics are often seen in softrobotics due to the compressible nature of gas [72].

3.9.1 Compressed Gas Energy Density

The maximum energy from a compressed gas is obtained through isothermal expansion at constant temperature [73]. This requires slow expansion of the gas and is defined by equation 9:

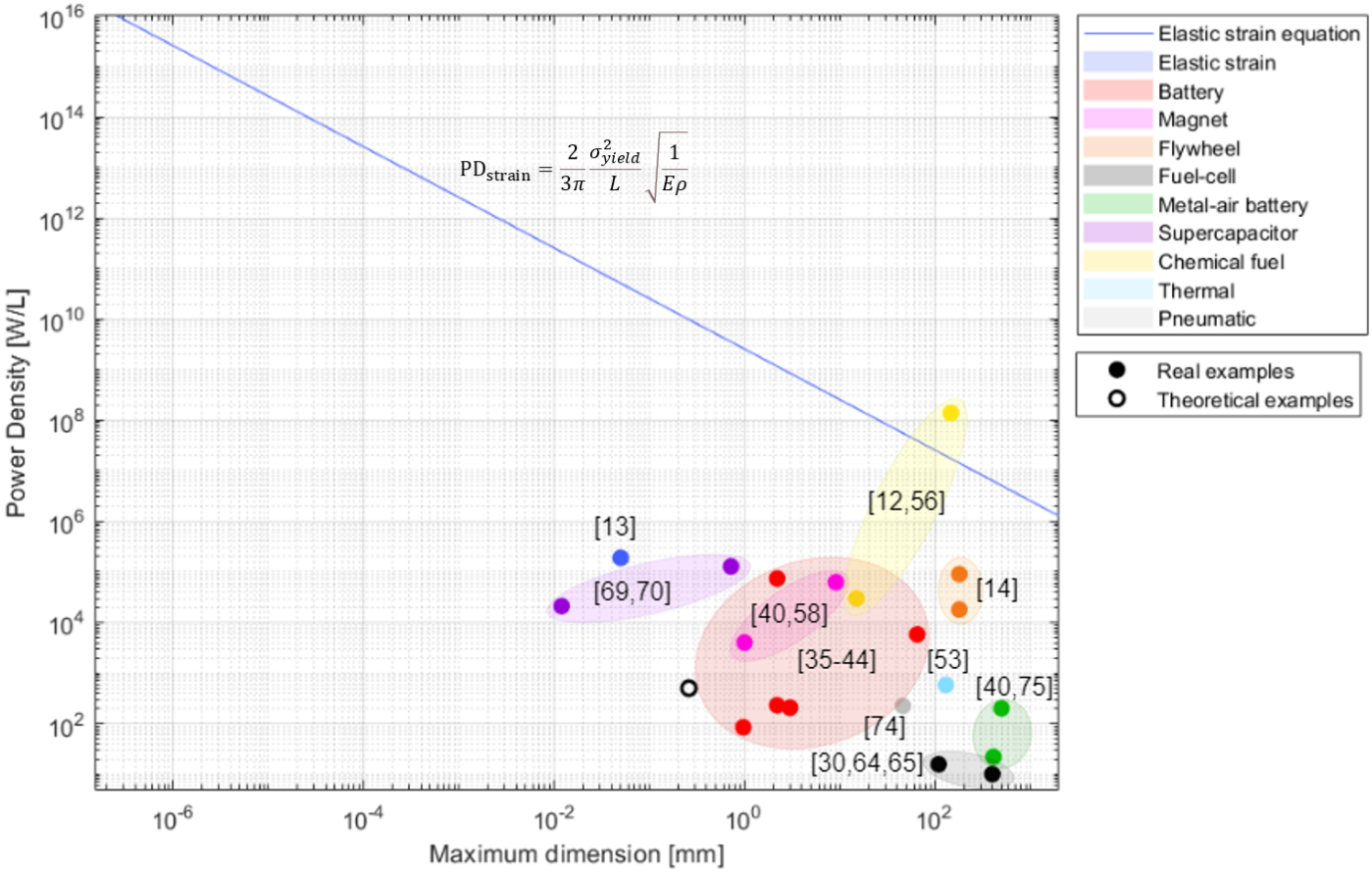

Figure 3: Power density of energy storage technologies

$$E_{tank} = p_{tank} V_{tank} \ln\left(\frac{p_{tank}}{p_{atm}}\right) \tag{9}$$

Compressed gas energy storage can be utilized in microrobotics, as done recently in a soft walking robot [71]. It walks on four legs that are powered by compressed CO_2 gas from a standard 12 gram cartridge. The four legs each consist of 3 cylinders that expand when pneumatic pressure is applied. By controlling the pressure in all 12 tubes, the legs can be moved to facilitate a turtle-like walking motion. The standard 12 gram CO_2 cartridge has a mass of 40.5 gram and contains 12 grams of CO_2 at 65 bar. It is made from steel which has a density of 7800 kg/m^3. The shape can be simplified to a cylinder with length 83 mm and diameter 18.6 mm. This gives a volume of $2.26(10^{-5})$ m^3 and a CO_2 volume of $1.89(10^{-5})$ m^3. Using equation 9 with a pressure of 65 bar, the total energy in the cartridge is 512 J, resulting in an energy density of 22.8 kJ/L.

Another example, in an attempt to achieve untethered flight, utilizes a CFRP tank to achieve burst pressures as high as 3250 bar. This results in an energy density of approximately 150 kJ/L with a tank of 25.4 mm in length [73].

3.9.2 Compressed Gas Power Density

Compressed gas as a macroscopic power supply is reported with a power density of 10 W/L [40]. The power density for microrobotic applications is unknown. A study investigating the efficiency of expansion of air when using porous inserts in pistons reports 223 W/L expansion rates at 12 bar of pressure [74]. The compressed air volume is 100 cc, which would mean, for a cubic volume, that the size is 46 mm.

3.10 Metal-air Energy Storage

Metal-air batteries is a relatively new concept, utilizing a chemical reaction of metal and oxygen from the air. Smaller batteries are hard to find, as this type of battery is in the early stages of development. Also note that this type of energy storage requires ambient air to work, which would not be possible for space-application or other vacuum environments.

3.10.1 Metal-air Energy Density

Metal-air batteries are mostly reviewed for load leveling the power grid, which is a large-scale application, providing an energy density of 36 MJ/L [30, 31, 40]. The smallest example found is a commercially available Li-air battery with a length of 70 mm. The energy density is 3.6 MJ/L [34], almost a factor of 3 higher than Li-ion batteries. Another commercially available battery is a zinc-air battery model DQFC 24/24-125, with a maximum dimension of 410 mm and an energy density of 479 kJ/L [75].

A study from 2008 has found that theoretical values of li-air batteries go up to 10.08 MJ/L [76]. The calculation excludes the weight and volume of packaging and other necessary materials which could bring the value down by 20-30% [76].

3.10.2 Metal-air Power Density

The zinc-air battery from reference [75] can deliver a maximum of 20 A of continuous current, corresponding to a power density of 22 W/L. Other sources claim a power density of 200 W/L which is a metal-air battery for a car [40]. Since it is for a car, the size is assumed to be maximum 500 mm.

3.11 Overview

Figure 2 provides an overview of all the data in all categories. Figure 3 provides the power density of all discussed energy storage methods. Theoretical data points are shown as open points and represent properties that are not yet accomplished but are theoretically reachable according to calculations or models. Transparent areas are surrounding the data points to represent a whole set of possible points. Every single point can be shifted to the right (larger size) as much as the application requires since every system can be stacked or elongated. The dashed lines are correlations between data points, it can be seen that decreasing the diameter of nanowires result in higher specific energy. Furthermore the progression of flywheel energy density is shown as a dashed line.

4 Discussion

Discussion of the implications of the results for the field of energy storage for microrobotics.

- **Graphs may be inconclusive**
  A lot of factors are not represented by the graphs, which still has to be considered during selection process. Examples are the costs, efficiency of energy conversion, actuator type decreasing the effective energy density and possibly also power. Furthermore, the size of the energy converter and actuator will increase the system size with a reduction of the energy- and power density as a consequence. There is also the discharge rate of the energy storage device, which is very high for flywheels, and present in almost all technologies.

- **Actuator efficiency**
  Multiple types of actuators can be used with electrical energy as the input, such as electrostatic, piezoelectric, thermal, and magnetic [77]. We will investigate some of them and search for the highest efficiency vs size.
  One example in an energetically expensive application of aerial flight, the micro actuator has a reported efficiency of 27% for a piezoelectric bimorph actuator of 10 mm [78]. Reference [79] reports an electrostatic thin sheet actuator with efficiency of approximately 22%, however with still a size over 100 mm. Reference [80] investigating the highest efficient motor for vehicle industry, documenting efficiency of 97% for a motor of 174 mm in diameter and 100 mm long. This indicates that high efficiencies are available in high power (85 kW) applications.
  Smaller size appear to reduce the efficiency of the actuator. Multiple factors can be the reason, such as manufacturing accuracy and having to use other actuator types for appropriate work-density.

- **Safety factor**
  All calculations are performed without safety factor, thus it is the ultimate limit of the energy source. It has to be considered that practical applications may result in lower values.

- **Weight**
  One other property of energy sources is its weight, which is related to its volume by the density. This property is not represented in this study, which has to be considered in applications where not the size is the limiting factor but the weight, such as untethered flight and space missions.

- **Bulk of data may be less optimal**
  This survey has included the most optimal solutions currently available from literature. These solutions do not present the bulk of the solutions that are applied in microrobotics or in other fields. For example, a lot of elastic devices use leaf flexures from a type of spring steel, which score lower on the graph than the presented ultra-high strength nanowires.

- **Hysteresis**
  Materials when stretched exhibit hysteresis rather than being perfectly elastic, therefore dissipating energy during an elastic cycle. This reduces the energy and power of elastic strain energy. The efficiency depends on the material and the actuating speed [81]. Hysteresis losses in the earlier shown carbon nano tube were estimated to be roughly 30%, corresponding to a spring efficiency of 70% [17]. Reference [82] provides experimental results on hysteresis in rubber (TG-B-712), when compressed to 43% at a rate of 2.2 Hz, the efficiency is 41%.

- **Non-linearity of stress-strain curve**
  Elastic materials could show non-linear behaviour below the yield limit, which makes the calculation of the modulus of resilience invalid. This effects is not taken into account and therefore the presented elastic strain energy density values should be taken as indicative data.

5 Conclusions

Based on the energy density, the following conclusions should be taken:

1. For microrobots in the range of 1-50 mm, the highest energy density options are chemical fuels and conventional batteries. One of the disadvantages of chemical fuel is that the efficiency of the actuator is very low which brings the usable energy density closer to that of the battery.

2. For microrobots of sub-millimeter scale, three types of energy storage are found in literature; elastic strain, supercapacitors and magnets. Elastic strain shows the highest energy density with a maximum of 1.34 MJ/L for spider silk. Silicon nanowires also shows high potential with an energy density of 1.04 MJ/L with the ability to manufacture these 100 nm wires via a VLS growth method. One must conclude that regular spring steel "only" has an energy density of ... and that this

is considerably lower than that of traditional batteries. Material choice is therefore important when trying to implement elastic strain into microrobotics.

3. Batteries decrease in energy density as the size decreases, while the energy density of elastic strain increases as the size decreases. This indicates that miniaturization of microrobotis will lead to elastic strain energy being a more preferable energy storage technology than conventional battery technology.

Based on the power density, the following conclusions should be taken:

1. The power density of elastic strain is high on all sizes and increases linearly as the characteristic length is decreased. This makes elastic strain the preferred energy supply for sub-millimeter microrobots that require high amounts of power.

2. The power density of supercapacitors is high compared to other electrical energy sources. It shall be noted that in most cases, the actuator must also be capable of outputting the amount of power provided from the capacitor.

3. Fuel combustion has a high power density potential.

For micro- and nano-scale applications, this report has shown that strain energy will often be preferable, as there is no other energy source that can generate comparable energy density and outstanding power density capabilities on this scale. Furthermore, strain energy is relatively easy to put in application as the energy can be directly converted to motion without the need of an actuator. Batteries and other chemical energy sources also provide high energy densities but can currently not be implemented at sub-millimeter scales. Future developments in the miniaturization of batteries and other chemical energy sources, as well as advances in their actuators, are likely to impact the viability of these energy storage options. Future developments may lead to reevaluation of the current conclusions.

Suggestion of future work is to include the weight of energy storage for a complete overview for all types of applications. In addition, the size, power and efficiency of actuators should be added to the data. Both of these improvements would clear up the overview and allow more complete conclusions about the best energy storing technology. It will also provide insight into potential areas of future research to improve energy storage in microrobotics.

References

[1] Paolo Corradi, Arianna Menciassi, and Paolo Dario. Space applications of micro-robotics: A preliminary investigation of technological challenges and scenarios. 1 2005.

[2] Paul E Kladitis and Major USAF. How small is too small? true microbots and nanobots for military application in 2035, graduation dissertation, air command and staff college, maxwell air force base, alabama, 2010.

[3] Robert Bogue. Miniature and microrobots: a review of recent developments. *Industrial Robot: An International Journal*, 42:98–102, 1 2015.

[4] Igor Paprotny and Sarah Bergbreiter. *Small-Scale Robotics. From Nano-to-Millimeter-Sized Robotic Systems and Applications: First International Workshop at ICRA 2013, Karlsruhe, Germany, May 6, 2013, Revised and Extended Papers*, volume 8336. 2 2014.

[5] Metin Sitti. Microscale and nanoscale robotics systems [grand challenges of robotics]. *IEEE Robotics Automation Magazine*, 14:53–60, 2007.

[6] Sarah Bergbreiter. Effective and efficient locomotion for millimeter-sized microrobots. pages 4030–4035, 2008.

[7] Salvador Pané, Pedro Wendel-Garcia, Yonca Belce, Xiang-Zhong Chen, and Josep Puigmartí-Luis. Powering and fabrication of small-scale robotics systems. *Current Robotics Reports*, 2:427–440, 2021.

[8] Zhongyi Li, Chunyang Li, Lixin Dong, and Jing Zhao. A review of microrobot's system: Towards system integration for autonomous actuation in vivo. *Micromachines*, 12, 2021.

[9] Bin Tang, Fernando Ariel Genta, Kai Lu, and Oleh Lushchak. *The Physiological Regulation of Energy Metabolism in Insects*. Frontiers Media SA, 2021.

[10] Mayue Shi and Eric M Yeatman. A comparative review of artificial muscles for microsystem applications. *Microsystems Nanoengineering*, 7:95, 2021.

[11] Poramate Manoonpong, Luca Patanè, Xiaofeng Xiong, Ilya Brodoline, Julien Dupeyroux, Stéphane Viollet, Paolo Arena, and Julien R Serres. Insect-inspired robots: Bridging biological and artificial systems. *Sensors*, 21, 2021.

[12] Xiufeng Yang, Longlong Chang, and Néstor O Pérez-Arancibia. An 88-milligram insect-scale autonomous crawling robot driven by a catalytic artificial muscle. *Science Robotics*, 5:eaba0015, 2020.

[13] S A Chesnokov, V A Nalimova, A G Rinzler, R E Smalley, and J E Fischer. Mechanical energy storage in carbon nanotube springs. *Physical Review Letters*, 82:343–346, 1 1999.

[14] Federico Rossi, Beatrice Castellani, and Andrea Nicolini. Benefits and challenges of mechanical spring systems for energy storage applications. *Energy Procedia*, 82:805–810, 2015.

[15] Keith J Dusoe, Xinyi Ye, Kim Kisslinger, Aaron Stein, Seok-Woo Lee, and Chang-Yong Nam. Ultrahigh elastic strain energy storage in metal-oxide-infiltrated patterned hybrid polymer nanocomposites. *Nano Letters*, 17:7416–7423, 2017.

[16] Bin Wu, Andreas Heidelberg, and John J Boland. Mechanical properties of ultrahigh-strength gold nanowires. *Nature Materials*, 4:525–529, 7 2005.

[17] Frances A Hill, Timothy F Havel, David Lashmore, Mark Schauer, and Carol Livermore. Storing energy and powering small systems with mechanical springs made of carbon nanotube yarn. *Energy*, 76:318–325, 2014.

[18] Hongti Zhang, Jerry Tersoff, Shang Xu, Huixin Chen, Qiaobao Zhang, Kaili Zhang, Yong Yang, Chun-Sing Lee, King-Ning Tu, Ju Li, and Yang Lu. Approaching the ideal elastic strain limit in silicon nanowires. *Science Advances*, 2:e1501382, 2016.

[19] Huan Hu, Hoe Joon Kim, and Suhas Somnath. Tip-based nanofabrication for scalable manufacturing, 1 2017.

[20] Heiko Wolf, Colin Rawlings, Philipp Mensch, James Hedrick, Daniel Coady, Urs Duerig, and Armin Knoll. Sub 20 nm silicon patterning and metal lift-off using thermal scanning probe lithography. *Journal of Vacuum Science Technology B*, 33, 1 2014.

[21] Minchang Wang, Daohan Ge, Liqiang Zhang, and Just L Herder. Micro-scale realization of compliant mechanisms: Manufacturing processes and constituent materials—a review. *Chinese Journal of Mechanical Engineering*, 34:85, 2021.

[22] Mark J Bonino. Material properties of spider silk, 2003.

[23] Mirko Kovac, Martin Fuchs, Andre Guignard, Jean-Christophe Zufferey, and Dario Floreano. A miniature 7g jumping robot. pages 373–378, 2008.

[24] Elliot W Hawkes, Charles Xiao, Richard-Alexandre Peloquin, Christopher Keeley, Matthew R Begley, Morgan T Pope, and Günter Niemeyer. Engineered jumpers overcome biological limits via work multiplication. *Nature*, 604:657–661, 2022.

[25] Metin Gurgoze. On the representation of a cantilevered beam carrying a tip mass by an equivalent spring–mass system. *Journal of Sound and Vibration - J SOUND VIB*, 282:538–542, 1 2005.

[26] Jun ichi Ueda and Yoshiro Sadamoto. A measurement of the effective mass of coil springs. *Journal of the Physical Society of Japan*, 66:367, 2 1997.

[27] Eduardo Rodríguez and Gabriel Gesnouin. Effective mass of an oscillating spring. *The Physics Teacher*, 45:100, 1 2007.

[28] Xiaobin Ji, Xinchang Liu, Vito Cacucciolo, Matthias Imboden, Yoan Civet, Alae El Haitami, Sophie Cantin, Yves Perriard, and Herbert Shea. An autonomous untethered fast soft robotic insect driven by low-voltage dielectric elastomer actuators. *Science Robotics*, 4:eaaz6451, 2019.

[29] Nitin Muralidharan, Ethan C Self, Jagjit Nanda, and Ilias Belharouak. Next-generation cobalt-free cathodes – a prospective solution to the battery industry's cobalt problem*, 2022.

[30] Haisheng Chen, Thang Ngoc Cong, Wei Yang, Chunqing Tan, Yongliang Li, and Yulong Ding. Progress in electrical energy storage system: A critical review. *Progress in Natural Science*, 19:291–312, 2009.

[31] Nasrullah Khan, Saad Dilshad, Rashida Khalid, Ali Kalair, and Naeem Abas. Review of energy storage and transportation of energy. *Energy Storage*, 1:e49, 1 2019.

[32] Jidai Wang, Kunpeng Lu, Lan Ma, Jihong Wang, Mark Dooner, Shihong Miao, Jian Li, and Dan Wang. Overview of compressed air energy storage and technology development. *Energies*, 10, 2017.

[33] Kimberly Cook-Chennault, N Thambi, and Ann Sastry. Powering mems portable devices - a review of non-regenerative and regenerative power supply systems with special emphasis on piezoelectric energy harvesting systems. *Smart Materials and Structures*, 17, 1 2008.

[34] Jung Park, Mokwon Kim, Joon-Hee Kim, Kyoung Choi, Heung Chan Lee, Wonsung Choi, Sang Ma, and Dongmin Im. A 1000 wh kg −1 li–air battery: Cell design and performance. *Journal of Power Sources*, 419:112–118, 1 2019.

[35] Shuai Ma, Modi Jiang, Peng Tao, Chengyi Song, Jianbo Wu, Jun Wang, Tao Deng, and Wen Shang. Temperature effect and thermal impact in lithium-ion batteries: A review. *Progress in Natural Science: Materials International*, 28:653–666, 2018.

[36] James H Pikul, Hui Gang Zhang, Jiung Cho, Paul V Braun, and William P King. High-power lithium ion microbatteries from interdigitated three-dimensional bicontinuous nanoporous electrodes. *Nature Communications*, 4:1732, 2013.

[37] Wei Lai, Can K Erdonmez, Thomas F Marinis, Caroline K Bjune, Nancy J Dudney, Fan Xu, Ryan Wartena, and Yet-Ming Chiang. Ultrahigh-energy-density microbatteries enabled by new electrode architecture and micropackaging design. *Advanced Materials*, 22:E139–E144, 2010.

[38] Yuxing Wang, Bo Liu, Qiuyan Li, Samuel Cartmell, Seth Ferrara, Zhiqun Daniel Deng, and Jie Xiao. Lithium and lithium ion batteries for applications in microelectronic devices: A review. *Journal of Power Sources*, 286:330–345, 2015.

[39] Ke Sun, Teng-Sing Wei, Bok Yeop Ahn, Jung Yoon Seo, Shen J Dillon, and Jennifer A Lewis. 3d printing of interdigitated li-ion microbattery architectures. *Advanced Materials*, 25:4539–4543, 2013.

[40] S Koohi-Fayegh and M A Rosen. A review of energy storage types, applications and recent developments. *Journal of Energy Storage*, 27:101047, 2020.

[41] Johannes Betz, Georg Bieker, Paul Meister, Tobias Placke, Martin Winter, and Richard Schmuch. Theoretical versus practical energy: A plea for more transparency in the energy calculation of different rechargeable battery systems. *Advanced Energy Materials*, 9:1803170, 2019.

[42] Wenzhuo Cao, Jienan Zhang, and Hong Li. Batteries with high theoretical energy densities. *Energy Storage Materials*, 26:46–55, 2020.

[43] Gang Ning, Bala Haran, and Branko N Popov. Capacity fade study of lithium-ion batteries cycled at high discharge rates. *Journal of Power Sources*, 117:160–169, 2003.

[44] Toshiki Nokami, Takahiro Matsuo, Yuu Inatomi, Nobuhiko Hojo, Takafumi Tsukagoshi, Hiroshi Yoshizawa, Akihiro Shimizu, Hiroki Kuramoto, Kazutomo Komae, Hiroaki Tsuyama, and Jun ichi Yoshida. Polymer-bound pyrene-4,5,9,10-tetraone for fast-charge and -discharge lithium-ion batteries with high capacity. *Journal of the American Chemical Society*, 134:19694–19700, 2012.

[45] B T Merritt, R F Post, G R Dreifuerst, and D A Bender. Halbach array motor/generators: A novel generalized electric machine, 10 1994.

[46] Gabriel Ertz, Jens Twiefel, and Malte Krack. Feasibility study for small scaling flywheel-energy-storage systems in energy harvesting systems. *Energy Harvesting and Systems*, 1, 2 2014.

[47] Arthur G Holms and Joe E Jenkins. Effect of strength and ductility on burst characteristics of rotating disks. 1948.

[48] Iso 15312:2018(e): Rolling bearings - thermal speed rating - calculation, 2018.

[49] L G Frechette, S A Jacobson, K S Breuer, F F Ehrich, R Ghodssi, R Khanna, Chee Wei Wong, Xin Zhang, M A Schmidt, and A H Epstein. High-speed microfabricated silicon turbomachinery and fluid film bearings. *Journal of Microelectromechanical Systems*, 14:141–152, 2005.

[50] Electrical energy storage : white paper. *International Electrotechnical Commission*, 2011.

[51] Jack W Judy. Microelectromechanical systems (mems): fabrication, design and applications. *Smart Materials and Structures*, 10:1115, 2001.

[52] Ioan Sarbu and Calin Sebarchievici. A comprehensive review of thermal energy storage. *Sustainability*, 10, 2018.

[53] Hyunkyu Moon, Nenad Miljkovic, and William P King. High power density thermal energy storage using additively manufactured heat exchangers and phase change material. *International Journal of Heat and Mass Transfer*, 153:119591, 2020.

[54] Fares Maimani, Ariel A. Calderón, Xiufeng Yang, Alberto Rigo, Joey Z. Ge, and Néstor O. Pérez-Arancibia. A 7-mg miniature catalytic-combustion engine for millimeter-scale robotic actuation. *Sensors and Actuators A: Physical*, 341, 7 2022.

[55] Ryan L Truby and Shuguang Li. Integrating chemical fuels and artificial muscles for untethered microrobots. *Science Robotics*, 5:eabd7338, 2020.

[56] Chao Shen, Ke dong Zhou, Ye Lu, and Jun song Li. Modeling and simulation of bullet-barrel interaction process for the damaged gun barrel. *Defence Technology*, 15:972–986, 2019.

[57] P B Koeneman, I J Busch-Vishniac, and K L Wood. Feasibility of micro power supplies for mems. *Journal of Microelectromechanical Systems*, 6:355–362, 1997.

[58] Werner Karl Schomburg, Olivier Reinertz, Johannes Sackmann, and Katharina Schmitz. Equations for the approximate calculation of forces between cuboid magnets. *Journal of Magnetism and Magnetic Materials*, 506:166694, 2020.

[59] F Donati, S Rusponi, S Stepanow, C Wäckerlin, A Singha, L Persichetti, R Baltic, K Diller, F Patthey, E Fernandes, J Dreiser, Ž Šljivančanin, K Kummer, C Nistor, P Gambardella, and H Brune. Magnetic remanence in single atoms. *Science*, 352:318–321, 2016.

[60] Ahmed A El-Gendy, Massimo Bertino, Dustin Clifford, Meichun Qian, Shiv N Khanna, and Everett E Carpenter. Experimental evidence for the formation of cofe2c phase with colossal magnetocrystalline-anisotropy. *Applied Physics Letters*, 106:213109, 2015.

[61] Mani Teja Bodduluri, Björn Gojdka, Niklas Wolff, Lorenz Kienle, Thomas Lisec, and Fabian Lofink. Investigation of wafer-level fabricated permanent micromagnets for mems. *Micromachines*, 13, 2022.

[62] https://www.supermagnete.nl/data_sheet_S-01-01-N.pdf. Supermagnete, Accessed: 2018-12-06.

[63] Saeed Moghaddam, Eakkachai Pengwang, Kevin Y Lin, Richard I Masel, and Mark A Shannon. Millimeter-scale fuel cell with onboard fuel and passive control system. *Journal of Microelectromechanical Systems*, 17:1388–1395, 2008.

[64] T Thampan, D Shah, C Cook, J Novoa, and S Shah. Development and evaluation of portable and wearable fuel cells for soldier use. *Journal of Power Sources*, 259:276–281, 2014.

[65] Kyle N Grew, Zachary B Brownlee, Kailash C Shukla, and Deryn Chu. Assessment of alane as a hydrogen storage media for portable fuel cell power sources. *Journal of Power Sources*, 217:417–430, 2012.

[66] Steven G Chalk and James F Miller. Key challenges and recent progress in batteries, fuel cells, and hydrogen storage for clean energy systems. *Journal of Power Sources*, 159:73–80, 2006.

[67] Waseem Raza, Faizan Ali, Nadeem Raza, Yiwei Luo, Ki-Hyun Kim, Jianhua Yang, Sandeep Kumar, Andleeb Mehmood, and Eilhann E Kwon. Recent advancements in supercapacitor technology. *Nano Energy*, 52:441–473, 2018.

[68] Jinhui Wang, Fei Li, Feng Zhu, and Oliver G Schmidt. Recent progress in micro-supercapacitor design, integration, and functionalization. *Small Methods*, 3:1800367, 2019.

[69] Feng Zhou, Haibo Huang, Chuanhai Xiao, Shuanghao Zheng, Xiaoyu Shi, Jieqiong Qin, Qiang Fu, Xinhe Bao, Xinliang Feng, Klaus Müllen, and Zhong-Shuai Wu. Electrochemically scalable production of fluorine-modified graphene for flexible and high-energy ionogel-based microsupercapacitors. *Journal of the American Chemical Society*, 140:8198–8205, 1 2018.

[70] Chuizhou Meng, Jimin Maeng, Simon W M John, and Pedro P Irazoqui. Ultrasmall integrated 3d micro-supercapacitors solve energy storage for miniature devices. *Advanced Energy Materials*, 4:1301269, 2014.

[71] Dylan Drotman, Saurabh Jadhav, David Sharp, Christian Chan, and Michael T Tolley. Electronics-free pneumatic circuits for controlling soft-legged robots. *Science Robotics*, 6:eaay2627, 2021.

[72] George M Whitesides. Soft robotics. *Angewandte Chemie International Edition*, 57:4258–4273, 2018.

[73] Venkata Siva Prasad Pulla. Insect powered micro air vehicles and centimeter scale high energy density pneumatic sources, 2012.

[74] Bo Yan, Jacob Wieberdink, Farzad Shirazi, Perry Y Li, Terrence W Simon, and James D Van de Ven. Experimental study of heat transfer enhancement in a liquid piston compressor/expander using porous media inserts. *Applied Energy*, 154:40–50, 2015.

[75] José Manuel Andújar, Francisca Segura, Jesús Rey, and Francisco José Vivas. Batteries and hydrogen storage: Technical analysis and commercial revision to select the best option. *Energies*, 15, 2022.

[76] J P Zheng, R Y Liang, M Hendrickson, and E J Plichta. Theoretical energy density of li–air batteries. *Journal of The Electrochemical Society*, 155:A432, 4 2008.

[77] D J Bell, T J Lu, N A Fleck, and S M Spearing. Mems actuators and sensors: observations on their performance and selection for purpose. *Journal of Micromechanics and Microengineering*, 15:S153, 6 2005.

[78] E Farrell, Karpelson Michael, Wood Robert J Jafferis Noah T., and Helbling. Untethered flight of an insect-sized flapping-wing microscale aerial vehicle. *Nature*, 570:491–495, 6 2019.

[79] T Niino, S Egawa, and T Higuchi. High-power and high-efficiency electrostatic actuator. pages 236–241, 1993.

[80] Kohei Aiso and Kan Akatsu. Performance comparison of high-speed motors for electric vehicle. *World Electric Vehicle Journal*, 13, 2022.

[81] Bertram Hopkinson and Trevor G Williams. The elastic hysteresis of steel. *Proceedings of the Royal Society of London. Series A, Containing Papers of a Mathematical and Physical Character*, 87:502–511, 1912.

[82] Milan Banic, Dusan Stamenkovic, V Miltenovic, Milos Milosevic, Aleksandar Miltenovic, Petar Djekic, and Milan Rackov. Prediction of heat generation in rubber or rubber-metal springs. *Thermal Science*, 16:527–539, 2 2012.

SUPPLEMENTARY MATERIAL

S.1. Search Method

There have been many search methods by which the literature has been found. Terms and combinations of terms are used as a way to search the internet as represented in Table 1. Not all columns are used in all searches, most of the time combinations of two, three or four terms have been selected. The search terms have been implemented in search engines Google and Google Scholar.

Search term 1	**Search term 2**	**Search term 3**	**Search term 4**	**Search term 5**
Elastic/strain	Energy storage	Micro	Review	J/L
Battery	Energy source	Microrobotics	Survey	J/m^3
Magnet	Energy storage device	Smallest	Overview	W/L
Flywheel	Energy density	Small scale		W/m^3
Fuel-cell	Power density	Millimeter-scale		
Metal-air	Volumetric energy density	Micro-scale		
Supercapacitor	Volumetric power density	Nano-scale		
Chemical/fuel				
Thermal				
Pneumatic				

Table 1: Indication of Search Terms Used

S.2. Strain Power Calculation

$$F(t) = m_{tot}\ddot{x}(t) \tag{10}$$

The force applied by the strain device is a function of its strain and the stiffness:

$$kx(t) = m_{tot}\ddot{x}(t) \tag{11}$$

This is a second order differential equation for which the solution is:

$$x(t) = e^{i\sqrt{\frac{k}{m_{tot}}}t} = C_1 \cos\left(\sqrt{\frac{k}{m_{tot}}}t\right) + C_2 \sin\left(\sqrt{\frac{k}{m_{tot}}}t\right) \tag{12}$$

The initial conditions are:

$$\begin{aligned} x(0) &= x_{\text{start}} \\ \dot{x}(0) &= 0 \end{aligned} \tag{13}$$

Which gives:

$$x(t) = x_{\text{start}} \cos\left(\sqrt{\frac{k}{m_{tot}}}t\right) \tag{14}$$

x_{start} is the strain applied at the point of release, which will be the strain at yield:

$$\sigma_{\text{yield}} = \frac{F}{A} = \frac{kx_{\text{start}}}{A} \quad \rightarrow \quad x_{\text{start}} = \frac{A\sigma_{\text{yield}}}{k} \tag{15}$$

x_{start} can be substituted in equation 14 and differentiated to find the speed and acceleration:

$$\begin{aligned} x(t) &= \frac{A\sigma_{\text{yield}}}{k} \cos\left(\sqrt{\frac{k}{m_{\text{tot}}}}t\right) \\ \dot{x}(t) &= -\frac{A\sigma_{\text{yield}}}{k}\sqrt{\frac{k}{m_{\text{tot}}}} \sin\left(\sqrt{\frac{k}{m_{\text{tot}}}}t\right) \\ \ddot{x}(t) &= -\frac{A\sigma_{\text{yield}}}{m_{\text{tot}}} \cos\left(\sqrt{\frac{k}{m_{\text{tot}}}}t\right) \end{aligned} \tag{16}$$

With m_{tot} equal to one third of the mass of the spring m_1, according to [26, 27], and the displaced mass m_2:

$$m_{tot} = \frac{1}{3}m_1 + m_2 \tag{17}$$

The power density is equal to the force applied to the displaced mass times the speed divided by the volume:

$$\begin{aligned} PD_{\text{strain}}(t) &= \frac{F(t)\dot{x}(t)}{V} \\ &= \frac{m_2\ddot{x}(t)\dot{x}(t)}{LA} \\ &= \frac{m_2}{m_{\text{tot}}}\frac{A\sigma_{\text{yield}}^2}{Lk}\sqrt{\frac{k}{m_{\text{tot}}}} \cos\left(\sqrt{\frac{k}{m_{\text{tot}}}}t\right) \sin\left(\sqrt{\frac{k}{m_{\text{tot}}}}t\right) \end{aligned} \tag{18}$$

The power density at any point in time is obtained, however, we will look at the average power density. The peak power density will be higher but the average power density is regarded as more important.

The average power density will be calculated between the start ($x(0) = x_{\text{start}}$) and the end ($x(t_{\text{end}}) = 0$):

$$\begin{aligned} x(t_{\text{end}}) = 0 &= \frac{A\sigma_{\text{yield}}}{k} \cos\left(\sqrt{\frac{k}{m_{\text{tot}}}}t_{\text{end}}\right) \\ 0 &= \cos\left(\sqrt{\frac{k}{m_{tot}}}t_{\text{end}}\right) \\ t_{\text{end}} &= \frac{1}{2}\pi\sqrt{\frac{m_{\text{tot}}}{k}} \end{aligned} \tag{19}$$

The average power density is the integral of the power density divided by the time:

$$\begin{aligned} PD_{\text{strain.average}} &= \frac{1}{t_{\text{end}} - 0}\int_0^{t_{\text{end}}} PD_{\text{strain}}\,(t)dt \\ &= \frac{m_2}{m_{\text{tot}}}\frac{A\sigma_{\text{yield}}^2}{Lk}\sqrt{\frac{k}{m_{\text{tot}}}}\frac{1}{t_{\text{end}}}\int_0^{t_{\text{end}}} \cos\left(\sqrt{\frac{k}{m_{\text{tot}}}}t\right)\sin\left(\sqrt{\frac{k}{m_{\text{tot}}}}t\right)dt \\ &= \frac{m_2}{m_{\text{tot}}}\frac{A\sigma_{\text{yield}}^2}{Lk}\sqrt{\frac{k}{m_{\text{tot}}}}\frac{1}{t_{\text{end}}}\left[-\frac{\cos^2\left(\sqrt{\frac{k}{m_{\text{tot}}}}t\right)}{2\sqrt{\frac{k}{m_{\text{tot}}}}}\right]_0^{t_{\text{end}}} \\ &= \frac{m_2}{m_{\text{tot}}}\frac{A\sigma_{\text{yield}}^2}{Lk}\frac{1}{t_{\text{end}}}\frac{1}{2} \\ &= \frac{m_2}{m_{\text{tot}}}\frac{A\sigma_{\text{yield}}^2}{Lk\pi}\sqrt{\frac{k}{m_{\text{tot}}}} \end{aligned} \tag{20}$$

Substitute 17 into 20 to give the power density as a function of the displaced mass:

$$PD_{\text{strain.average}} = \frac{3m_2}{m_1 + 3m_2}\frac{A\sigma_{\text{yield}}^2}{Lk\pi}\sqrt{\frac{3k}{m_1 + 3m_2}} \tag{21}$$

A certain displaced mass m_2 will give an optimal power density. We take the derivative of the power density with respect to m_2 and set it to zero to find the optimal value of m_2. The quotient rule is used here:

$$\begin{aligned} \frac{\partial PD_{\text{strain.average}}}{\partial m_2} = 0 &= \frac{A\sigma_{\text{yield}}^2}{Lk\pi}\cdot\frac{3\,(2m_1 - 3m_2)}{2\,(m_1 + 3m_2)^2}\sqrt{\frac{3k}{m_1 + 3m_2}} \\ 0 &= 2m_1 - 3m_2 \end{aligned} \tag{22}$$

$$m_2 = \frac{2}{3}m_1 \tag{23}$$

$PD_{\text{strain.average}}$ has the highest value when the mass on the end of the string is 2/3 of the weight of the spring.

Substituting 23 into 21 gives:

$$PD_{\text{strain.average}} = \frac{2}{\pi}\frac{A\sigma_{\text{yield}}^2}{3Lk}\sqrt{\frac{k}{m_1}} \tag{24}$$

The axial stiffness of a wire-like spring is given as:

$$k = \frac{AE}{L} \tag{25}$$

With spring mass:

$$m_1 = AL\rho \tag{26}$$

This gives the power density for an axial wire spring with optimal displacing mass:

$$PD_{\text{strain.average}} = \frac{2}{\pi}\frac{\sigma_{\text{yield}}^2}{3L}\sqrt{\frac{1}{E\rho}} \tag{27}$$

The same calculation can be done for a cantilever beam which gives a lower power density.

S.3. Two Cuboid Magnets Attracting; Calculations

The attraction forces of two magnets is approximated by equation 28 with x(t) as the distance between the magnets [58]:

$$F(t) = F_0 \frac{d_e^2}{(x(t) + d_e)^2} \tag{28}$$

Where F_0 and d_e are constants (3x3x3 mm magnets):

$$\begin{aligned} F_0 &= -11.9\text{N} \\ d_e &= 0.0016\text{mm} \end{aligned}$$

Energy Density

The work done by the magnets is calculated by integration of the force over the distance:

$$W = \int_0^{x_{\text{end}}} F(t)dx \tag{29}$$

$$W = \frac{F_0 d_e^2}{x_{\text{end}} + d_e} - F_0 d_e \tag{30}$$

The resulting work is a function of x_{end}, which is determined by the amount of distance the two magnets get. In case of repelling magnets, it is indeed x_{end}, in case of attracting magnets, x_{end} would be x_{start}.

The final distance x is included in the total volume of the energy storing system. This leads to an optimal energy density where the work and the volume are in balance. Increasing one or the other leads to a lower energy density. For the two 3x3x3 magnets, x_{end} turned out to be 3.1 mm to obtain the highest amount of energy density. The value of x_{end} was obtained by simple trial and error.

Power Density

The magnetic force applied to a mass will start it to move with an acceleration:

$$F(t) = m_{tot}\ddot{x}(t) \tag{31}$$

With initial conditions:

$$\begin{aligned} x(0) &= x_{\text{start}} \\ \dot{x}(0) &= 0 \end{aligned} \tag{32}$$

This gives the second-order nonlinear ordinary differential equation:

$$F_0 \frac{d_e^2}{(x(t) + d_e)^2} = m_{tot}\ddot{x}(t) \tag{33}$$

The symbolic solution to this second-order nonlinear ordinary differential equation was not found with Matlab, however, the solution to this problem is found with Matlab Simulink. The resulting optimal mass to be displaced is 0.36 gram. The mass of the magnetic cuboid is 0.19 gram, thus approximately half. The average power density with this optimal mass is found to be $6.24{\cdot}10^4$ W/L.

S.4. Flywheel Energy Density; Calculations

Consider a flat disc with radius r and thickness t spinning around its central axis. Then the energy will be defined by:

$$\begin{aligned} E_{\text{disc}} &= \frac{1}{2} J\omega^2 \\ J &= mr^2 \\ m &= \rho V = \rho\pi r^2 t \end{aligned}$$

The elastic stress of a solid disc is greatest at the center and given by the formula [47]:

$$\sigma_{\text{yield}} = \frac{3+v}{8}\rho\omega^2 r^2$$

Which can be rewritten to obtain the rotational speed ω :

$$\omega^2 = \frac{8}{3+v}\frac{\sigma_{yield}}{\rho r^2}$$

Assuming the rotational speed will be a function of the yield strength (higher rotational speeds for higher strength materials), the energy can be rewritten in terms of yield strength:

$$E_{\text{disc}} = J\frac{4}{3+v}\frac{\sigma_{\text{yield}}}{\rho r^2}$$

Substituting inertia J:

$$E_{\text{disc}} = mr^2\frac{4}{3+v}\frac{\sigma_{yield}}{\rho r^2} = \frac{4}{3+v}\sigma_{yield}\pi r^2 t$$

In this example where the rotational speed is a function of the yield strength of the material, the energy of a flywheel is a function of the Poisson's ratio, yield strength, radius, and thickness. The energy density is what needs to be obtained here and is defined as:

$$\left(\frac{E}{V}\right)_{\text{flywheel}} = \frac{E_{\text{disc}}}{\pi r^2 t} = \frac{4}{3+v}\sigma_{\text{yield}}$$

A remarkable conclusion is that the maximum energy density of a disk is solemnly defined by the material properties. This result could lead to immoderate rotational speeds, which must be investigated due to limitations of the bearing.